University of Southampton

Faculty of Engineering and Physical Science

School of Chemistry

Nitrides or carbides coated on hard carbon for sodium ion batteries

Hang Cheng

Thesis for the degree of Doctor of Philosophy

Submission date: March, 2021

Table of Contents

Figures

Tables

Schemes

Research Thesis: Declaration of Authorship

Print name: Hang Cheng

Title of thesis: **Nitrides or carbides coated on hard carbon for sodium ion batteries**

I declare that this thesis and the work presented in it are my own and has been generated by me as the result of my own original research.

I confirm that:

1. This work was done wholly or mainly while in candidature for a research degree at this University;

Where any part of this thesis has previously been submitted for a degree or any other qualification at this University or any other institution, this has been clearly stated;

2. Where I have consulted the published work of others, this is always clearly attributed;

Where I have quoted from the work of others, the source is always given. With the exception of such quotations, this thesis is entirely my own work;

I have acknowledged all main sources of help;

3. Where the thesis is based on work done by myself jointly with others, I have made clear exactly what was done by others and what I have contributed myself;
4. Parts of this work have been published as:

Hang Cheng, Nuria Garcia-Araez, Andrew L. Hector. Synthesis of Vanadium Nitride-Hard Carbon Composites from Cellulose and Their Performance for Sodium Ion Batteries, ACS Applied Energy Materials, **2020**, DOI: 10.1021/acsaem.0c00003.

Hang Cheng, Nuria Garcia-Araez, Andrew L. Hector and Samantha Soule., Synthesis of Hard Carbon-TiN/TiC Composites by Reacting Cellulose with TiCl4 Followed by Carbothermal Nitridation/Reduction, Inorganic Chemistry, **2019**,DOI: 10.1021/acs.inorgchem.9b00116.

Signature: Date:

Abstract

Sodium ion batteries (SIBs) are a promising substitute for lithium ion batteries (LIBs) because of the natural abundance and lower price of sodium. Hard carbon (HC), known as “non-graphitizable” carbon, is the most popular negative electrode material in SIBs. In this thesis, we investigate the development of composite materials in which the hard carbon is combined with a sodium conversion material with the aim of improving the capacity and cycling stability.

Hard carbon obtained from cotton wool at 1400 °C shows a best reversible capacity of 319 mA h g^{-1} at current of 20 mA g^{-1}. The sodium storage analysis is consistent with the traditional insertion/absorption mechanism in the hard carbon. The slope region is more related with interlayer distance and degree of graphitization while the plateau part is more related to the micropores size and volume.

An effective route to synthesis composites of metal nitrides and carbides with carbon was reported. Titanium tetrachloride is reacted with hydroxide groups on cellulose (cotton wool) before firing to convert the cellulose to hard carbon. Hard carbon-nanocrystalline titanium nitride composites with a good distribution of the titanium across the fibrous hard carbon structure were obtained by firing the treated cellulose under nitrogen. Hard carbon-nanocrystalline titanium carbide composites were obtained by carbonized under argon. Both composites show similar first cycle capacities to hard carbon, but the titanium nitride composite delivers a better capacity retention (85.2%) after 50 cycles than that of hard carbon (74.3 %). *Ex situ* grazing incidence XRD patterns of the HC-TiN composites suggest the reactions occurring only on the surface region of TiN.

VN-HC composites have been synthesised using the same pyrolysis process after reacting $VOCl_3$ with cellulose. The introduction of VN produces an increased capacity: with addition of 8.6 *wt*% VN, the hard carbon-based electrode achieves a first cycle reversible (oxidation, de-sodiation) capacity of 354 mA h g^{-1} at 50 mA g^{-1}, while with pure hard carbon it is 302 mA h g^{-1}. The additional specific capacity achieved upon addition of VN, compared with the pure hard carbon, is 605 mA h g^{-1} when referred to the mass of VN only, which is the highest capacity of VN materials in sodium-ion batteries reported to date. In addition, VN also improves the capacity retention with cycling: after 50 cycles the reversible capacity of hard carbon electrodes with 8.6 *wt*% VN is 294 mA h g^{-1}, while with pure hard carbon it is 239 mA h g^{-1}. Insights into the reaction mechanism are obtained by *ex situ* characterization of the discharged and charged electrodes.

Amorphous silicon nitride and silicon oxycarbides were obtained at 1200 °C. The as-prepared silicon nitride coated on hard carbon shows a reversible capacity of 351 mA h g^{-1} at 50 mA g^{-1}, better than that of 284 mA h g^{-1} from pure hard carbon. Furthermore, hard carbon coated with silicon nitride delivers a capacity retention of 85.4% in 50 cycles. The surface evolution of electrode before and after reduction cycling has been investigated by XPS measurement.

Acknowledgements

I would like to acknowledge the China Scholarship Council (CSC) and University Of Southampton for the financial support of my PhD study.

I would like to thank my supervisor, Professor Andrew L Hector and Dr. Nuria Garcia-Araez, for their guidance throughout the whole research project. I appreciate all their contributions of time and research ideas. I would not finish this thesis without their immense knowledge, patience and motivation.

I would extent my appreciation to my research progress examiner, Professor John R Owen, Dr. Geoff Hyett and Professor Magda Titirici, for their suggestions to solid my final version of thesis.

I would thank the members from Hector's group for their immense contribution to my personal and professional time in Southampton. I would like to acknowledge Sam Fitch, who has helped me conduct the experiment at the beginning of PhD study. I also like to thank the former group members, Dr. Samantha Soulé and Dr. Josh Whittam, for their kind advices in both my research and life. Other past and present group members that I have had the pleasure to work with are postdocs Andrew Lodge and Min Zhang, postgraduate students Samia Alsobhi, Gilles Moehl, Li Shao, Nabil Mohamed, Bowen Liu and Jon Allen, and the project students who have come through the lab.

I gratefully acknowledge the people who help me with the instrumental training and also the measurements in the Southampton.

Lastly, I would like to thank my family members for their support and encouragement. Thank you.

1. Introduction

1.1 Sodium ion batteries

Research on sodium ion batteries (SIBs) initially started parallel with that on lithium ion batteries (LIBs) through the 1980s.[1-4] Due to the rapid development and the successful commercial application of LIBs, research work on SIBs was stagnant for a long time. While LIB technologies are quite mature, there are potential problems with growing cost of lithium and non-abundant lithium supplies as large scale storage technology becomes necessary.[5] Lithium consumption was around 21280 tons in 2008 and the present lithium resource will run out in the next 50 years, which makes it important to find alternative materials in larger scale storage application. In contrast to lithium, sodium is one of the most abundant elements in the Earth's crust, and the sodium resources are basically unlimited everywhere in the world.[6] Compared to lithium ions (0.76 Å), sodium has larger ionic diameter (1.02 Å), which would inevitably affect the transport properties and interphase formation.[7] The difference of standard electrochemical potential between Li (-3.04 V) and Na (-2.71) is 0.3 V, and sodium is heavier than lithium (23 g mol^{-1} compared to 6.9 g mol^{-1}), suggesting the application of sodium would sacrifice too much energy density. However, the weight of cyclable lithium or sodium is a small fraction of mass of whole cells. Therefore, there should be no energy density consequence when transferring from LIBs to SIBs.[5] In addition, lithium undergoes alloying reactions with aluminium below 0.1 V vs Li/Li^+, but aluminium current collectors can be used in SIBs. Hence, the cost-effective aluminium can replace the copper as the anode current collector for SIBs. Researchers used layered oxides such as $LiCoO_2$, which is still widely used as high energy density positive materials, in the lithium batteries. However, the cobalt element is notable and should be replaced by other elements in large scale storage application. Although Na_xCoO_2 were reported in the early 1980s, researchers have fabricated iron- and manganese-base layered oxides in the sodium ion batteries in recent years. Based on the good electrochemical properties and abundant supply[6] of sodium, ambient temperature SIBs have gained more and more attention recently. Just with 87 papers on SIBs were published in 2011 and that rose to 2288 in 2019 (Data from Web of Science).

Sodium ion batteries are called secondary batteries as they can be repeatedly charged and discharged. For a secondary battery, electrodes are called positive/negative irrespective of whether device is being charged or discharged, in which the positive electrode operates at a higher potential while the negative electrode operates at a lower potential. Based on the discharge process, the positive electrode is generally referred to cathode with reduction reaction and the negative electrode is referred to anode with oxidation reaction. For the charge, the positive electrode is acting as the anode with oxidation reaction and the negative electrode is acting as the cathode with reduction reaction, respectively. The battery components of SIBs (Fig. 1-1) and LIBs are the same except for the ion carriers. The ion storage operation in SIBs is in similar to that in LIBs: sodium ions are shuttled back and forth from positive electrodes to negative electrodes through a non-aqueous (or aqueous) sodium ion electrolyte during discharge/charge.[8]

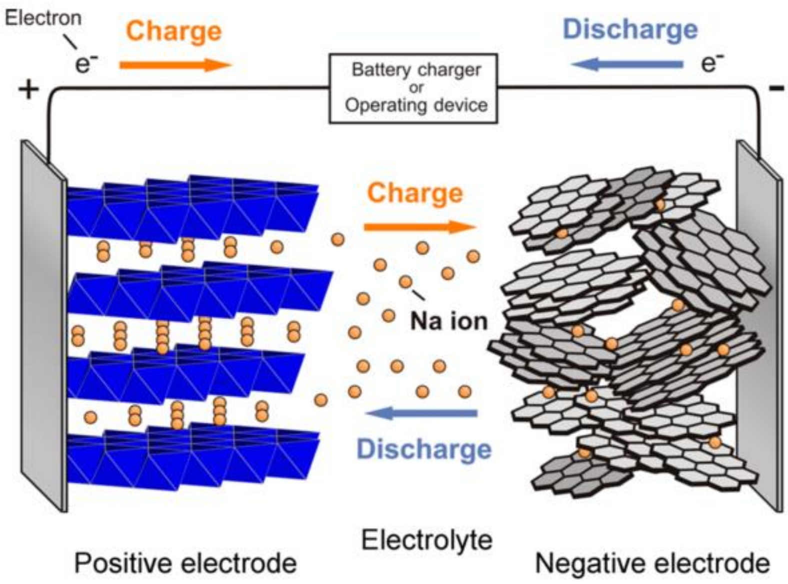

Figure 1-1 Schematic illustration of Na-ion batteries. Reproduced with permission[9]. Copyright (2014) American Chemical Society.

In a full cell, during the charging process (equation 1-1 and 1-2), sodium ions are extracted from the positive electrode and are inserted into negative electrode. Here composition NaM_xO_y represents a sodium metal oxide, and C represent a negative electrode carbon. The x, y and z represent the stoichiometric numbers. The electrons are transferred from positive to the negative electrode through the external circuit. In the discharging process (equation 1-3 and 1-4), it occurs conversely. The electrons are transferred from negative to positive electrode from external circuit. In our experiments, the half cells were assembled and tested to check the electrochemical properties. The carbon/metal nitride composites are referred to the positive electrode while the sodium metal is referred to as the negative electrode. In the discharging process, the electrons are given from sodium metal to composite via the external circuit. The sodium metal undergoes oxidation reaction and the carbon undergoes reduction reaction.

$$NaM_xO_y \rightarrow Na_{1-z}M_xO_y + zNa^+ + ze^{-1} \qquad \text{Equation 1-1}$$

$$C + zNa^+ + ze^{-1} \rightarrow NaC_z \qquad \text{Equation 1-2}$$

$$Na_{1-z}M_xO_y + zNa^+ + ze^{-1} \rightarrow NaM_xO_y \qquad \text{Equation 1-3}$$

$$Na_zC \rightarrow C + zNa^+ + ze^{-1} \qquad \text{Equation 1-4}$$

The electrolyte is positioned between the positive and negative electrodes, and it affects the battery behaviour as the electrolyte transfers and balances the charges in the forms of ions between the electrodes. Due to the working potential over the thermodynamic limit, the electrolyte decomposes and forms a solid electrolyte interface (SEI) on the surface of the electrodes. Once the SEI is formed on the electrode, the electrolyte is prevented from continuous decomposition and the system is kinetically stabilized.[10]

A good electrolyte should combine high ionic conductivity, good thermal stability, facile synthesis procedure, wide electrochemical stability window, etc.[11] To optimise the electrolyte properties, electrolyte composition with different salts, solvents and additives have been taken into account. The most common systems used in SIBs are $NaClO_4$ and $NaPF_6$ salts in carbonate ester solvents, such as propylene carbonate (PC), ethylene carbonate (EC) and diethyl carbonate (DEC) due to their high dielectric constant, low viscosity and stable electrochemical properties. In addition, by adding fluoroethylene carbonate (FEC), the EC would reduce solvent decomposition and form stable SEI ingredients.

Ether-based electrolytes make graphite usable in SIBs. Jache et al.[12] reported a co-intercalation of solvated sodium ion into graphite with formation of ternary graphite intercalation compounds:

$$Na^{+} + C + e^{-1} + solvent \leftrightarrow Na^{+}(solvent)C^{-1} \qquad \text{Equation 1-5}$$

Later, the Na^+-solvent co-intercalation was also investigated by XRD measurements, density functional theory and CV testing.[11] Recently, Cui et al. mixed various ether-based solvents with $NaPF_6$ to form a uniform and thin SEI layers, suppressing dendritic growth, which induces long-cyclic stability and high Coulombic efficiency.[13]

Ionic liquid-based electrolytes are composed of an organic cation and an inorganic/organic anion at room temperature. They are potential alternative electrolytes due to their wide electrochemical window, high boiling point and good thermal stability. Ding et al. applied N-propyl-N-methyl-pyrrolidinum ($Pyr_{1,3}$-) with NaFSI with optimized molar ratio to achieve conductivity of 15.6 mS cm^{-1} and an electrochemical window of 5.2 V *vs*. Na/Na^+ at 80 °C.[14]

A proper electrolyte is very important in SIBs to have long cycling stability and high capacity performance. Although various electrolyte systems have been reported, some fundamental studies such as relationship between molecular structures and electrolyte properties, the interface problem between electrolyte and electrode, and some safety properties still need to be investigated in the future.

For cathode materials, the sodium ions should be inserted reversibly at a voltage higher than 2 V vs Na metal. In that case, the volume change should be negligible if possible for the sodiation or desodiation in the host cathode materials. Early contributions to cathode materials, especially for layered oxides ($NaMO_2$, M: transition metal) in the SIBs have been made by Delmas, Hagenmuller and co-workers in the early 1980s.[15] The coordination environment of sodium metal in these layered materials can be described as either P (prismatic coordination) or O (octahedral coordination) depending on the stacking sequence of sodium ions between layers.[16] The structures of these sodium metal oxides (Fig. 1-2) are designated as P2 (ABBA stacking), O3 (ABCABC stacking) and P3 (ABBCCA stacking) from Delmas.[15,17] The phase transition occurs when extraction of sodium from O3- to P2-type phase, and the formation of prismatic sites is achieved by MO_2 slabs gliding without breaking M-O bonds. The P2-type layered structure has an open channel for sodium ions, since it has a lower diffusion barrier than that of O3-type layered system. On the other hand, the phase transition from P2- to P3-type is obtained by breaking/reforming M-O bonds with heating treatment.

Recently, similar to LIBs, various layered sodium metal oxides[18-20] have been widely and successfully applied in cathode materials as these materials show a minimal structural change with intercalation.

Iron- and manganese-based layered oxides are widely used as sodium insertion hosts as the metals have high elemental abundance in the Earth's crust. The $NaFeO_2$ is a typical O3-type layered oxide and can be obtained by solid-state reaction. The sodium extraction from $NaFeO_2$ was first investigated by Takeda in a Li/$NaFeO_2$ cell.[59] Reversible discharging/charging process was first demonstrated by Okada in Na/$NaFeO_2$ cell. A reversible capacity of 80 mA h g^{-1} was achieved by extracting sodium from $NaFeO_2$ and inserting sodium into the resultant $Na_{0.7}FeO_2$, suggesting around 0.3 mol of sodium is reversibly reacted in the discharging/charging process. The electrode performances of O3- and P2-type $NaMnO_2$ were investigated in early 1980s but the reversible capacities were not good enough as electrode materials. The P2-$NaMnO_2$ shows better electrochemical performance than that of O3-$NaMnO_2$ due to the higher ionic conductivity, indicating the different sodium migration path in different layered type materials.[69] P2-type $Na_{2/3}[Fe_{1/2}Mn_{1/2}]O_2$ and O3-type $Na[Fe_{1/2}Mn_{1/2}]O_2$ were prepared by changing the ratio of sodium/(iron and manganese). These materials deliver large reversible capacity and also high operating voltage, which induces much research interest on $Na_x[Fe_yMn_{1-y}]O_2$ with different chemical compositions. A reversible capacity of 190 mA h g^{-1} with an average voltage of 2.75 V *vs* Na can be obtained with P2-$Na_x[Fe_{1/2}Mn_{1/2}]O_2$. The energy density (520 mW h g^{-1} *vs* Na) is comparable to LiFePO4 (530 mW h g^{-1} *vs* Li), which makes it a promising positive material for sodium ion batteries.

Layered Na_xCoO_2 is the oldest oxide as the sodium insertion host. P2- and P3-type layered Na_xCoO_2 were first applied as positive materials in SIBs in 1988.[83] Fig. 1-3 shows the discharging/charging curves of O3-, P2- and P3-type Na_xCoO_2, with very similar voltage profile, operating voltage and phase transition behaviour at lower sodium content range ($x<0.7$). The O3-type Na_xCoO_2 is energetically stable than P2-type at higher sodium content range ($x>0.8$), which is revered in contrast to iron-, manganese-based layered oxides, suggesting different sodium insertion kinetics in the high sodium content range.

Other layered binary/ternary metal oxides without cobalt system have also been reported. The O3-type $Na[Fe_{0.4}Ni_{0.3}Mn_{0.3}]O_2$ layered material delivers good electrode performance with small polarization.[117] O3-type $Na_{1-x}[Ni_{1/2}Mn_{1/2}]O_2$ shows O3-P3 phase transition with a reversible capacity of 185 mA h g^{-1}. With the oxidation of Ni^{2+}/Ni^{4+}, the sodium ions are extracted without irreversible structural change.[125]

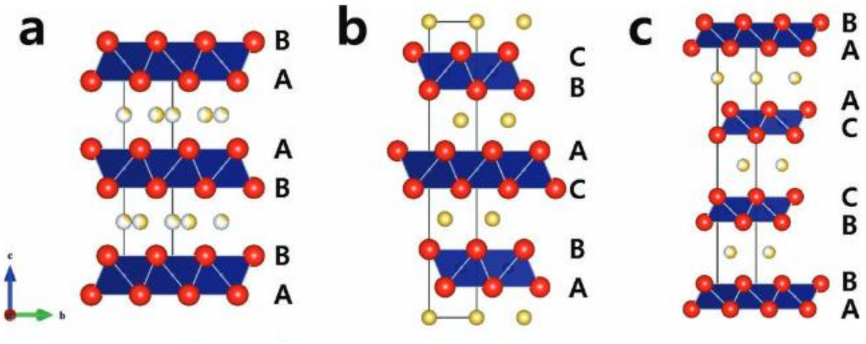

Figure 1-2 Crystal structures of (a) P2-Na$_x$CoO$_2$, (b) O3-Na$_x$CoO$_2$ and (c) P3-Na$_x$CoO$_2$ (Na: yellow, Co: blue, O: red). Reproduced with premission[21]. Copyright (2012) Wiley-VCH Verlag GmbH & Co. KGaA.

However, the research for an anode material with good structural stability and large reversible capacity is still a big problem in development of SIBs. Graphite, which is the accepted anode material in LIBs, does not show good reversible capacity due to the ionic radius of sodium (1.02 Å), which is 55% larger than that of lithium (0.76 Å).[22] First-principles calculation shows that the chemical bonding between alkali metal ion and carbon atoms is the major reason for alkali metal ion intercalation in graphite.[23,24] The formation energy of NaC_6 is positive while that of LiC_6 and KC_6 are negative, suggesting the graphite is suitable for Li/K intercalation but not for Na. Although alternatives including metal alloys[25], metal oxides[26], metal phosphides[27], and organic compounds[28] have been investigated, carbon-based materials[29-32] and especially hard carbon materials are very attractive anode materials in SIBs due to the good conductivity and the high reversible capacity at low voltage.[33]

1.2 Hard carbon

1.2.1 Definition of hard carbon

Graphite, (Fig. 1-3a) contains hexagonal carbon layers, which are stacked in parallel and bounded by weak Van der Waals forces that allow their gliding under mechanical stress.[33,34] X-ray diffraction (XRD) pattern (Fig. 1-4a) shows two sharp peaks around 2θ=26° and 55°, which can be attributed to interlayer distance in 002 and 004 reflection, respectively. A series of inter-plane and intra-plane peaks can be found in the range 42-47°. Non-graphitic carbon consists “soft carbon” and “hard carbon” (Fig. 1-3b and c). The Van der Waals forces in “soft carbon” allow enough mobility of carbon layers at high temperature (over 2500 °C) to increase their crystallinity toward graphite.[35] Soft carbon (Fig. 1-4b) has a broader and lower position peak in 002 reflection, corresponding to the crystallinity loss in the stacking direction. The inter-plane reflections in the range 42-47° disappear, which can be attributed to the total loss of plane-to-plane coherency. Only the intra-plane reflection (100) shows up but owns a broader shape, corresponding to the unstretched intra-layer strength and a loss of in-plane crystallinity. “Hard carbon” (Fig. 1-4c) has a high degree of defect structure and this highly disordered structure inhibits the gliding of graphene layers with heat treatment.[36] The 002 reflection shows broader peak and shifts to lower position compared to soft carbon, suggesting reduced crystallinity in the stacking direction and enlarged interlayer distance in the hard carbon. The 100 reflection almost stays the same, which is due to the similar intra-layer strength and in-plane crystallinity for soft and hard carbon.

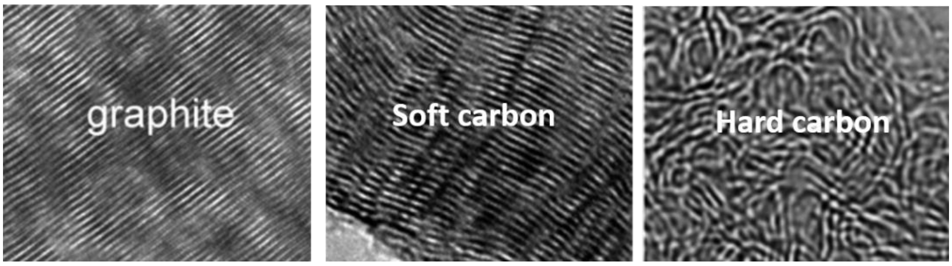

Figure 1-3 High-resolution TEM images of different types of carbon. Reproduced with permission[37]. Copyright (2017) American Chemical Society.

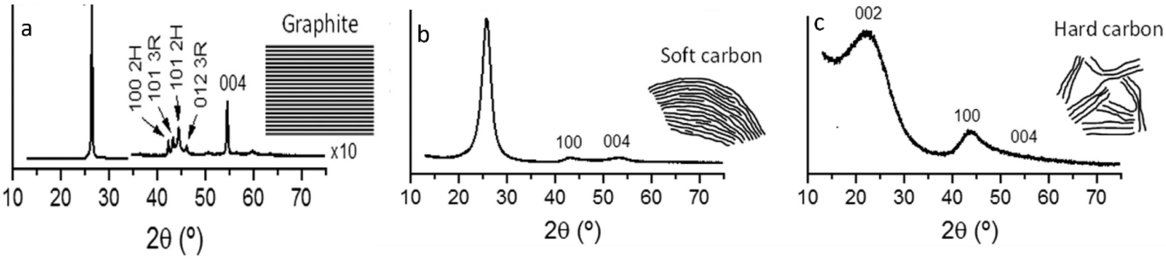

Figure 1-4 XRD patterns of (a) graphite, (b) soft carbon and (c) hard carbon. Reproduced with premission[33]. Copyright (2017) Wiley-VCH Verlag GmbH & Co. KGaA.

The c-axis length (L_c) and a-axis length (L_a) of the graphitic domains are measured by Scherrer equation with the full width at half-maximum of 002 at 2θ~23 and 100 at 2θ~43. The calculation equations are as follows:

$$L_a = 1.84\lambda/(\beta_{100}\ \cos\theta_{100}) \qquad \text{Equation 1-6}$$

$$L_c = 0.89\lambda/(\beta_{002}\ \cos\theta_{002}) \qquad \text{Equation 1-7}$$

Where λ is the wavelength of the radiation, β_{002} and β_{100} are the full width at half-maximum (fwhm) of 002 and 100 peaks, respectively. θ_{002} and θ_{100} are the corresponding scattering angles.

1.2.2 The synthesis of hard carbon

Disordered carbons are typically obtained by pyrolysis of organic precursors at high temperatures (500-3000 °C). R. Franklin[38] proposed that the structure of carbons obtained with pyrolysis depends not only on temperature but also on the nature of the substance. According to his report, the formation of hard carbon is favoured by the presence of oxygen or by the shortage of hydrogen in the raw precursor. Hydrogen-rich precursors such as polyvinylchloride $(C_2H_3Cl)_n$ form cross-linked carbons that are subjected to continual reduction or destruction because of the excess of hydrogen in the raw material, leaving a relatively compact carbon. Oxygen-rich precursors such as cellulose $(C_6H_{10}O_5)_n$, resorcinol-formaldehyde and sugar $(C_6H_{12}O_6)_n$ tend to form hard carbon. During the pyrolysis of these precursors, the hydrogen will be released with the formation of H_2O or HCl. The formation gas produces porous structure, leading to a low-density carbon network.

Researchers reported phenolic resin-derived hard carbon shows good sodium storage performance due to the controllable carbon physical and chemical properties.[39-42] From a green and sustainability point of view, biomass-derived hard carbons are promising not only they show good electrochemical performance but also reduce the quantities of biowaste produced every year. Various biomass materials like argan shells[43], grass[44], leaf[45] and rice husk[46] have been applied as precursors to synthesize hard carbon. Cotton wool[47] is another promising precursor owing to its low cost and abundant supply. In this work, resorcinol-formaldehyde and cotton wool derived hard carbon have been produced at high pyrolysis temperature. Physical properties and electrochemical performance of these hard carbons have been investigated to identify which material is better to use in the composite.

1.2.3 Research on electrochemical performance of hard carbon

Theoretical capacity is the amount of charge (Coulombs) can be provide in the battery by a given active material. However, the practical capacity is normally less than the theoretical capacity because not all the material in the cell can be accessible. To test the electrochemical performance of hard carbon, researchers typically apply galvanostatic testing to obtain the capacity using the equation $Q=I*t$, where Q is electric charge measured in Ah, I is current and t is time. Normally, the capacity can be divided either by volume or by mass, named specific capacity (Ah kg^{-1} or Ah m^{-3}), to compare the electrochemical performance between different materials with different mass or volume. The specific capacity by mass is much easier to measure, but the specific capacity calculated by volume is more useful when applied in small places like residential buildings.

Theoretical energy is the energy that can be provided by a given cell. Energy is the integral of voltage with charge (or capacity, equation 1-7), which is usually quoted in Wh (1 Wh=1 W *3600 s=3600 J). Similar to capacity, the energy can be divided either by volume or by mass, named specific energy or known as energy density (Wh kg^{-1} or Wh m^{-3}).

$$\text{Energy} = \int V dq \qquad \text{Equation 1-8}$$

Power is the amount of energy per unit time (equation 1-8). Power is usually quoted in W (1 W=1J s^{-1}). Power density (W kg^{-1} or W m^{-3}) is the power that be divided either by volume or by mass.

$$\text{Power} = \frac{dEnergy}{dt} = \frac{\int Vdq}{dt} = VI, \text{ if the V is the constant.} \qquad \text{Equation 1-9}$$

In the following discussion parts, two types of plots (Fig. 1-5) will be presented to describe the relationship between the specific capacity and potential (vs Na/Na$^+$). As shown in Fig. 1-5a, the potential (vs Na/Na$^+$) decreases to near 0 V (vs Na/Na$^+$) in the reduction (discharge) process, and the capacity increases to around 200 mA h g^{-1}. Then in the oxidation (charge) process, the potential (vs Na/Na$^+$) goes back to around 1.5 V (vs Na/Na$^+$), and the capacity increases from 0 to around 150 mA h g^{-1}, lower than that after first reduction process. It is noticed that the reduction process of negative electrode in the full cell is charging while that of negative electrode in the half cell is discharging. The ratio of oxidation capacity to reduction capacity after first cycle is the initial Coulombic efficiency (ICE), which is used to describe the reversible capacity performance in the battery. The higher the ICE, the more reversible capacity will be obtained. The other type of plot that is commonly used has been shown in Fig. 1-5b. The reduction process is the same with that shown in Fig. 1-5a. During oxidation process, however, the capacity value decreases from first reduction capacity (around 250 mA h g^{-1}) to around 60 mA h g^{-1}, highlighting the irreversible part of the capacity.

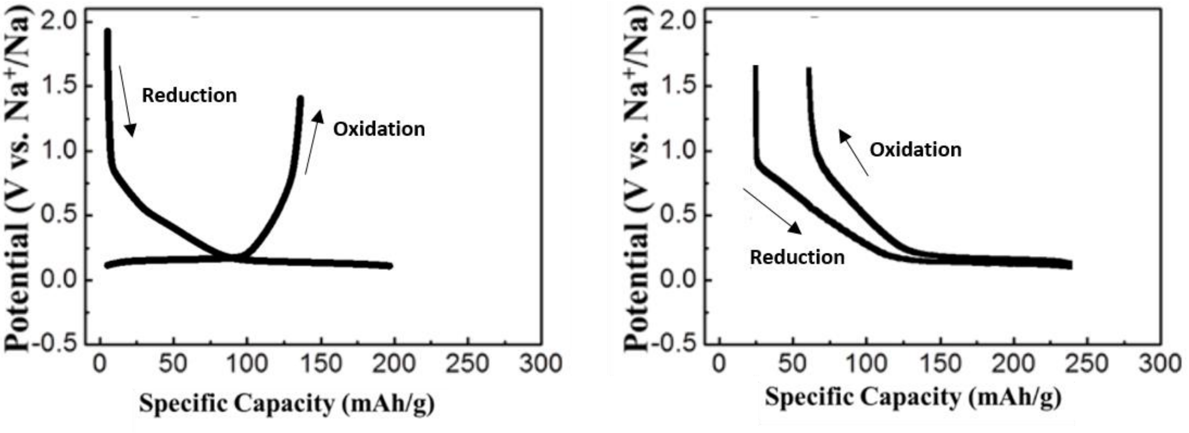

Figure 1-5 Two different plots to describe the reduction and oxidation process in SIBs.

In addition, different currents with related specific capacity are often plotted in one graph. Rates of charge or discharge are often described in terms of C-rates, by dividing the theoretical capacity of the material (mA h g^{-1}) by the applied current (mA g^{-1}). Hence at 1 C the electrode is expected to fully charge or discharge in 1 h, whereas at 2 C this would take 0.5 h.

Graphite is widely used in lithium ion batteries with the graphite intercalation compound LiC_6.[48] However, the sodium intercalation content in graphite is very small (NaC_{64}) with conventional electrolytes as reported.[49] The ionic radius of the sodium ion (0.95 Å) is larger than that of the lithium ion (0.60 Å). Generally the interlayer distance of graphite is around 0.34 nm, which is too small to accommodate the sodium ions, and the minimum interlayer distance of 0.37 nm is required for sodium insertion by theoretical calculations.[50] The calculation of energy cost shows that the energy cost curve for sodium insertion into carbon is steeper than that for lithium insertion. When the interlayer space increases to 0.37 nm, the energy barrier is low enough to conquer and the expanded graphite can be used as sodium insertion material similar to lithium insertion into graphite (LiC_6).[50]

Instead, some researchers reported the non-graphitic carbon materials in SIBs. In 1993, Doeff *et al*.[51] first demonstrated sodium ion insertion/disinsertion reaction into the disordered soft carbon obtained from petroleum coke, which shows the possibility of application of disordered carbons in SIBs. In 2000, Stevens and Dahn[52] first reported the electrochemical reversibility of Na insertion reaction into hard carbon obtained by pyrolysis of glucose at 1000 ℃. Although the hard carbon electrode showed a reversible capacity of 300 mA h g^{-1}, the current (around 5 mA g^{-1}) was small and needed to be improved.

Later some studies revealed that the reversible capacity links to the microstructure (e. g. d_{002} interlayer distance and degree of graphitization) of the hard carbon. Fig. 1-6a shows the typical XRD pattern of hard carbon. As discussed above, the d_{002} interlayer distance is related with the peak position around 2θ=23° in the XRD pattern. Fig. 1-6b and c shows the different d-spacing and related specific capacity of hard carbon with different pyrolysis temperature. Generally, the d-spacing is from 3.7 to 4.0 Å and decreases with rise of temperature. It is noted that the different precursor also affects the d-spacing under the same pyrolysis temperature. It has been reported the larger d-spacing is better for the insertion/extraction of sodium between the graphene layers. However, the correlation between the d_{002} interlayer distance and reversible capacity is not clear though the interlayer distance wider than 3.70 Å is appropriate for obtaining good reversible capacity (Fig. 1-6c). It's reasonable that even the lower temperature produces greater d_{002} interlayer distance, hard carbon obtained at this lower temperature will remain more functional groups on the surface, causing high irreversible capacity. For example, argan shell based hard carbon shows a higher capacity when it has smaller d_{002} interlayer distance.[43]

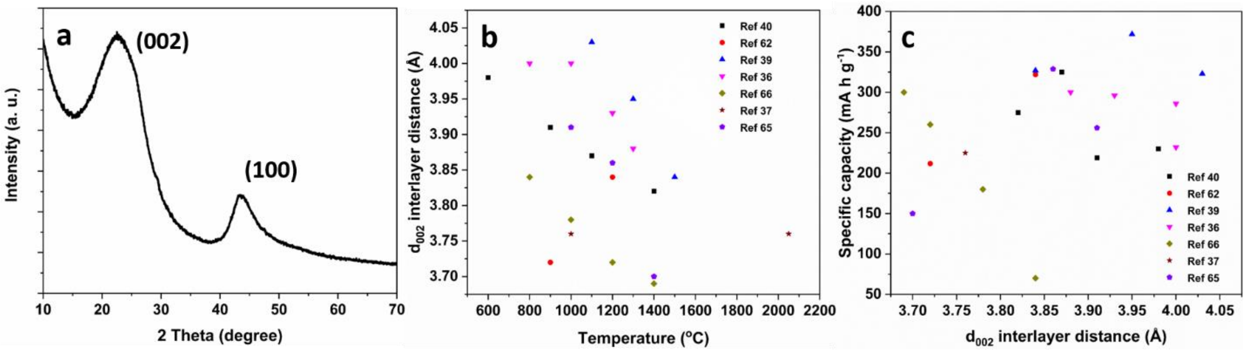

Figure 1-6 (a) Typical XRD pattern of hard carbon, (b) relation between d_{002} interlayer distance and pyrolysis temperature and (c) correlation between specific capacity and d_{002} interlayer distance.

The degree of graphitization can be investigated by Raman measurement. As shown in Fig. 1-7a, the spectrum exhibits broad disorder-induced D-bands at 1350 cm^{-1} and graphitic-induced G-band at 1580 cm^{-1}. It is obvious that the more defective structures are favourable for the sodium insertion into the carbon structure.[53] The intensity of I_D/I_G indicates the degree of graphitization and normally decreases with the rise of pyrolysis temperature due to the increase degree of order (Fig. 1-7b).[54-56] However, some researchers also reported the abnormal tendency with increasing treatment temperature.[47,57] The correlation between the degree of graphitization and reversible capacity is not clear though the highly disordered structure is needed in hard carbon (Fig. 1-7c).

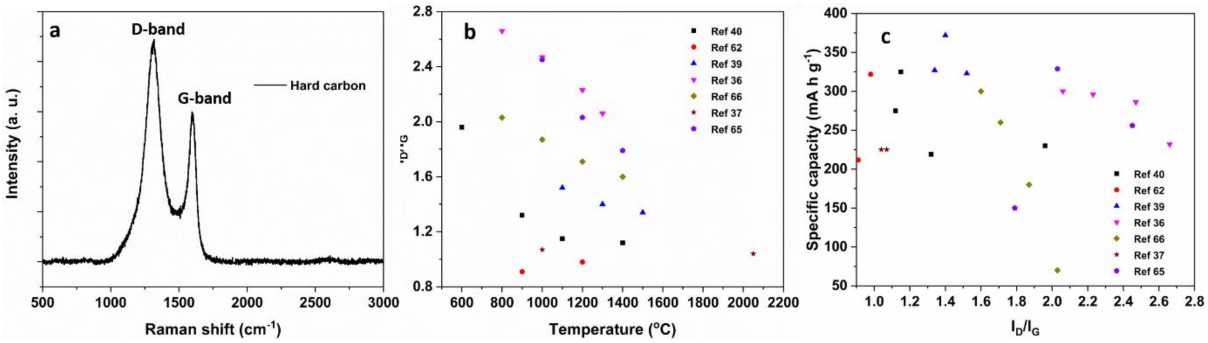

Figure 1-7 (a) Typical Raman spectrum of hard carbon, (b) correlation between degree of graphitization and pyrolysis temperature and (c) correlation between reversible capacity and degree of graphitization.

Some works also reported the specific morphology in hard carbon has a positive effect on sodium storage. The morphology links to the sodium diffusion path, providing a better contact to increase the electronic conductivity or allowing solvent availability to enhance the mass transport at high current. Thomas and Billaud[58] prepared three different types of hard carbons (saccharose-coke derived at different temperature, cellulose-derived) and compared their electrochemical properties. The best electrochemical performance was obtained from a cellulose-derived carbon electrode, with a reversible capacity of 279 mA h g^{-1} at the current of 7 mA g^{-1}. The discussion suggests the most suitable hard carbon materials should possess significant microporous structure. Wenzel *et al.*[59] showed good rate capacity around 120 mA h g^{-1} at 74.4 mA g^{-1} (0.2 C) after 40 cycles from hierarchically porous hard carbon (Fig. 1-8a). Maier *et al.*[60] first indicated the excellent rate performance of hollow carbon nanospheres as SIB anode materials (Fig. 1-8b). The hollow spherical carbon electrode delivered reversible capacities of 223 mA h g^{-1} at 50 mA g^{-1} and ~50 mA h g^{-1} at 10 A g^{-1}, respectively, attributed to rapid mass transport to a large surface area with lots of active sites.[61] Hou *et al.*[62] reported 3D porous carbon quantum dots (Fig. 1-8c) with rate performance of 104.1 mA h g^{-1} at 5 A g^{-1}, which may be in related to the large surface area and porous structure, facilitating the transport of sodium ions.[63] Pyo *et al.*[64] prepared sucrose-based hard carbons with various porosities by adding different amounts of bicarbonates, which can decompose with gas evolution to form submicron-sized and nanometric pores. This optimal nanoporosity hard carbon shows a reversible capacity of 324 mA h g^{-1} at 20 mA g^{-1}, and an initial cycle Coulombic efficiency of 81%, better than any other hard carbons with different porous structure. It suggests that the optimization of a nanoporous architecture is crucial in order to prepare highly efficient hard carbon.

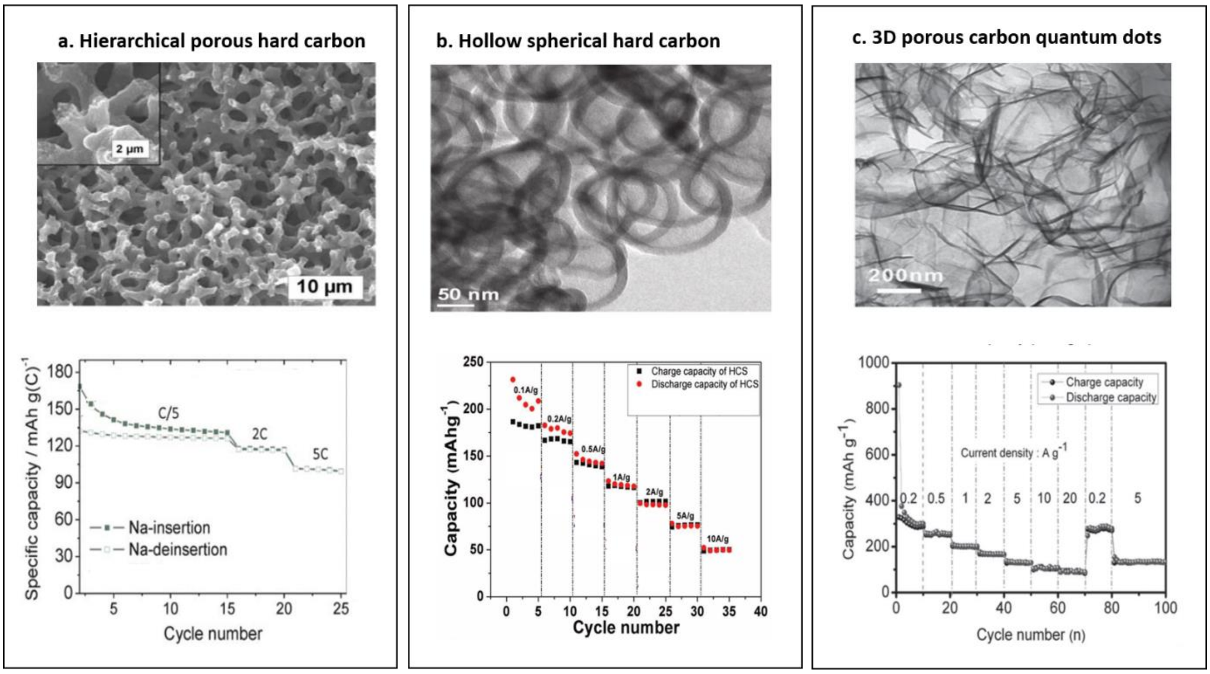

Figure 1-8 Morphological characterization (upper) and related capacity performance (lower) of (a) hierarchical porous hard carbon, Reproduced with permission[59], Copyright (2011) Royal Society of Chemistry; (b) hollow spherical hard carbon, Reproduced with permission[60], Copyright (2012) Wiley-VCH Verlag GmbH & Co. KGaA; and (c) 3D porous carbon quantum dots, Reproduced with permission[62], Copyright (2015) Wiley-VCH Verlag GmbH & Co. KGaA. The current used for hierarchical porous carbon electrode is 0.2 C (74.4 mA g^{-1}).

While large surface areas and specific porous structures improve the mass transport and then increase the sodium storage, most of these hard carbon electrodes present a low initial Coulombic efficiency (ICE), which reduces the recyclable sodium ions and thus decreases the total capacity performance. This poor ICE is mostly due to the formation of solid electrolyte interface (SEI) but also attributed to some ions being trapped in the bulk of the materials.[54] The capacity loss due to the formation of SEI is usually related with the BET surface area of the electrode[54,51] though the side reactions (e.g. the reaction between functional group OH- and sodium) also affect the ICE.[8,47,65] Ji and co-workers[66] prepared graphene oxide doped hard carbon (G-HC) by adding graphene oxide (GO) into sucrose before high temperature treatment. The doped GO can effectively inhibit foaming during caramelization of sucrose, leading to a surface area of 5.4 m^2 g^{-1}, much lower than that of 137.2 m^2 g^{-1} from the sucrose-derived hard carbon (Fig. 1-9a). In contrast, the FCCE value increased from 74% to 83%, which is one of the highest ICE values reported for hard carbon anodes in SIBs (Fig. 1-9b).[47] Hu *et al.* [67] also obtained a hugely improved ICE value from 25% to 72 % by chemical pre-treatment of a wood precursor of hard carbon (Fig. 1-9d). With the treatment of 2, 2, 6, 6-tetramethylpiperidine-1-oxyl (TEMPO), fewer nanosized pores were generated in the oxidized wood fiber, resulting in a lower surface area of 126 m^2 g^{-1} than that of 586 m^2 g^{-1} without treatment of TEMPO (Fig. 1-9c).

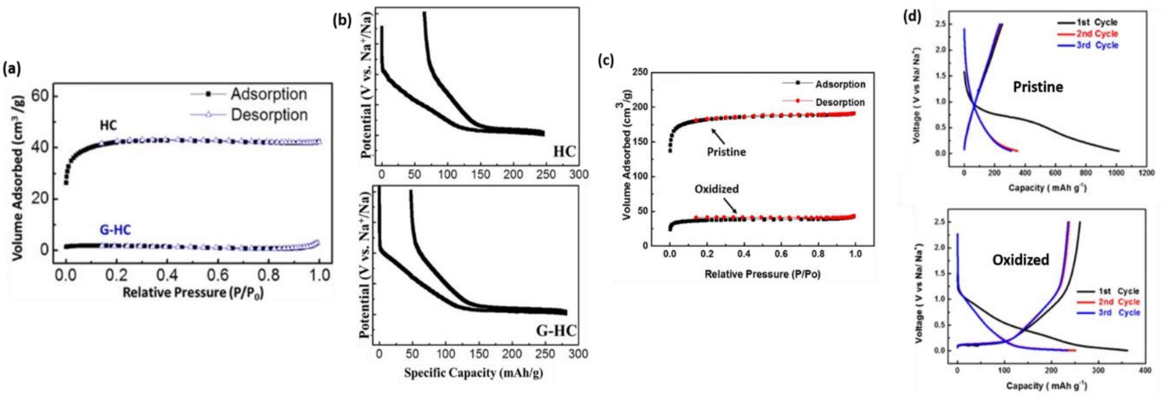

Figure 1-9 (a) Nitrogen adsorption/desorption isotherms and (b) potential profiles for HC and G-HC, Reproduced with permission[66], Copyright (2015) American Chemistry Society; (c) Nitrogen adsorption/desorption isotherms and (d) potential profiles of oxidized carbon paper and pristine carbon paper, Reproduced with permission[67], Copyright (2015) American Chemistry Society. The current is 20 mA g^{-1}.

Overall, the correlation between BET surface area and capacity performance is not always negative but the surface area lower than 100 m^2 g^{-1} is more favourable to get better electrochemical performance (Fig. 1-10).

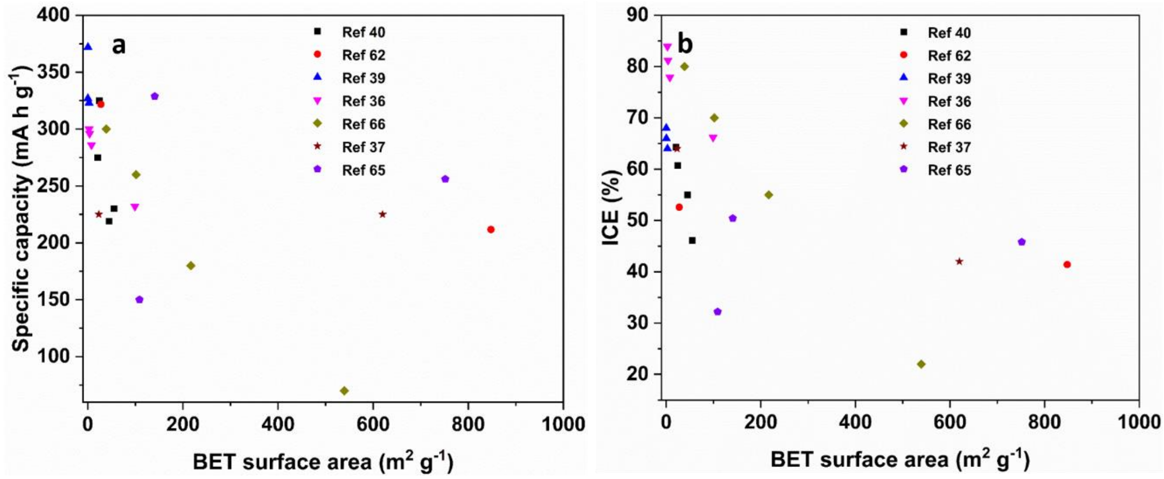

Figure 1-10 (a) Correlation between BET surface area and specific capacity, (b) correction between BET surface area and initial Coulombic efficiency (ICE).

In conclusion, hard carbon materials obtained with different precursors have been produced and their electrochemical performance have been also discussed previously. It seems that the large d_{002} interlayer distance, low graphitization degree, porous structure and low surface properties can affect the sodium storage in hard carbon. Therefore, the design of hard carbon with appropriate porous structure and surface area is necessary in SIBs. Here a summary of the capacity from some typical hard carbons has been shown in Table 1-1.

Table 1-1 Capacity review of hard carbon in SIBs reported in the literatures.

Materials	Precursor	Mas loading (mg cm^{-2})	Electrode compose (A:B:C)[†]	Electrolyte	Voltage windows	Oxidation capacity	ICE(%)	Reference
Hard carbon	Cotton wool	2-2.5, Swagelok cells	95:5:0	1 M NaClO4 in EC/DEC	0.005-2 V	319 mA h g^{-1} at 20 mA g^{-1}	71.8	This work
Carbon nanofibers	Cellulose nanofibres	1-1.2, coin cells (CR2032)	80:10:10	1 M NaClO4 in EC/PC	0.01-2 V	255 mA h g^{-1} at 40 mA g^{-1}	58.8	[68]
Carbon membranes	Leaf	N/A, coin cells (CR2032)	100:0:0	1 M NaClO4 in EC/DEC	0-2.5 V	270 mA h g^{-1} at 40 mA g^{-1}	74.8	[45]
Carbon nanotubes	Cotton	2.5-3.5, coin cells (CR2032)	95:5:0	0.8 M NaPF6 in EC/DMC	0-2 V	315 mA h g^{-1} at 30 mA g^{-1}	83	[69]
Nitrogen-doped carbons	Honey	~1.2, coin cells (CR2032)	80:10:10	1 M NaClO4 in EC/DEC	0.005-2.9 V	394 mA h g^{-1} at 100 mA g^{-1}	43.7	[70]
Carbon sheets	stalks	N/A, coin cells (CR2032)	80:10:10	1 M NaClO4 in EC/DEC	0.01-3 V	260 mA h g^{-1} at 100 mA g^{-1}	52.6	[71]
Carbon nanosheets	Peat moss	~1, coin cells (CR2032)	80:10:10	1 M NaClO4 in EC/DEC	0.001-2.8 V	298 mA h g^{-1} at 50 mA g^{-1}	57.5	[55]
Hard carbon	Switchgrass	0.5, coin cells (CR2025)	80:10:10	1 M NaClO4 in EC/DEC	0.01-2 V	298 mA h g^{-1} at 50 mA g^{-1}	64	[44]
Actived hard cabron	Argan shells	1.2-2, coin cells (CR2032)	90:10:0	1 M NaPF6 in EC/DEC	0-2 V	333 mA h g^{-1} at 50 mA g^{-1}	79.0	[43]
Hard carbon	Peanut shells	~1.5, coin cells (CR2025)	80:10:10	1 M NaClO4 in EC/PC	0.001-2 V	261 mA h g^{-1} at 100 mA g^{-1}	58±2	[72]
3D free-standing hard carbon	hemp haulm	N/A, coin cells (CR2032)	100:0:0	0.8 M NaClO4 in DMC	0.01-3 V	256 mA h g^{-1} at 37.4 mA g^{-1}	N/A	[73]
Hard carbon	Lotus seedpod	N/A, coin cells (CR2025)	80:10:10	1 M NaClO4 in PC with 2% FEC	0.01-2.5 V	328.8 mA h g^{-1} at 50 mA g^{-1}	50.4	[74]
Hard carbon	Mangosteen shell	~2.5, coin cells (CR2032)	80:10:10	1 M NaClO4 in EC/PC	0-2 V	330 mA h g^{-1} at 20 mA g^{-1}	83	[75]

†, A:B:C represents weight percentage of active materials, binder and conductive carbon. EC=ethylene carbonate, DEC=diethyl carbonate, PC=propylene carbonate, DMC=dimethyl carbonate, FEC=fluoroethylene carbonate. N/A=not available

1.2.4 Sodium storage mechanism in SIBs

In 2000, Stevens and Dahn[52] proposed the "card house" mechanism (Fig. 1-11a) for sodium ion storage in hard carbons, which contains the sodium insertion between parallel graphene layers (the slope voltage region) and the sodium adsorption process in the nanopores of the disordered carbon structure (the plateau region).[52,76,77] In 2002, Thomas and Billaud[58] showed a similar mechanism of sodium insertion into hard carbon. In the charge-discharge profile, the low-potential plateau can be also attributed to sodium intercalation into carbon nanopores, while the slope region contains both sodium insertion between graphene sheets and interactions between the sodium and hetero-elements such as residual oxygen or hydrogen on the hard carbon. Fig. 1-11b describes the traditional insertion/absorption mechanism of sodium storage in hard carbon. In that case, the slope region is more related with interlayer distance and degree of graphitization while the plateau part is more related to the micropores size and volume.

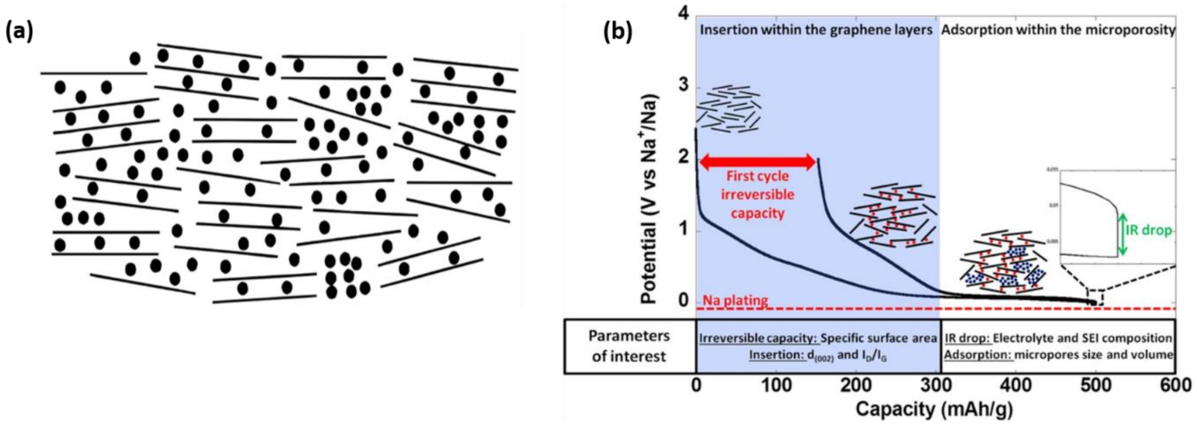

Figure 1-11 (a) The "Card-house" model for sodium filled hard carbon. Reproduced with permission[52], Copyright (2000) The Electrochemical Society; (b) Sodium storage mechanism in hard carbon.[54]

Fujiwara *et al.*[78] further confirmed the structural changes that occur during sodium insertion between graphene layers by using X-ray diffraction (XRD) measurements. They found that the broad peak at 2θ=23.4° (Fig. 1-12a) shifted to a lower angle at 2θ=ca. 21-22 °after reduction of hard carbon electrode to 0.2 eV*vs* Na/Na^{+}, indicating expansion of the space between the graphene layers, which is ascribed to sodium insertion between parallel graphene sheets in a similar way to that in LIBs.[79] When the hard carbon electrode was oxidized back to 2 eV, the peak position went back to the same position to that of the pristine, showing the reversible sodium insertion/disinsertion process from the graphene layers. The authors also investigated the nanopores structural change during the charge-discharge process in hard carbon electrodes with *ex situ* small angle X-ray scattering (SAXS). The scattering intensity around 0.03-0.07 Å^{-1} (Fig. 1-12b), in corresponding to the nanopores with a diameter around 14 Å in hard carbon, decreased with reducing voltage from 0.20 to 0.00 V. This shows a decrease in the electron density between the carbon matrix and nanopores, ascribed to the sodium insertion into the nanopores.

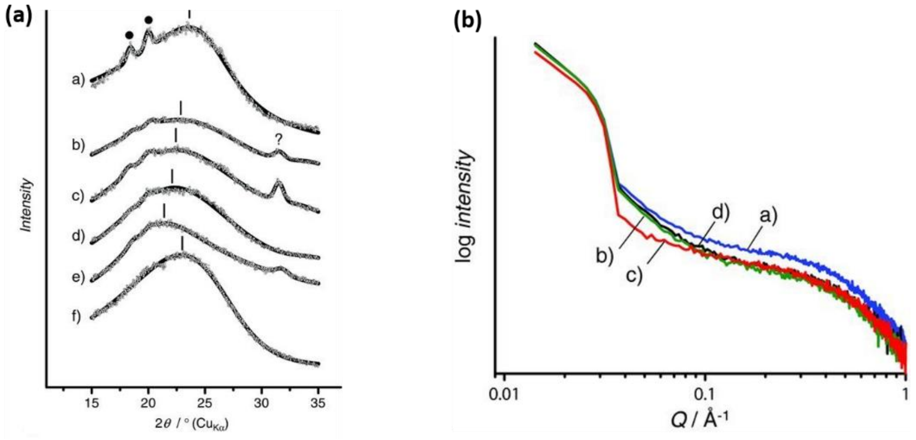

Figure 1-12 (a) *Ex situ* XRD patterns for hard-carbon electrodes: a) pristine electrode, galvanostically reduced to b) 0.40 V, c) 0.20 V d) 0.10 V, e) 0.00 V, and f) oxidized to 2.00 V after reduction to 0.00 V.(• PVDF binder, ? unknown). (b) Ex situ SAXS patterns for hard-carbon electrodes: a) pristine, galvanostically reduced to b) 0.20 V and c) 0.00 V, and d) re-oxidized to 2.00 V. Reproduced with pdrmission[78], Copyright (2011) Wiley-VCH Verlag GmbH & Co. KGaA.

Reddy et al. first applied *in situ* Raman measurements and density functional theory (DFT) to monitor the sodium insertion into hard carbon in the slope region.[53] Two peaks in the spectra (Fig. 1-13) around 1600 and 1330 cm^{-1} correspond to G-band and D-band as discussed above. During the charge-discharge process, the position of the D-band remains the same while the intensity decreases from OCV of 2.42 V down to about 0.2 V, and then disappears. Interestingly, the peak of G-band shifts to lower frequency with increase of sodium insertion but stops shifting when the voltage approaches to plateau region (Fig. 1-13c). Later DFT calculation shows a lower G-band frequency with increase of sodium contents in hard carbon, which agrees well with the shifting of G-band to lower frequency in the experiment. Quantitative analysis suggests the composition of roughly NaC_{24} is reached after sodium insertion between the graphene layers.

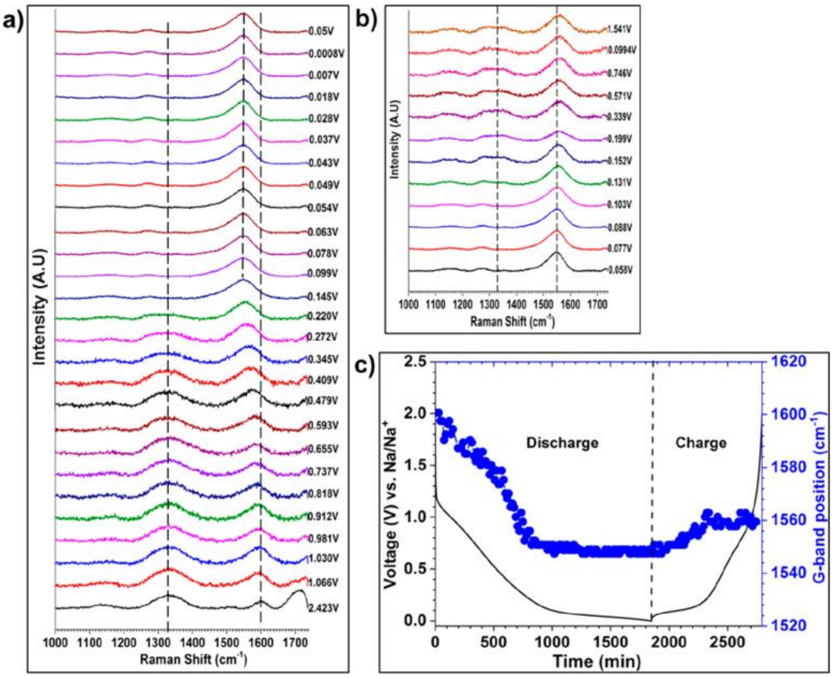

Figure 1-13 *In situ* Raman studies. Evolution of Raman spectra collected in operando during (a) discharge from OCV to 0.0 V, (b) charge from 0.0 to 2.0 V (only selected spectra are shown for brevity), and (c) evolution of the G-band position as a function of discharge and charge. The discharge−charge curves were obtained at RT, at a current density of 10 mA g^{-1} and in the voltage window of 0.0−2.0 V vs Na/Na$^+$. Reproduced with permission[53]. Copyright (2018) American Chemical Society.

Recently, Titirici *et al.* reported a revised mechanism model for sodium insertion in hard carbons by ex-situ ^{23}Na solid-state NMR techniques.[80] Fig. 1-14a shows that a broad peak appears in lower temperature treated carbon and shifts to 1135 ppm (metallic sodium exhibits a peak at 1135 ppm[81]) when the carbon is obtained at higher pyrolysis temperature. With the lowest pyrolysis temperature, the treated sample has no quasi-metallic peak and also the plateau capacity, implying that sodium storage in slope region in related to ionic in nature. Fig. 1-14b suggests that the quasi-metallic sodium corresponding to the increasing pore size and can only be observed in materials which have a plateau capacity. The results clearly demonstrates that the pore filling is the final sodiation process which happens in the plateau region, which in agree with the research works by Stevens, Dahn[76] and Morita et al.[82]

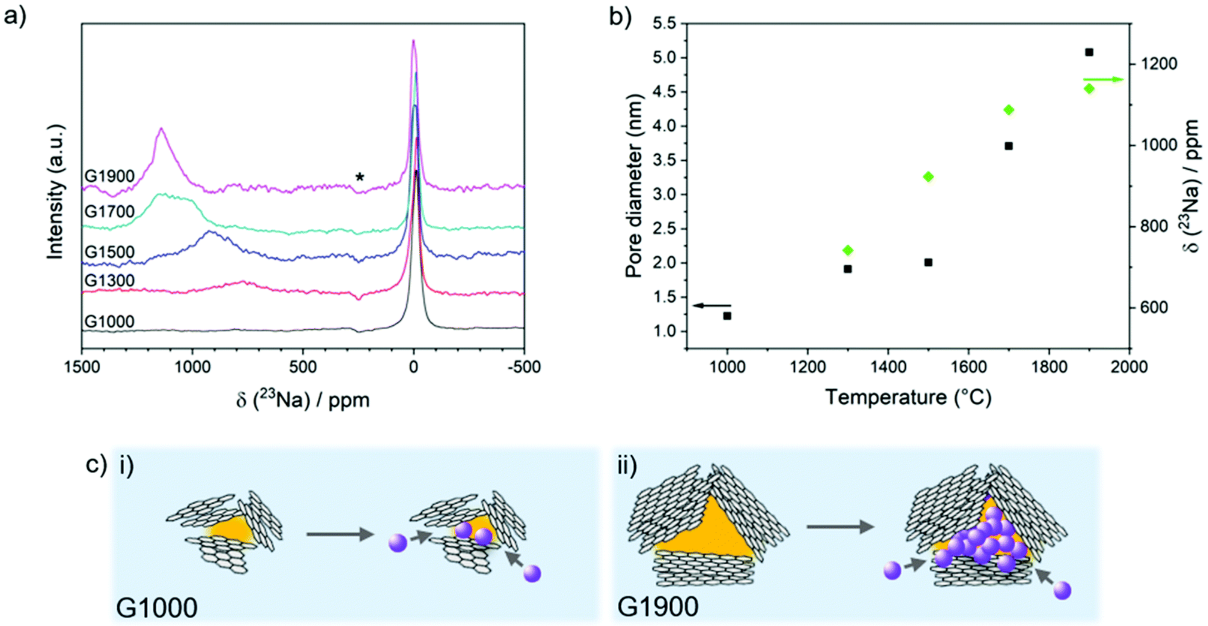

Figure 1-14 (a) Ex situ ^{23}Na MAS NMR of G1000–G1900 after discharging to 5 mV, (b) relationship between the pore diameter, quasi-metallic Na peak shift and sample pyrolysis temperature; (c) schematic illustration of pore size dependence on basal plane lateral size, in (i) G1000, where no metallic sodium is observed in the small pores, and (ii) G1900, where significant metal clustering is possible in larger pores. Reproduced with permission.[80] Copyright (2014) Royal Society of Chemistry.

Although this sodium insertion/disinsertion mechanism has been widely applieds,[54,83] Some works have shown discrepancies of the "card-house" model. Cao *et al.*[50] showed that Na intercalation into graphene sheets are occurs in the plateau region at low potentials. Moreover, Ji *et al.*[84] proposed that the slope capacity corresponded to the defect concentration in the hard carbon, supported by *ex situ* neutron pair distribution function studies and Raman information (Fig. 1-15). The PDF analysis shows that the peaks from hard carbon produced at 1100 ℃ (S-1100) diminish around ~15-17 Å, while glassy carbon and hard carbon produced at 1400 ℃ (S-1400) still show notable peak features, indicating the smallest domains in S-1100. The plot in Fig. 1-15b reveals that the S-1100 has highest capacity in the slope region and the biggest intensity ratio between D-band and G-band (I_D/I_G) in hard carbon, suggesting greatest concentration of defects. All of these discussions show that the defected carbon sites in hard carbon rather than the interlayer space are responsible for the capacity in the slope region in SIBs.

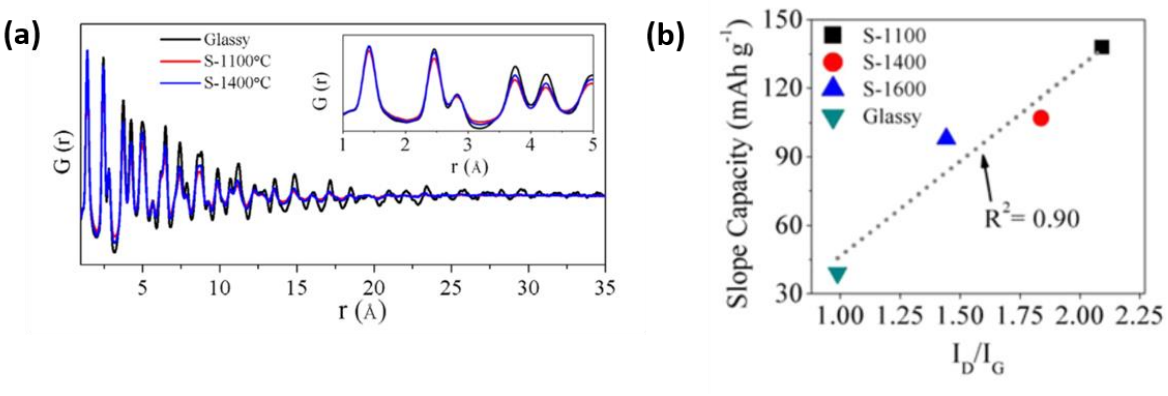

Figure 1-15 (a) PDF results for total neutron scattering, with the inset showing the short-range order. (b) Plot of the sloping capacity vs the I_D/I_G (intensity ratio of D-band and G-band) ratio from Raman spectra. Reproduced with permission[84]. Copyright (2015) American Chemical Society. S-1100, S-1400 and S-1600 represents the sucrose-derived hard carbon with different pyrolysis temperature, respectively. The glassy carbon was purchased directly from Sigma Aldrich.

In summary, the card-house model (Fig. 1-16a) indicates that the capacity from slope region corresponds to the sodium intercalation into graphene interlayers (blue marks), and the plateau storage is attributed to the sodium insertion into nanopores in hard carbon (red marks). In terms of the new proposed three parts sodium storage mechanism (Fig. 1-16b), the sodium storage in the sloping part of the reduction curve can be explained through storage at defect sites (purple marks), in contrast to the intercalation between graphene sheets. While the storage in low voltage plateau is due to the sodium intercalation between the graphene interlayers (blue marks) and the sodium adsorption on nanopores (red marks). This apparent contradiction between earlier and recent results suggests that the mechanism of sodium insertion in SIBs could overlap. Thus, further research work is needed in order to optimise the hard carbon for SIBs effectively. Here a summary of sodium storage mechanism in related to the characterization method has been shown in Table 1-2.

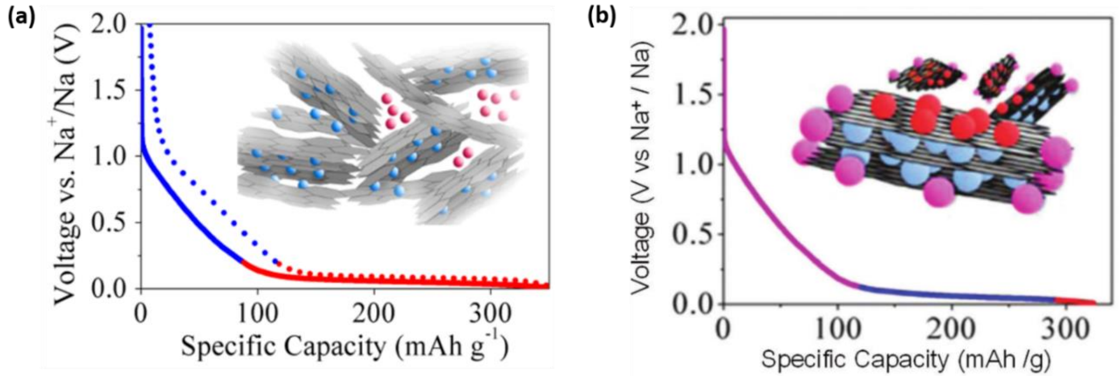

Figure 1-16 Visual representation of (a) card-house model on Na-ion storage in hard carbon, (b) sodium ion three parts storage mechanism. Reproduced with permission[84]. Copyright (2015) American Chemical Society.

Table 1-2 Capacity attribution from hard carbon with different characterization method

Slope region attribution	Plateau region attribution	Characterization method	Reference
Interlayer insertion, defects adsorption	Nanopores filling	SAXS	76
Interlayer insertion	Nanopores filling	XRD, SAXS	78
Interlayer insertion	--	Raman, DFT	53
Interlayer insertion, defects adsorption	Nanopores filling	NMR, PDF	80
--	Interlayer insertion	Theoretical simulations	50
Defects adsorption	--	PDF, Raman	84

1.3 Metal nitrides and carbides

The formation of Group 4-6 metal nitrides and carbides, which are interstitial compounds, from the structural point view, introduces the nitrogen or carbon into the lattice of the early metals. The formation of carbides occurs throughout the metals except for Pt-group metals. In addition, the nitrides and carbides of elements in Groups 7-10 are not stable with the exception of iron, cobalt, and nickel. These three elements from iron nitrides/carbides, cobalt nitrides, and nickel nitrides, respectively. Table 1-2 shows the Group 4-10 metals and the stoichiometry of their nitrides and carbides. These different stoichiometry varies from different d-band filling in the metals.[85]

Table 1-3 Typical metal nitrides (MNs) and metal carbides (MCs). Reproduced with permission[86], Copyright (2013) American Chemistry Society.

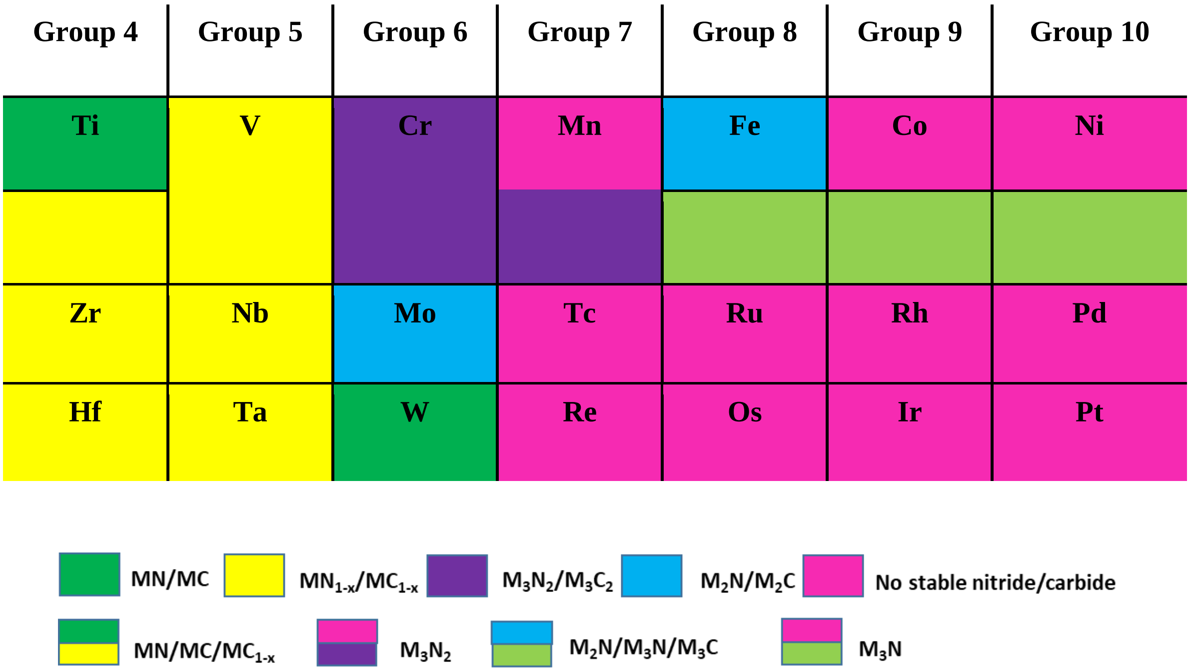

Group 4	Group 5	Group 6	Group 7	Group 8	Group 9	Group 10
Ti	**V**	**Cr**	**Mn**	**Fe**	**Co**	**Ni**
Zr	**Nb**	**Mo**	**Tc**	**Ru**	**Rh**	**Pd**
Hf	**Ta**	**W**	**Re**	**Os**	**Ir**	**Pt**

MN/MC
MN_{1-x}/MC_{1-x}
M_3N_2/M_3C_2
M_2N/M_2C
No stable nitride/carbide
$MN/MC/MC_{1-x}$
M_3N_2
$M_2N/M_3N/M_3C$
M_3N

The structural types formed by metal nitrides and metal carbides were described by empirical rules from Hägg though several complex binary carbides and nitrides such as Cr_3C_2 and ε-Ti_2N are non- Hägg phases.[87] According to Hägg, the structures of MNs and MCs are determined by the radius ratio of r_X/r_M. r_X and r_M represents the radius of interstitial and metal atom, respectively. If the radius ratio is greater than 0.59, the metals and interstitial atoms form complicated structures. If the radius ratio is less than 0.59, the metal atoms form simple common crystal structures like face centred cubic (fcc), hexagonal close-packed (hcp) or simple hexagonal structures.

The introducing of nitrogen and carbon into the interstitial sites significantly modifies the physical properties of metals in Group 4-6. The incorporation of these non-metal atoms increase the metal-metal distance and modify the metal d-band, causing a greater density of states of metal near the Fermi level, which contributes to the attractive electronic conductivity.[88,89] This electrical resistance property, together with the typical ceramic properties of high melting point, leads metal nitrides to be a promising electrode materials in energy storage and conversion.

Here we review the application of the most studied MNs and MCs in energy storage, especially in lithium ion batteries and sodium ion batteries.

1.3.1 metal nitrides/carbides (MNs and MCs) in lithium ion batteries

Many MNs have been studied as anode materials in LIBs. MNs normally undergo conversion reactions with a general mechanism ($MN + 3Li \rightarrow M + Li_3N$) in LIBs.[90] However, some different reaction processes, similar to those observed with metal oxides applied in LIBs, have also been reported. Apart from the conversion capacity of metal nitride to metal, the metal may be alloyed with Li to provide some reversible capacity.[91] Moreover, Pereira et al. reported the direct formation of LiZn without the conversion process when they applied the Zn_3N_2 in LIBs.[92] Thus the mechanism of some MNs in LIBs in still unclear and needs to be resolved.

With the conversion reaction, Balogun et al. reported Fe_2N nanoparticles with outstanding reversible capacity of 900 mA h g^{-1} at 1 A g^{-1} and a superior cycling retention of 76% after 300 cycles.[93] Moreover, Sun et al. fabricated VN thin film electrodes with a reversible capacity of 1156 mA h g^{-1} at 250 mA g^{-1}, which is close to the theoretical capacity of 1238 mA h g^{-1}.[94] However, the application of MNs in LIBs has a disadvantage of volume change during cycling, which would break the electrode and cause the capacity to decay rapidly. In order to solve the problem, researchers tried to prepare composites to buffer the volume expansion in the cycling. Dong et al. fabricated carbon microcubes to accommodate the nanostructured porous Fe_2N.[95] The presence of carbon microcubes can reduce the oxidation of Fe_2N and keep it stable, resulting a very low electrode volume expansion of 9% in long cycling process. In that case, the Fe_2N@C microcubes deliver a capacity retention of 91% after 2500 cycles at high current of 10 A g^{-1}. This strategy of introducing carbon structure and constructing composites (Ni_3N/carbon cloth, WN/carbon cloth) was also reported by other groups to obtain good capacity performance in LIBs.[96,97]

MCs have also been studied as active materials in LIBs as their good intrinsic conductivity. Most studies showed that the MCs play a role of increasing the electron transport during cycling. For example, Deng et al. reported MoC/C nanowires with capacity of 455.4 mA h g^{-1} at high current 2 A g^{-1} after 2000 cycles and a small capacity loss rate of 0.004% per cycle. The electrochemical impedance of spectra (EIS) shows that the charge transfer resistance decreases after 10 cycles, indicating the excellent capacity retention is related to the good electron transport.[98] Moreover, the morphology of MCs also affect the capacity performance in LIBs. The 2D family members of MCs, named as “MXenes”, combining metallic conductivity of metal carbides and hydrophilic nature because of the hydroxyl terminated surfaces, have been rapidly developed as active materials in LIBs in recent years after Gogotsi’s group reported them for supercapacitors in 2014.[99,100] In general, the MXenes family consists transition metal carbides, carbonitrides and nitrides, with a formula of $M_{n+1}X_nT_x$. M represents the transition metal such as Ti, V, Zr, Hf, Cr, Mo etc, and X is carbon and /or nitrogen. T_x represents the functional group (-O, -OH, -F), which is from the hydrofluoric acid (HF) or HF forming etchants when the chemical etching method is applied obtain the MXenes. Due to the superior metallic conductivity and the well-developed synthesis method, $Ti_3C_2T_x$ have been most studied and widely used MXenes in recent years.[101-103] Most recently, Zhang et al. fabricated red phosphorus/$Ti_3C_2T_x$ (PTCT) composites with two steps.[104] Firstly the $Ti_3C_2T_x$ was obtained by etching the Ti_3SiC_2 with 20% HF solution. Later the $Ti_3C_2T_x$ powder was mixed with phosphorus powder under high-energy ball milling treatment to get the final composites. Theoretical DFT calculations showed that the PTCT composites are the most stable composites among $Ti_3C_2T_x$/M (M=P, Si, and Sn), delivering an excellent cyclic performance in 1000 cycles at current of 200 mA h g^{-1}. The capacity even rises up during cycling as the volume expansion of red phosphorus increases the interlayer spacing of MXenes, leading to a reversible capacity of 585.3 mA h g^{-1} with Coulombic efficiency > 99.9% after 600 cycles.

1.3.2 The electrochemical performance of metal nitrides in SIBs

A series of MNs have been studied as anode materials in SIBs but their reaction mechanism is still not clear. Similar to use MNs in LIBs, the good theoretical capacity for conversion reactions between sodium and metal nitrides motivated researchers to apply metal nitrides in SIBs. Hector's group reported the first use of metal nitride (Ni_3N) as anode active material in SIBs.[105] A low capacity of 100 mA h g^{-1} after 30 cycles was attributed to the surface reaction of Ni_3N. The result indicates small particle size with large surface area would increase the conversion capacity. Later, they obtained Cu_3N nanoparticle with average size of 20 nm by ammonolysis of copper (II) pivalate.[106] Cu_3N delivered a stable capacity of 89 mA h g^{-1} at 39.2 mA g^{-1} over 50 cycles. *Ex situ* XRD patterns (Fig. 1-16) only showed the presence of Cu_3N and Ti substrate before cycling. Reflections of metallic copper have been observed after reduction at different potentials *vs* Na^+/Na, but did not disappear after first re-oxidation. After 50 cycles, the Cu_3N and Cu still remain the same proportion though the reflections become broader because of the crystallinity loss. The discussion suggests the conversion reaction mainly takes place on the surface of Cu_3N, and neither the reduction nor oxidation products are reversibly converted even on the surface region. Moreover, they evaluated the capacity performance of nanocrystalline Sn_3N_4 obtained by ammonolysis of $Sn(NMe_2)_4$. The nanocrystalline Sn_3N_4 shows an excellent cycling performance with 188 mA h g^{-1} at 50 mA g^{-1} and a capacity retention of 95% after 100 cycles. The studies above show that the metal nitrides can be applied in SIBs and the small particle size would be better in consideration of the surface conversion.

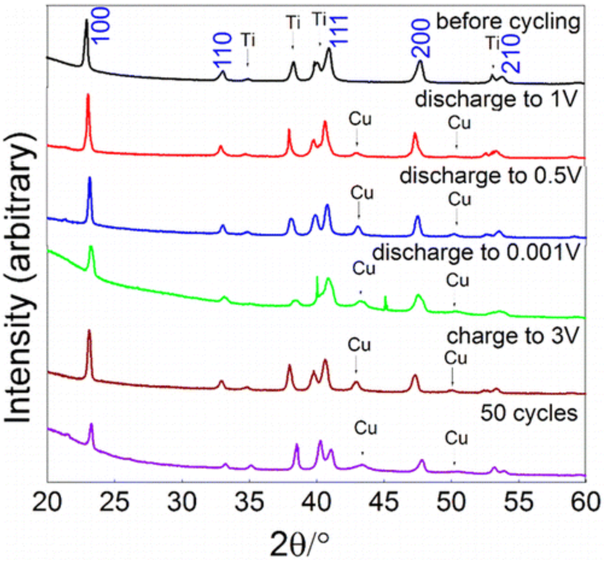

Figure 1-17 Ex-situ XRD patterns of electrodes in the different cycling stage. Reflections from the titanium current collector are labeled and the reflections due to Cu_3N are marked by Miller indices, and reflections due to copper metal produced by reduction of Cu_3N are labeled in subsequent patterns. Reproduced with permission[106], Copyright (2014) Royal Society of Chemistry.

To get more understanding about the conversion reaction of metal nitride in SIBs, Cui et al.[107] applied transmission electron microscope (TEM) and X-ray absorption near-edge structure (XANES) characterization in their study. They prepared micro-sized mesoporous vanadium nitride (VN) by ammonolyzing $Zn_3V_2O_8$ at 500 °C. The VN electrode shows a reversible capacity of 300 mA h g^{-1} at 0.1 C, and good cycling performance with capacity of 100 mA h g^{-1} at 2 C after 1000 cycles. Unlike the lithiation product (Fig. 1-17a) after discharging to 0.01 V in LIBs, the sodiation product (Fig. 1-17b) shows the presence of $VN_{0.35}$ (JCPDS 06-0624) not the metallic vanadium in SIBs, suggesting partial conversion reaction of VN. The difference of conversion products between lithiation and sodiation process have also been investigated by XANES (Fig. 1-17c). After first reduction in LIBs, the absorption edge (peak B and C) shifts to lower energy and the pre-edge peak (peak A) almost disappears, indicating the valence state of vanadium from V^{3+} to V^0. However, in the SIBs, the spectrum of discharge state shows a less shifting to lower energy and a stronger intensity of pre-edge peak compared with lithiation process, which indicates the conversion product of N-deficient $VN_{0.35}$ not the metallic vanadium forms after sodiation process. This uncompleted conversion reaction in SIBs may be related to the sluggish Na-contained mass transport at interface or weaker Na-N bonding than Li-N, although the exact reason is still not clear.

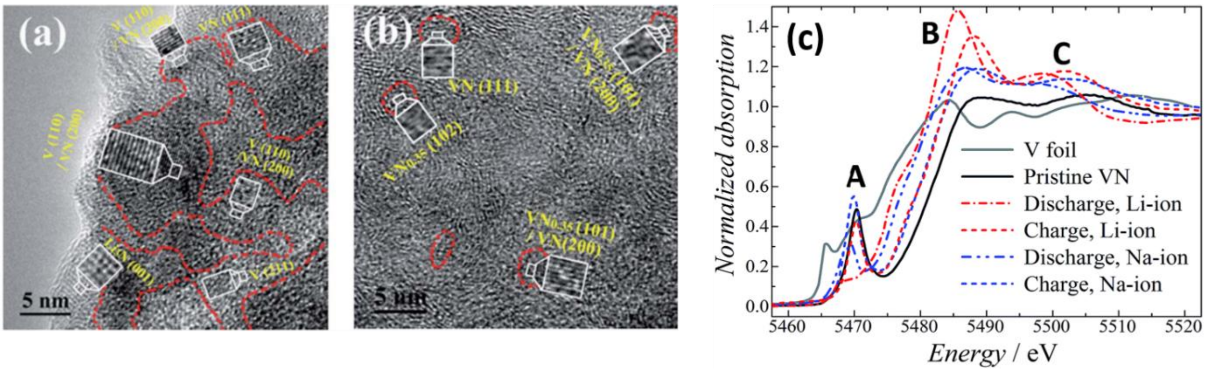

Figure 1-18 HRTEM images of (a) lithiated and (b) sodiated VN samples after discharging to 0.01 V; (c) Normalized K-edge XANES spectra of pristine VN and the samples after discharge to 0.1 V or recharge to 3 V for Li- and Na-storage. The K-edge of V foil is also measured as a reference. Reproduced with permission[107], Copyright (2015) Royal Society of Chemistry.

Although some progress has been made using conversion reaction of metal nitrides in SIBs, the reversible capacity still needs to be improved in consideration of the high theoretical capacity. On the other hand, the Gibbs free energy (Table 1-3) for most metal nitrides conversion reaction discussed above are positive, which indicate the reaction along the direction (MN+ 3Na → M + Na_3N) is thermodynamically unfavorable according to the reports from Li et al.[108] Therefore, the conversion reaction of these metal nitrides may be limited to some extent and needs further research work.

Table 1-4 A summarization of theoretical capacity, experiment capacity and the calculated Gibbs free energy of mainly reported metal nitrides in SIBs.

	Theoretical capacity (mA h g^{-1})	Experimental capacity (mA h g^{-1})	$\Delta_r G$ (kJ mol^{-1})	Reference
Ni_3N	1106	100	-	[105]
Cu_3N	392.9	89	-	[106]
Co_3N	421.4	-	42.7	-
VN	1238	300	284.8	[107]
Fe_2N	639.7	70	-	[109]
TiN	1299.5	-	337.6	-

As when applying metal nitrides in LIBs, the volume expansion caused by conversion reactions during cycling can be reduced by nanostructuring and electrochemical performance would be expected to be improved. Metal nitrides have the advantage of forming solid solutions easily. Therefore, some studies reported fabricating metal nitride based nanostructured composites, reducing the volume expansion during cycling and providing optimized electrode surface as well. Most recently, Yuan et al. prepared vanadium nitride quantum dots uniformly embedded within N-doped carbon hollow spheres (VNQS@NC HSs).[110] The VNQS@NC HSs electrode shows a reversible capacity of 360 mA h g^{-1} at 0.1 A g^{-1} after 200 cycles, much better than that of 107 mA h g^{-1} from VN-bulk nanoparticles (Fig. 1-18a). Moreover, it also delivers a reversible capacity of 306 mA h g^{-1} at 1 A g^{-1} with capacity retention of 88.8% after 1400 cycles. This work does not mention the conversion reactions (or other chemical reactions on VN) in their sodium storage process. They ascribe the excellent electrochemical performance to the hollow structure and the quantum dot size of VN, which help the electrolyte penetration and shorten the electron/ion transport path, respectively. A similar study has also been previously reported by Yang's group.[111] They fabricated VN quantum dots with 2-5 nm homogeneously dispersed onto graphene. The specific hybrid of VN-graphene ammonolyzed at 500 °C shows a reversible capacity of 254 mA h g^{-1} at 372 mA g^{-1} with capacity retention near to 100% after 800 cycles (Fig. 1-18c). EIS measurements (Fig. 1-18d) indicate that the unique microstructure of hybrid VN-graphene reduces the charge-transfer resistance, resulting the stable sodium storage. In both VN composites reported above, they deliver excellent stable cyclic performance due to the structure advantages of carbon substrates and also the small particle size of VN. Although they mention the conversion reactions between VN and sodium in their literature review, some specific characterization should be carried out to identify the exact chemical reactions during cycling.

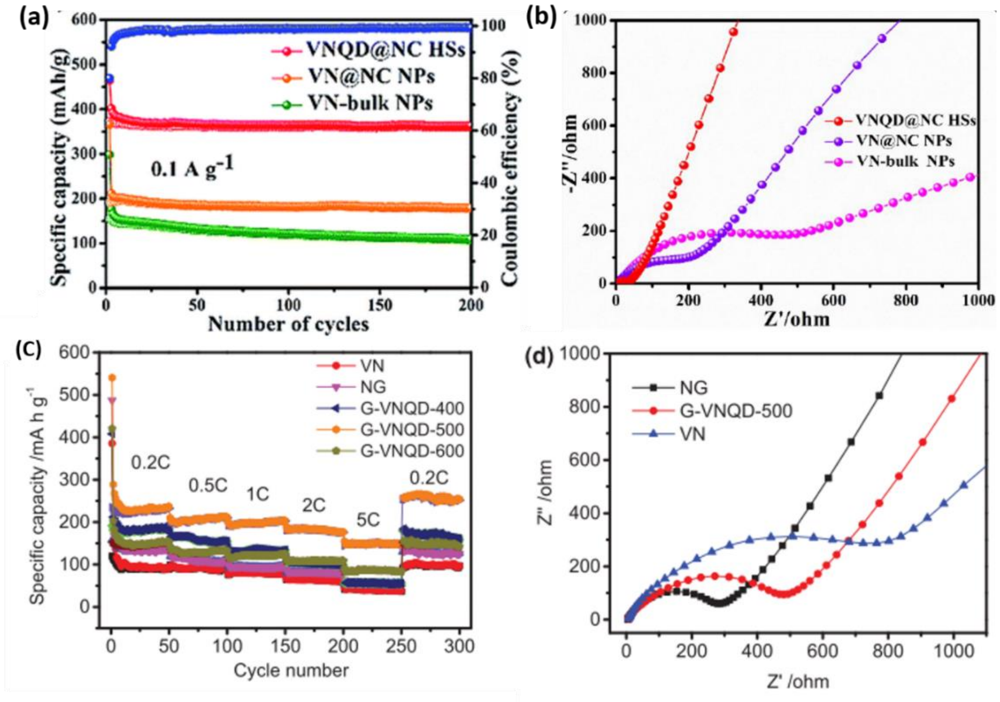

Figure 1-19 (a) Cycling performance and (b) Nyquist plots of VNQD@NC HSs, VN@NC NPs and VN-bulk NPs after 200 cycles at 0.1 A g^{-1}, Reproduced with permission[110], Copyright (2019) Royal Society of Chemistry; (c) rate capacities and (d) Nyquist plots of VN, N-doping graphene (NG), and G-VNQD-500 after rate cycles, Reproduced with permission[111], Copyright (2016) Wiley-VCH Verlag GmbH & Co. KGaA.

Li et al. fabricated a necklace-like structure composed of Fe_3N@C yolk-shell particles and applied it as anode materials in SIBs.[112] The Fe_3N@C electrode delivers a reversible capacity of 280 mA h g^{-1} at 0.4 A g^{-1} with capacity retention of 88% after 300 cycles (Fig. 1-19a). The excellent cyclic performance can be partly attributed to the unique yolk-shell structure for accommodating the volume expansion of Fe_3N during cycling (Fig. 1-19b). Cyclic voltammetry (CV) curves (Fig. 1-19c) shows two reduction peaks at 0.4 and 1.3 V, which corresponds to the initial conversion from Fe_3N to Fe and the formation of SEI film, respectively. The small peak at around 0.36 V in the anodic scan and the peak located below 0.4 V in the following cathodic scan reveal the reversible electrochemical reaction. Although the CV characterization suggests the Fe_3N maybe undergoes a conversion reaction with sodium forming Na_3N, more direct evidence with deep investigation are required in the further research. Liu et al. reported a reduction of Fe_2N to Fe_3N after sodiation process by XRD measurement.[109] In this study, they synthesized Fe_2N@C composite by hydrothermal method with the presence of FeOOH and glucose. As shown in Fig. 1-19d, the Fe_2N@C electrode shows a reversible capacity of 60 mA h g^{-1} at 500 mA h g^{-1} with capacity retention of 80% after 1000 cycles, while the Fe_2N delivers 20 mA h g^{-1} and a capacity retention of 40% after 1000 cycles. The XRD pattern (Fig. 1-19e) shows the presence of Na_3N and Fe_3N after reduction but the reflections of Fe_2N still remain, indicating part of active materials have reacted with sodium. The reflections of Fe_3N disappear after re-oxidation process (charge), suggesting the re-nitridation of Fe_3N back to Fe_2N. Overall, the discussion above shows the promising of iron nitrides based composites in the application of SIBs and indicates the possibility of conversion mechanism of iron nitrides (Fe_3N and Fe_2N) in similar with (de)lithiation mechanism in LIBs.[113,114]

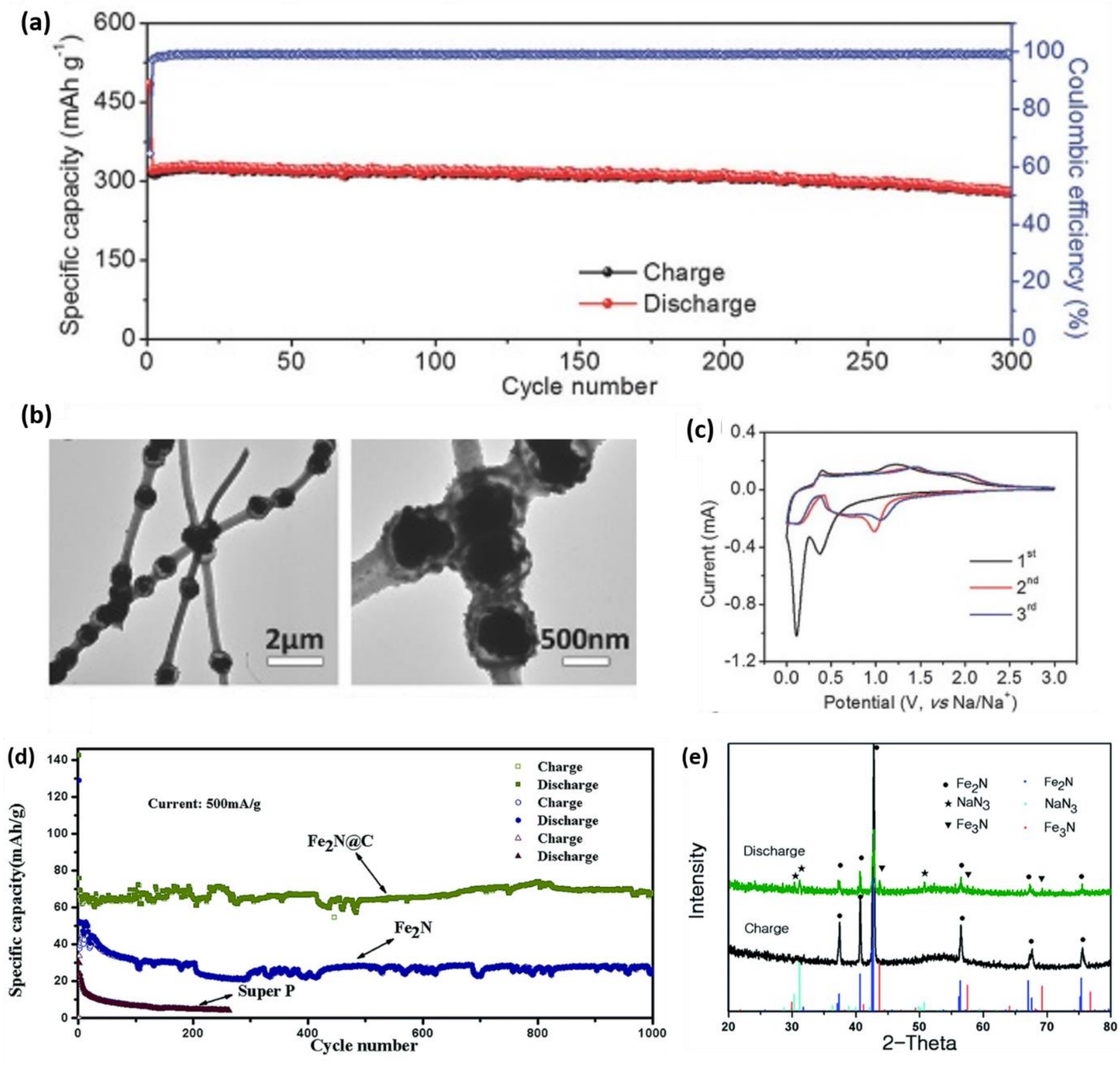

Figure 1-20 (a) cyclic performance (b) TEM images and (c) CV curves of Fe_3N@C nano-necklaces. The cycling current is 0.4 A g^{-1} and the CV scan rate is 0.2 mV s^{-1}, Reproduced with permission[112], Copyright (2018) Wiley-VCH Verlag GmbH & Co. KGaA. (d) Cycling performance of Fe_2N, Fe_2N@C and Super P electrodes at 0.5 A g^{-1}; and (e) XRD patterns of Fe_2N electrode after being charged and discharged for 10 cycles, Reproduced with permission[109], Copyright (2016) Royal Society of Chemistry.

In addition, other metal nitrides based composites (e.g. Mo_2N@C-rGO[115]) have also been synthesized and deliver good electrochemical performance in SIBs. The conversion reaction between metal nitrides and sodium provides great theoretical capacity, and the specific structures of substrate in the composites buffer the volume change from conversion reaction and facilitate the mass/ion transport during cycling. Therefore, fabrication of metal nitrides with proper structural composites are effective way to obtain anode materials in SIBs.

The most studied metal carbide in SIBs is molybdenum carbide (Mo_2C). In 2016, Çakır et al.[116] and Sun et al.[117] theoretically proved the possibility of applying Mo_2C monolayer in SIBs by first-principle simulations. Later, Lv et al. first reported the use of Mo_2C nanoplates as anode for SIBs.[118] The capacity remains 90.8 mA h g^{-1} at 200 mA g^{-1} and 58.1 mA h g^{-1} at 500 mA g^{-1} after 400 cycles, respectively (Fig. 1-20a). The CV curves (Fig. 1-20b) show a peak around 0.2 V in the cathodic scan, corresponding to sodium insertion ($Mo_2C + xNa^+ + xe^- \rightarrow Na_xMo_2C$) into Mo_2C nanoplates. This sodium storage mechanism has also been reported by Liao et al.[119] with Mo_2C based composites, in which Mo_2C nanoparticles are embedded in a porous N-doped carbon matrix (Mo_2C-NC). The pair of oxidation/reduction peak 0.74/0.28 V (Fig. 1-20d) can be attributed to the sodium insertion process discussed above. The Mo_2C-NC maintains a capacity of 98 mA h g^{-1} at 1600 mA g^{-1} with a capacity retention of 95.4% after 2500 cycles (Fig. 1-20c). This stable cyclic performance can be attributed to the nano-confined Mo_2C particles shortening ionic/electronic diffusion path and carbon matrix buffering volume change of (de)sodiation during cycling. In addition, other works (e. g. Mo_2C embedded in S-doped carbon nanofibres[120], Mo_2C/N-doped carbon nanowires[121]) also reported good electrochemical performance in SIBs.

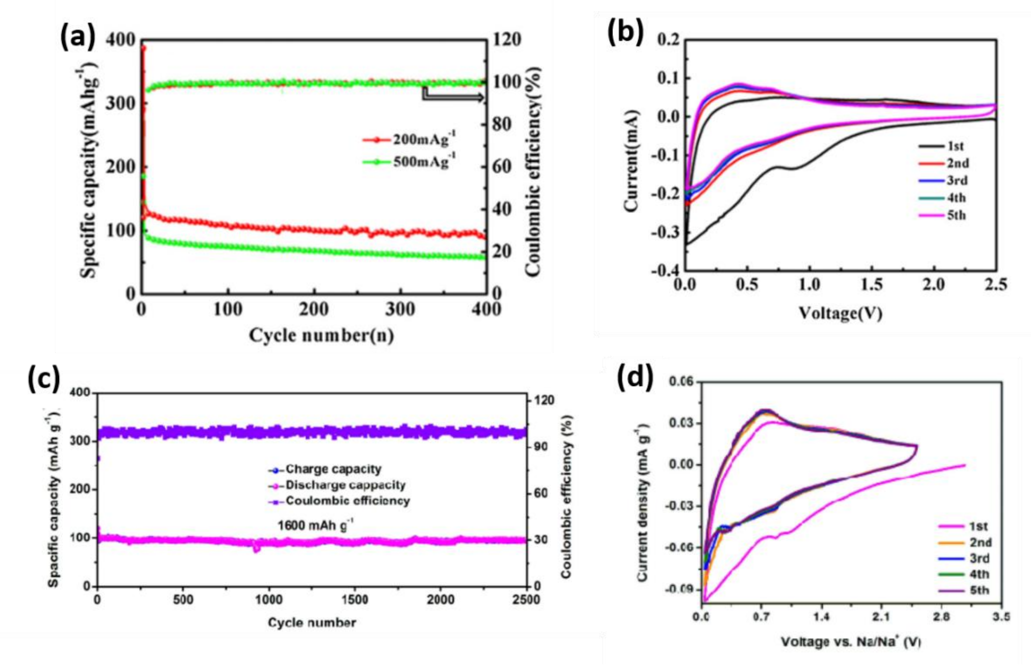

Figure 1-21 (a) Cycling performance of Mo_2C nanoplates electrode at 200 and 500 mA g^{-1}; (b) CV curves of the Mo_2C nanoplates anode for five cycles at a constant scan rate of 0.2 mV s^{-1}, Reproduced with permission[118], Copyright (2016) Elsevier. (c) Cycling performance of Mo_2C-NC at 1600 mA g^{-1}; and (d) CV curves of Mo_2C-NC at scan rate of 0.1 mV s^{-1}, Reproduced with permission[119], Copyright (2017) Wiley-VCH Verlag GmbH & Co. KGaA.

In summary, although some metal nitrides and carbides have shown a promising sodium storage recently, the study of their application in SIBs is still in early stage. More research work, including design appropriate size of metal nitride and full understanding the conversion mechanism in SIBs is necessary. Here a summary of the capacity performance and storage mechanism from some metal nitride and carbides has been shown in Table 1-4.

Table 1-5 Capacity review of metal nitrides and metal carbides in LIBs/SIBs reported in the literatures.

Materials	Applications	Performance	Synthesis method	Storage mechanism	reference
TiN	LIBs	567 mA h g^{-1} at 335 mA g^{-1}	Hydrothermal	Conversion reaction	[122]
VN	LIBs	1156 mA h g^{-1} at 250 mA g^{-1}	magnetron sputtering	Conversion reaction	[94]
Fe_2N	LIBs	900 mA h g^{-1} at 1000 mA g^{-1}	Hydrothermal	Conversion reaction	[93]
Fe_2N@C	LIBs	Capacity retention of 91% after 2500 cycles at 10 A g^{-1}	Anion conversion	Conversion reaction	[95]
Ni_3N-C	LIBs	Capacity retention of 50% after current increase from 1C to 10C	Hydrothermal	Conversion reaction	[96]
MoC/C	LIBs	Capacity retention of 92% after 2000 cycles at 2 A g^{-1}	carbothermal reduction	Short diffusion path	[98]
Ni_3N	SIBs	Reversible capacity of 220 mA h g^{-1} at 42.3 mA g^{-1}	-	Surface conversion	[105]
Cu_3N	SIBs	89 mA h g^{-1} at 39.3 mA g^{-1} after 50 cycles	Ammonolysis	Surface conversion	[106]
Sn_3N_4	SIBs	188 mA h g^{-1} at 50 mA g^{-1} after 100 cycles	Ammonolysis	Conversion and alloying	[123]

Mn_3N_2	SIBs	127 mA h g^{-1} at 50 mA g^{-1} after 50 cycles	Solvothermal	N/A	[124]
VNQS@NC HS s	SIBs	360 mA h g^{-1} at 0.1 A after 200 cycles	Solvothermal	Short diffusion path	[110]
G-VNQD	SIBs	254 mA h g^{-1} at 372 mA g^{-1} after 800 cycles	Hydrothermal	N/A	[111]
Fe_3N@C	SIBs	280 mA h g^{-1} at 0.4 A g^{-1} after300 cycles	Electrospum method, carbothermal reduction	Short diffusion path	[112]
Fe_2N@C	SIBs	60 mA h g^{-1} at 0.5 A g^{-1} after 1000 cycles	Hydrothermal	Conversion reaction	[109]
Mo_2N@C-rGO	SIBs	487.2 mA h g^{-1} at 0.2 A g^{-1} after 100 cycles	Microwave irradiation	Conversion reaction	[115]
Mo_2C	SIBs	90.8 mA h g^{-1} at 200 mA g^{-1} after 400 cycles	Carbothermal reduction	Short diffusion path	[118]
Mo_2C-NC	SIBs	98 mA h g^{-1} at 1600 mA g^{-1} after 2500 cycles	Carbothermal reduction	Alloying	[119]
Mo_2C-SC	SIBs	223.4 mA h g^{-1} at 0.1 A after 50 cycles	Carbothermal reduction	Conversion reaction	[120]
Mo_2C-NC	SIBs	166 mA h g^{-1} at 200 mA g^{-1} after 100 cycles	Carbothermal reduction	N/A	[121]

2. Experimental and characterization

2.1 Materials characterization

2.1.1 X-ray diffraction (XRD)

XRD is a powerful non-destructive technique for characterizing the chemical compositions and crystal structure of crystalline materials. Generally, a monochromatic beam of X-ray, normally using Cu K_α radiation with wavelength of 0.15406 nm, interacts with the electrons of the atoms in the crystal. As shown in the Fig. 2-1, the diffractions can be visualized as reflections from a set of parallel planes in the crystal if we use the Bragg's model. With Bragg's law, the X-ray path difference (ABC) on reaching the different crystal lattice plane can be measured by equation 2-1,

$$n\lambda = 2d_{hkl}\sin\theta \qquad \text{Equation 2-1}$$

Here the n is the order of the reflection and λ is the wavelength of X-ray source. The θ is the Bragg angle, and the d_{hkl} is the interplanar spacing in the crystal.

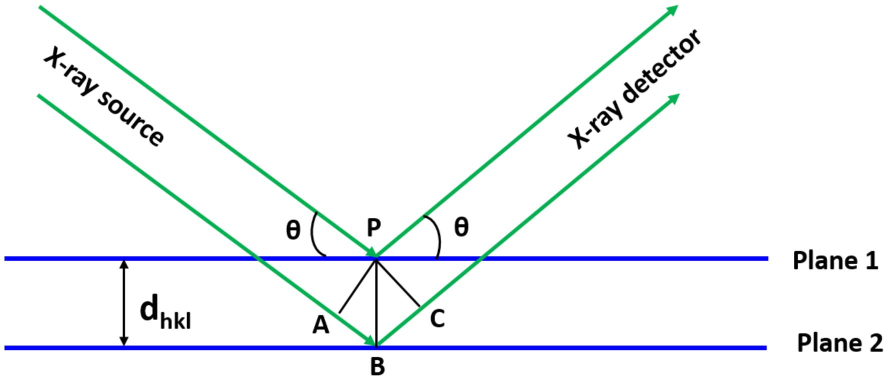

Figure 2-1 Schematic illustration of Bragg's model.

In this study, XRD patterns were collected with parallel Cu-K_α X-rays using a Rigaku Smartlab. For the powder sample, it was filled in a silica capillary with diameter of 0.6 or 0.7 mm. For the *ex-situ* XRD measurement, the cells were disassembled in the N_2-filled glove-box and then the working electrode was transferred into a sealed box. The electrode seated in the sealed box was measured with grazing incidence XRD.

The diffraction measurement converted the linear information (d-space of crystal planes) to angular information (Bragg angle). A XRD pattern is a fingerprint of the phase which can be compared with known phase stored in the database (e.g. inorganic crystal structure database (ICSD)). The data analysis used the Rigaku PDXL2 and general structure analysis suite (GSAS) packages.[125] The typical procedure for the refinement involves five parts:

Using ICSD database to determine an approximate model of the structure;

Refinement of the lattice parameters and zero point;

Refinement of the atom positions;

Refinement of the isotropic thermal parameters;

Refinement of peak shapes parameters.

The goodness of fitting can be observed from the plot of the profile fit. The difference between observed and calculated pattern should be as flat as possible. The $R_{weighted\ profile}$ (R_{wp}) is an important factor to describe the goodness of fitting and should be as small as possible for a good fit. With the Rietveld method, the physical parameters such as lattice parameters and particle size can be checked by the data refinement.

Compared the lattice parameters from the refinement results and database, the exact components (i.e., TiN, TiO and TiC) in the samples can be identified. Interlayer distance (d_{002}) in the hard carbon was obtained to discuss the relationship between interlayer distance and sodiation capacity. The particle size of metal nitrides/carbides was measured as well.

2.1.2 Raman spectroscopy

Raman spectroscopy is a non-destructive technique to observe the vibration, rotation and other low frequency models. It provides a fingerprint by which molecules can be identified. Generally, a monochromatic laser is incident upon a sample and the radiation interacts with the chemical bonds within the material. It gives reflection, absorption and scattering in some manner. Most of the scattered light are elastic scattering (Rayleigh scattering, $\lambda_{Rayleigh}=\lambda_{laser}$) and a small portion of light are inelastic scattering ($\lambda_{scatter}>\lambda_{laser}$) which is called Raman scattering providing the structure information (Fig. 2-2).

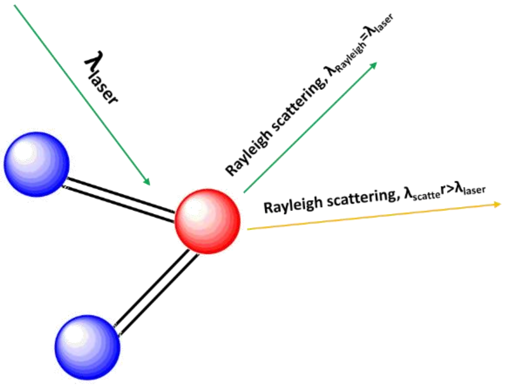

Figure 2-2 Schematic illustration of Raman scattering.

A Raman spectrum features the peak intensity and Raman shifts measured with the laser line as the reference. The Raman shift represents the vibration energies in relation to the highly polarizable bonds in the molecules. In this study, the powder were simply located on the glass slide and the Raman spectra were collected with a Renishaw inVia Ramascope operating at 785 nm. Raman peak analysis used WiRE software, a linear baseline correction and curve-fitting using Gaussian and Lorentzian functions. Fig. 2-3 shows the typical curve fitting of carbon material with three different peaks. The carbon was obtained by pyrolysis of cotton wool at 1400 °C with argon gas. D band with Raman shift around 1310 cm^{-1} is corresponding to disordered graphitic lattice vibration and G band with Raman shift around 1580 cm^{-1} can be ascribed to graphitic lattice vibration. While D_3 band is related to amorphous carbon vibration model with Raman shift of 1500 cm^{-1}.[126]

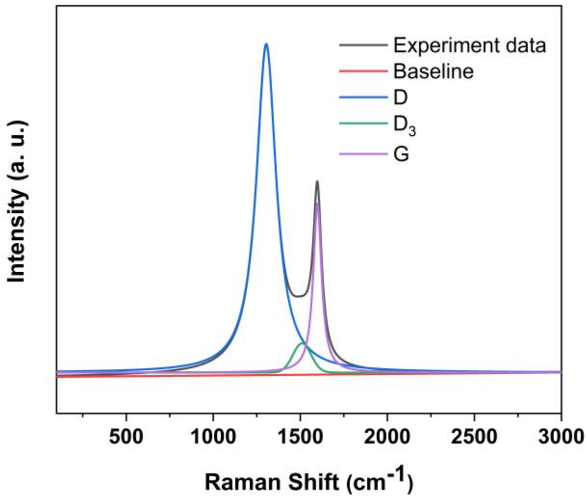

Figure 2-3 Typical curve fitting of hard carbon obtain from cotton wool.

2.1.3 Thermogravimetric analysis (TGA)

Thermogravimetric is a method to measure the weight of substance with a function of temperature. It records the mass change (gain or loss) when the sample subjected to thermal process including oxidation, decomposition and reduction at controllable gas conditions. In this study, TGA was measured with a TG 209 F1 Libra with a ramp rate of 10 °C min^{-1} with flowing gas mixture of Ar (50 ml min^{-1}) and O_2 (20 ml min^{-1}). Normally, thermogravimetric (TG) curves are plotted with mass change in percentage on y-axis and temperature on the x-axis. Fig. 2-4 shows the typical TG curves of carbon and vanadium nitride composite. The composite at heating condition undergoes the oxidation of carbon and vanadium nitride. The mass loss between 325 and 500 °C combined mass loss due to burning carbon and mass increase due to oxidizing vanadium nitride. After heating to 600 °C, the carbon transfers to carbon dioxide and evaporates with gas flow. The final plateau corresponds to the vanadium oxides and can be identified by XRD characterization. In that case, the mass ratio of vanadium nitride in the composite can be measured by the TGA analysis.

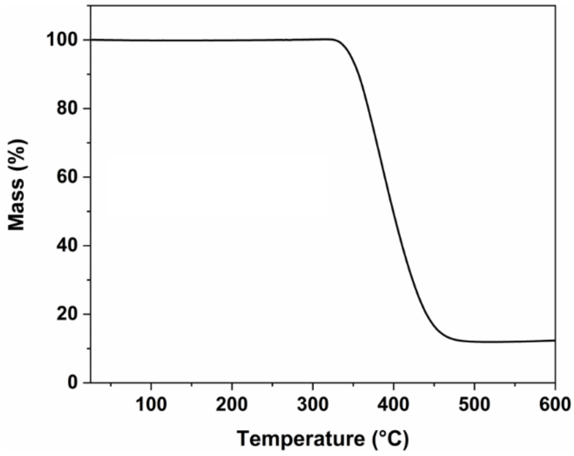

Figure 2-4 Thermogravimetric curves of heating vanadium nitride-carbon materials at Ar/O_2 gas.

2.1.4 Scanning electron microscopy (SEM), transmission electron microscopy (TEM) and electron dispersive X-ray (EDX) spectroscopy

Electron microscopy uses a beam of energetic electrons to observe objects on a fine scale. Scanning electron microscopy (SEM) is a type of electron microscopy that scans a high-energy electron beam across the surface of sample, providing detailed information about the surface topography (e. g. surface features and texture), morphology (shape and size). Transmission electron microscopy (TEM) is related technique that uses high-energy electron beam that is transmitted through the specimen, giving the information on morphology and composition. In this study, SEM used a Philips XL30 with 10 kV accelerating voltage and a Jeol JSM6500 with 15 kV accelerating voltage. TEM was carried out with a FEI Tecnai T12 at 80 kV. For the sample preparation, the powder attached upon conductive black tape was hold on a sample stage.

Electron dispersive X-ray (EDX) spectroscopy is used to find the chemical composition of materials and create an element composition mapping within a raster area. Generally, the incident beam excites an electron in an inner shell, ejecting it and creating an electron hole (Fig. 2-5a). An electron in a higher energy shell then fills the hole and the energy difference released as an X-ray photon (Fig. 2-5b). The number and energy of the X-ray photons emitted from the specimen can be measured by an energy dispersive detector. The energy of X-ray is related to the atomic structure of elements from the specimen. Therefore, the element composition of materials can be obtained by EDX analysis.

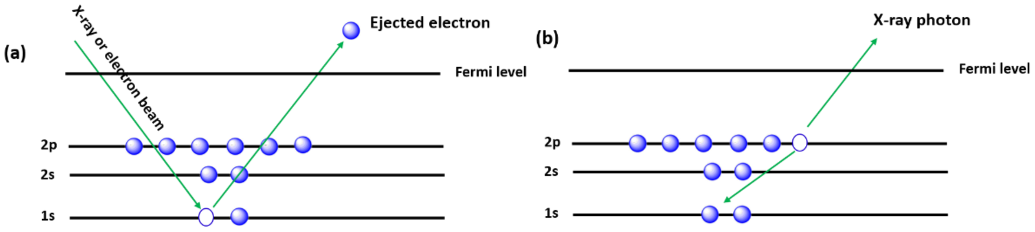

Figure 2-5 illustration of EDX process.

Elemental mapping was obtained by EDS analysis with Thermofisher Ultradry detector in this work. Different X-ray intensity indicates the difference of element concentration across the surface. One or more maps are recorded using image brightness intensity as a function of element concentration.

2.1.5 X-ray photoelectron spectroscopy (XPS)

X-ray photoelectron spectroscopy (XPS) is a surface sensitive spectroscopic technique to measure the chemical composition on the surface. Generally, a monoenergetic X-ray (Mg K_α or Al K_α) beam strikes the core electron of the atoms and creates an electron vacancy, releasing a photoelectron with specific binding energy (Fig. 2-6a). Later, the electron at higher energy level fills the vacancy and emits Auger electron with specific binding energy (Fig. 2-6b). The XPS instrument detects the binding energy from both photoelectrons and Auger electrons. Each element releases unique electrons with specific binding energies, which can be used to quantify the element composition. In addition, XPS analysis also gives information about the chemical state of compound (e.g. C-O and O-C-O) as the binding energy depends on the chemical environment.[127]

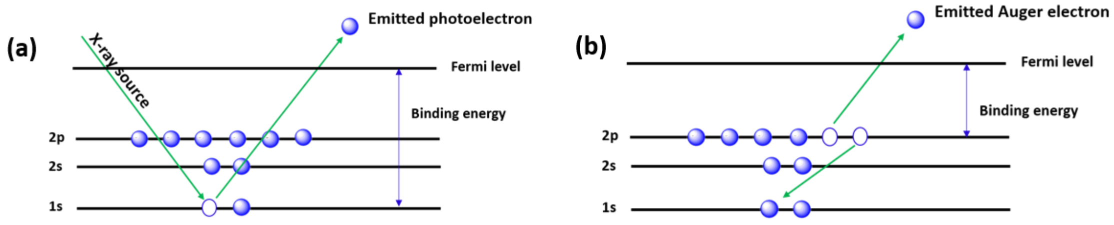

Figure 2-6 illustration of (a) photoelectron and (b) Auger electron emission during XPS measurement.

XPS is a surface sensitive technique because only the electrons generated near the surface escape and can be detected. The photoelectrons have relatively low kinetic energy. Due to the inelastic collisions within atomic structure in the solid, photoelectrons releasing more than 2 nanometers below the surface cannot escape with enough energy and lose its information. Thus the information depth is around two nanometers in XPS and give the surface sensitivity.

In this study, XPS was carried on a Thermo Nexsa with Al K_α X-rays. For sample preparation, powder was directly put on the golden stage and transferred to chamber. For *ex-situ* XPS measurement, cells were disassembled in the N_2-filled glove-box and then the electrode of interest was transferred into a working stage to be detected. Ar^+ sputtering was carried out with an etching rate of 2 nm min^{-1} in the XPS depth profiling. XPS data analysis was conducted from the Casa XPS software package. The XPS binding energy scale was calibrated to graphitic carbon at 284.6 eV. Core peaks were fitted with nonlinear Shirley-type background.[128] Peak positions and areas were optimized by a weighted least-squares fitting method using 70% Gaussian and 30% Lorentzian line shapes.

2.1.5 N_2 physisorption analysis

N_2 adsorption measurements were used to determine the surface area and pore size distribution of solid materials. Generally, the amount of N_2 physically adsorbed on the surface of solid increases with applied pressure. The adsorption isotherms feature the adsorbed volume of N_2 as a function of relative pressure.

According to the International Union of Pure and Applied Chemistry (IUPAC), the isotherms can be classified into six types (Fig. 2-7a).[129] Reversible type I isotherms describe microporous solids with small external surface area such as molecular sieve zeolites. Type II, III and VI isotherms are obtained from nonporous or macroporous materials. Type IV and V isotherms are characteristic of mesoporous adsorbents. Hysteresis loops in type IV and V isotherms corresponding to texture (pore size distribution or pore geometry) can be divided into four types (Fig. 2-7b). Type H1 loop is often found in materials with narrow range of uniform mesoporous or well defined cylindrical-like pore channels. Type H2 is found in disordered materials with variable pore size distribution and pore structure. Type H3 is ascribed to materials with slit-shaped pores. The H4 loop is similar to H3 without obvious increased adsorption at high relative pressure, which is often found in mesoporous zeolites and micro-mesoporous carbons.

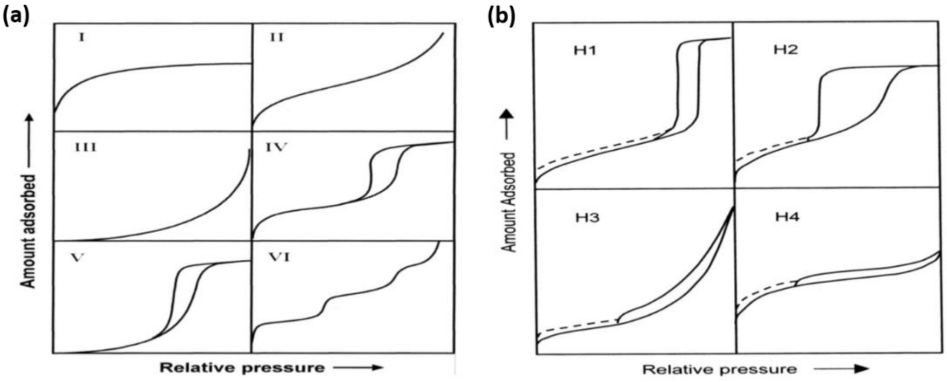

Figure 2-7 Classification of (a) physisorption isotherms and (b) hysteresis loops according to IUPAC.[129]

The Brunauer-Emmett-Teller (BET) method is the most widely used procedure for calculating the surface area. The BET concept is an extension from Langmuir theory, which is used to describe the adsorption of monolayer molecular or atom, to multilayer adsorption with three hypotheses. The first one is that gas molecules physically adsorb on the solid in layers. The second one is that no reaction occurs between each adsorption layer. The last one is that Langmuir theory can be applied in each layer. The BET equation can be expressed as equation 2-2:

$$\frac{1}{v[\left(\frac{p_o}{p}\right)-1]} = \frac{c-1}{cv_m}\left(\frac{p}{p_o}\right) + \frac{1}{cv_m} \qquad \text{Equation 2-2}$$

Where v is adsorbed gas quantity, p_o and p is saturation and equilibrium pressure of the adsorbate, v_m is the monolayer adsorbed gas quantity, and c is the BET constant.

The BET equation can be plotted as linear graph and used to calculate the value of v_m. Then the BET surface area can be measured by equation 2-3:

$$S_{BET} = \frac{v_m Ns}{aV} \qquad \text{Equation 2-3}$$

Where S_{BET} is specific surface area, v_m is the monolayer adsorbed gas quantity, N is Avogadro’s number, s is the cross-sectional area of adsorbed gas and V is the molar volume of adsorbed gas.

Nonlocal density functional theory (NLDFT) is one of the most used methods to measure the pore size distribution (PSD). The PSD is obtained from adsorption isotherms and calculated with the adsorption integral equation:

$$N(p/p_o) = \int_{w_{min}}^{w_{max}} f(w) K(p/p_o, w) dw \qquad \text{Equation 2-4}$$

Where $N(p/p_o)$ is the experimental adsorption isotherms as a function of pressure p/p_o; w is the pore width; w_{min} and w_{max} are the widths of smallest and largest pores present; f(w) is the PSD to be calculated; $K(p/p_o, w)$, which is called the kernel function of integral equation, represents the theoretical isotherms as a function of p/p_o and w.

In this study, the nitrogen adsorption/desorption isotherms was obtained on a Micromeritics Tristar II surface area analyzer. All the samples were dried in the 120 °C for overnight before the measurement. BET surface area and pore size distribution were calculated by the equations discussed above.

2.2 Electrochemistry performance

2.2.1 Cell assembly

Working electrodes were prepared from inks produced using 0.2 g of composite or hard carbon with a polyvinylidene difluoride (Solvay) binder at a weight ratio of 95:5 %wt. These materials were mixed with N-methyl-2-pyrrolidone (0.5-0.6 mL, anhydrous, 99.5%, Sigma-Aldrich) to prepare a viscous ink, which was mixed with an homogenizer (running at speed of 10000, 15000 and 20000 revolutions per minute for 5, 3 and 2 min, respectively) and cast onto copper foil (0.0175 mm thick, Goodfellow Cambridge Ltd) using a K-bar of 40 or 200 μm. The ink was air dried before the foil was cut into 11 mm diameter discs, and then further dried under vacuum for overnight. Typical mass loadings of electrodes prepared in this way were 1-1.5 mg cm^{-2} or 2-2.5 mg cm^{-2}. 11 mm diameter discs of sodium (Sigma-Aldrich) were used as the counter and reference electrode. Two sheets of dried Whatman GF/D glass fiber (GE Healthcare Life Sciences) were used as the separator, soaked with 180 μL of the electrolyte which was made up from 1 M $NaClO_4$ (Alfa Aesar, anhydrous) in a mixture of ethylene carbonate (EC, Sigma-Aldrich, anhydrous, 99%) and diethyl carbonate (DEC, Sigma-Aldrich, anhydrous, ≥ 99%) in a 1:1 ratio in volume. All the electrochemical tests were conducted using Swagelok cells (Fig. 2-8) and all the cell assembly was carried in an argon-filled glove box (Mbraun, $H_20 < 0.1$ ppm, $O_2 < 0.1$ ppm).

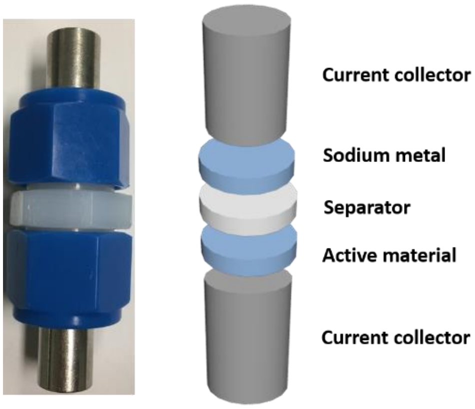

Figure 2-8 components in Swagelok cell.

2.2.2 Galvanostatic Cycling with Potential Limitation (GCPL)

Galvanostatic cycling with potential limitation is the most standard protocol to calculate the capacity performance of batteries being cycled at a constant current and a potential range. The current in cycled battery is often referenced to as C-rate. A C-rate of 1 C means that necessary current is incorporated the theoretical capacity into the battery in one hour. The theoretical specific capacity (Q) is calculated by:

$$Q = \frac{nF}{3600M} \qquad \text{Equation 2-5}$$

Where n is number of transferred electrons, F is the Faraday's constant, and M is the molar mass of active material. The real specific capacity is calculated by:

$$Q = \frac{It}{m} \text{ or } Q = \frac{It}{V} \qquad \text{Equation 2-6}$$

Where the I is the constant current, t is the applied time, m and V is the mass and volume of active material, respectively.

In this study, galvanostatic charge/discharge cycling was performed at 25 °C in the voltage range 5 mV to 2 V (vs. Na^+/Na) using a Biologic MPG potentiostat.

2.2.3 Differential capacity analysis

Differential capacity (DC) describes the capacity change during charge or discharge as a function of voltage. Differential capacity analysis plots the differential capacity (dQ/dE) vs. E, which gives structural transformation during charge/discharge process. The advantage of the DC plot is that the plateau information in the E vs. Q plot is clearly seen in the dQ/dE vs. E plot. The presence of cathodic and anodic peaks are related to the electrochemical reactions on electrode materials. The plot of dQ/dE vs. cycle numbers gives the information of capacity degradation during long cycles.

2.2.4 Electrochemical impedance spectroscopy (EIS)

Electrical impedance (Z) is the measure of opposition that the circuit gives to a current when a voltage is applied. The measurement of alternating current (AC) impedance uses small amplitude perturbation method to reveal the electrochemical process in the electrode. Voltage and current are represented as functions of angular frequency (ω) and time.

$$Z = \frac{V(\omega,t)}{I(\omega,t)} \qquad \text{Equation 2-7}$$

Where ω=2πf, and f is the frequency.

Different electrode processes can be modelled with different equivalent circuits. The Randles equivalent circuit (Fig. 2-9a) applies to simple reversible electron transfer at the liquid electrolyte/electrode interface. Here the R_u represents the uncompensated solution resistance, R_{ct} is charger transfer resistance, Z_w is Warburg impedance, and C_{dl} is double layer capacitance.

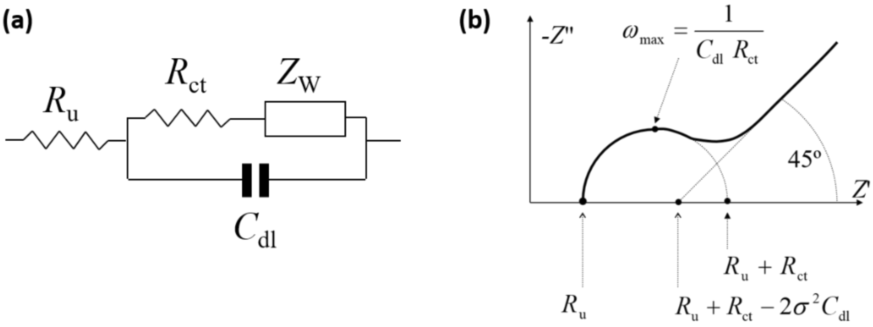

Figure 2-9 illustration of (a) Randles equivalent circuit and (b) Nyquist plot of Randles circuit.

Nyquist plot (Fig. 2-9b) is a best way to analyze the impedance data obtained from Randles equivalent circuit. In that case, we can get the charge transfer resistance and mass transfer information from the Nyquist plot. In this study, the EIS analysis was measured by using Biologic MPG potentiostat at room temperature with a frequency range from 0.05 Hz to 500 kHz.

3. Synthesis of hard carbon from cotton wool and resorcinol-formaldehyde gels

3.1 Introduction

Hard carbon shows attractive sodium storage performance including a considerable reversible capacity (200-300 mA h g^{-1}) and a plateau region at low potential (cal. 0.2 V *vs* Na^+/Na).[130] Researchers have reported that phenolic resin-derived hard carbon shows good electrochemical features due to the controllable carbon physical and chemical properties.[42] Cotton wool is another promising precursor because of its low cost and abundant supply. In this work, resorcinol-formaldehyde and cotton wool derived hard carbon have been produced at high pyrolysis temperature. Physical properties and electrochemical performance of these hard carbons have been investigated to identify which material is better to use in the productional composite materials.

3.2 Experimental

Cotton wool was directly carbonized in a closed end alumina furnace tube at 1000, 1200 or 1400 °C with a ramp of 4 °C and the maximum temperature maintained for 2h under argon gas, respectively. Hard carbons obtained with different temperatures were denoted as HC-CW-T, and the T represents the pyrolysis temperature. The gas flow rate was 200, 600 or 1000 mL min^{-1}.

Resorcinol formaldehyde based hard carbon was synthesized based on a previous report[42]. Briefly, 2.20 g of resorcinol (Sigma Aldrich, ≥ 99.0%) was dissolved in a mixture of 4.0 mL of 10 mM HCl (Alfa Aesar, 36.5-38%) and 0.8 mL of ethanol (Alfa Aesar, anhydrous). After obtaining a homogeneous solution, the solution was cooled in an ice-water bath, followed by the addition of 3.0 mL formaldehyde solution (Alfa Aesar, 37 *wt*% in H_2O, contains 10-15% methanol as stabilizer) with vigorous stirring. After mixing for 5 min, the solution was kept at 80 °C for 24 h for gelation. Then the gel was washed with ethanol 3 times and dried. Finally, the gels were carbonized at different temperatures (1000, 1200 or 1400 °C) for 2 h in a closed end alumina furnace tube under argon gas. Hard carbons obtained with different temperatures were denoted as HC-RF-T, and the T represents the pyrolysis temperature.

3.3 Results and discussions

The main component (~95%) in cotton wool is cellulose $(C_6H_{10}O_5)_n$,[131] which is a polymer of β-D-glucose, containing plentiful intra- and inter-molecular hydrogen bond networks. The cellulose decomposes to carbon with release of water at high temperature (Scheme 3-1). During the decomposition process, the intermediate products like carbon monoxide and organic by-products will also be produced. The formation of resorcinol-formaldehyde resin (Scheme 3-2) contains a complex reaction process before firing with argon gas to get the black color of hard carbon. At ambient acid synthesis condition, the formaldehyde accepts hydrogen proton and leaves an empty orbital. Then the empty orbital can accept electrons near to the –OH group, which are more active because of the polar effect from the oxygen. Later the repeated processes continue and orange color resorcinol-formaldehyde resins are obtained.

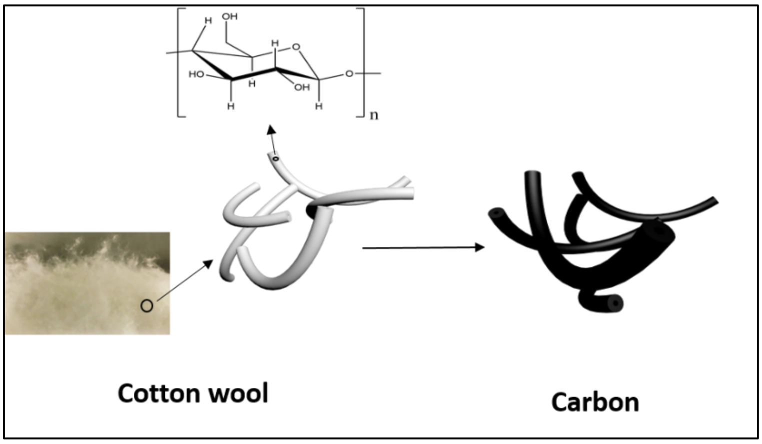

Scheme 3-1. Illustration of synthesis process of cotton wool derived hard carbon

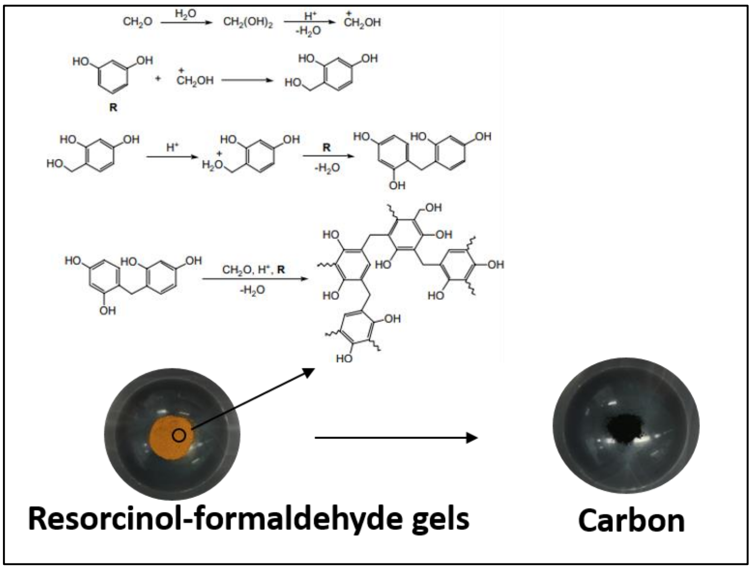

Scheme 3-2. Illustration of synthesis process of resorcinol-formaldehyde gels derived hard carbon

3.3.1 Temperature effect on synthesis of hard carbon

Fig. 3-1 and Fig. 3-2 show the structural information and morphological characterization of carbon obtained with Ar gas flow rate of 200 mL min^{-1}. XRD patterns of the carbon materials with different pyrolysis temperature display two broad peaks around 23° and 44°, corresponding to the 002 and 100 peaks of the graphitic regions of the hard carbon, respectively. Raman spectra display two broad peaks of D-band (defect-induced band) and G-band (crystalline graphite band) around 1343 cm^{-1} and 1589 cm^{-1}, respectively.[42] Intensity ratio (I_D/I_G) of hard carbon obtained from cotton wool stays almost the same (2.11 to 2.17) as pyrolysis temperature goes up from 1000 to 1400 °C, while the intensity ratio of hard carbon obtained from resorcinol-formaldehyde gels goes up from 1.71 to 2.08 with increased pyrolysis temperature, suggesting the decrease of graphitization degree in hard carbon. Although the negative correlation results are abnormal to general expectations,[42,132] some other researches also reported this trend in intensity ratio. [47,69] SEM image indicates the cotton wool derived hard carbon has a fibrous structure with diameter 5-10 μm while the resorcinol-formaldehyde derived hard carbon has a powdery morphology.

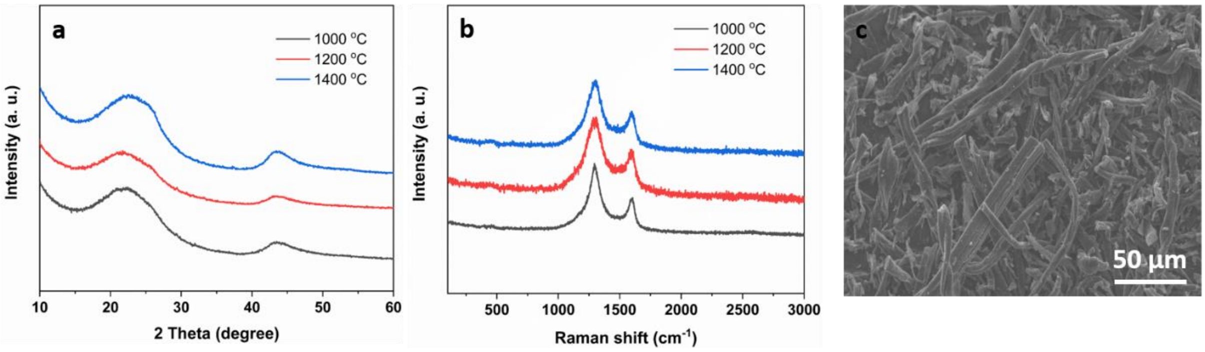

Figure 3-1 (a) XRD, (b) Raman and (c) SEM spectra of hard carbon obtained from heating cotton wool at different temperature with Ar gas flow rate of 200 mL min^{-1}.

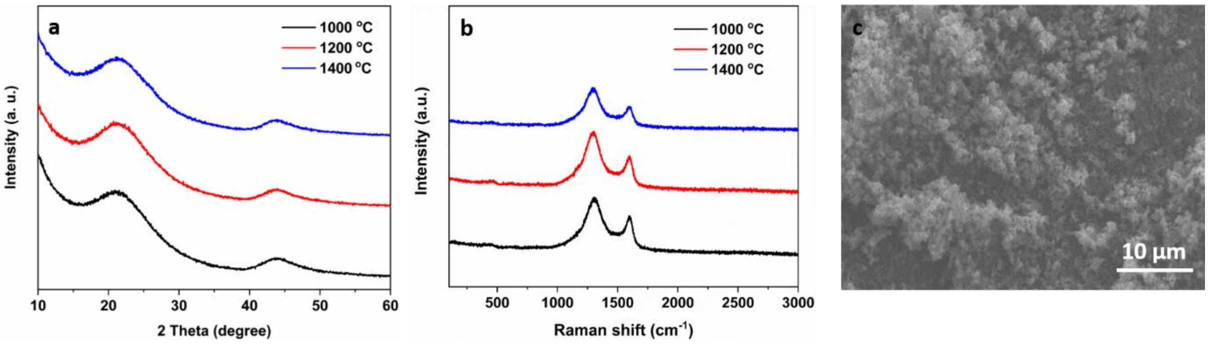

Figure 3-2 (a) XRD, (b) Raman and (c) SEM spectra of hard carbon obtained from heating resorcinol-formaldehyde gels at different temperature with Ar gas flow rate of 200 mL min^{-1}.

BET surface area and pore size distributions were investigated. N_2 adsorption-desorption isotherms (Fig. 3-3 a) can be classified as type IV and H4 type hysteresis according to the IUPAC classification[133], showing that the co-existence of micropores and mesopores in the cotton wool derived hard carbon. A feature common to these hysteresis loops is that complete closure points should appear at nitrogen's boiling point around $P/P_0 = 0.42$. However, for some materials containing micropores, low pressure hysteresis can be extended to the lowest attainable pressures as seen in these isotherms.[133-135] Fig. 3-4 shows the Isotherms have a type IV and H4 type hysteresis when the pyrolysis temperature is below 1200 °C. Compared with pore size structure obtained from cotton wool, resorcinol-formaldehyde derived hard carbon presents higher proportion of micropores, and shows a typical feature of type I when the pyrolysis temperature goes up to 1400 °C. Pore size distribution (Fig. 3-3 b and Fig 3-4 b) obtained by density functional theory (DFT) indicates the presence of micro and mesopores. Pore size evolution may be ascribed to the collapse of mesostructure and the shrinkage by condensation when the pyrolysis temperature goes up to 1400 °C.[136] BET surface area (Table 3-1) decreases with increasing of pyrolysis temperature by reducing functional groups, which is consistent with previous reports[69]. The product yield decreases at higher temperature, which may be attributed to the removing of more hydroxyl groups on the hard carbon.

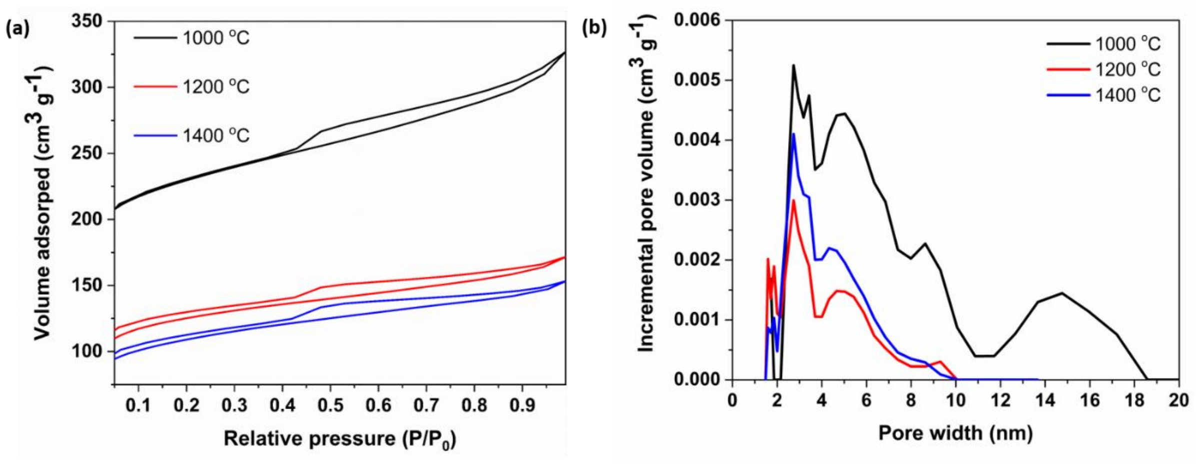

Figure 3-3 (a) N_2 adsorption-desorption isothermal curves and (b) pore size distribution of hard carbon obtained from heating cotton wool at different temperature with Ar gas flow rate of 200 mL min^{-1}.

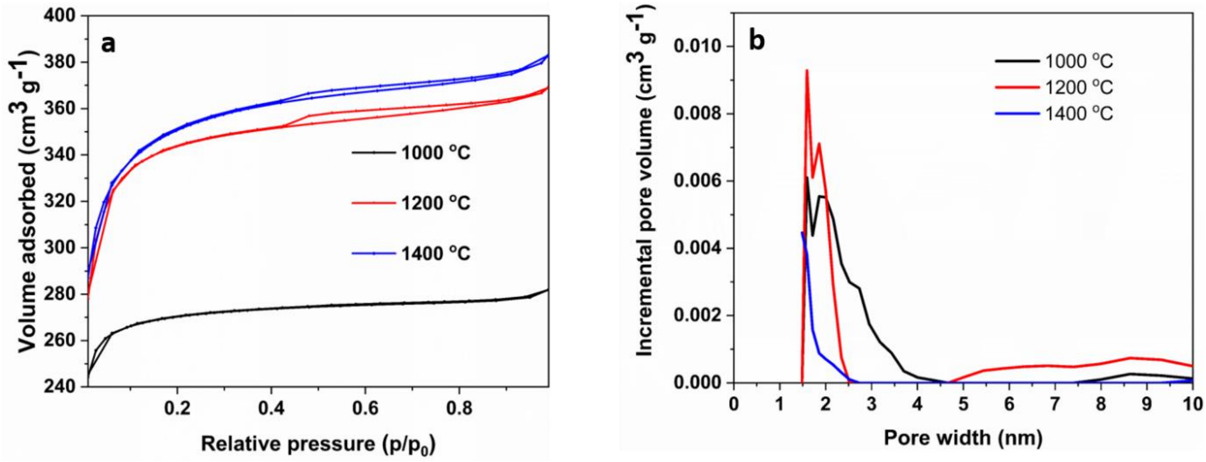

Figure 3-4 (a) N_2 adsorption-desorption isothermal curves and (b) pore size distribution of hard carbon obtained from heating resorcinol-formaldehyde gels at different temperature with Ar gas flow rate of 200 mL min^{-1}.

Table 3-1 BET surface area obtained from cotton wool with different pyrolysis temperature.

	Cotton wool derived hard carbon		resorcinol-formaldehyde gels derived hard carbon	
Temperature (℃)	BET surface area (m2/g)	Yield (%)	BET surface area (m^2/g)	Mass yield (%)
1000	713	11.1	1074	28.8

1200	392	9.4	1011	24.9
1400	346	9.2	785	25.2

3.3.2 Gas flow rate effect on synthesis of hard carbon

In order to check the effect of flow rate, cotton wool derived hard carbon materials have been synthesized with different gas flow rates. As shown in Fig. 3-5, the isotherms keep the features of type IV and H4 type hysteresis with the increasing gas flow rate, indicating the co-existence of micropores and mesopores in the hard carbon. The BET surface area of HC-CW-1400 obtained with the flow rate of 200 mL min^{-1} is 346 m^2 g^{-1} (Table 3-2), while the surface area decreases to 123 and 55 m^2 g^{-1} when the flow rate goes up to 600 and 1000 mL min^{-1}, respectively. During the pyrolysis process, it is reasonable that residual functional groups (e.g. CH_2OH- and OH-) from cotton wool will react with the obtained carbon to produce CO_2 gas. In the low flow rate of protective gas (argon), the produced CO_2 gas will react with the obtained carbon before flushing out the furnace tube, inducing porosity and enhancing the surface area in the final product.[54] The production yield values (Table 3-2) also support this assumption. The higher argon flow rate reduces the burn off during the synthesis process, enhancing the product yield.

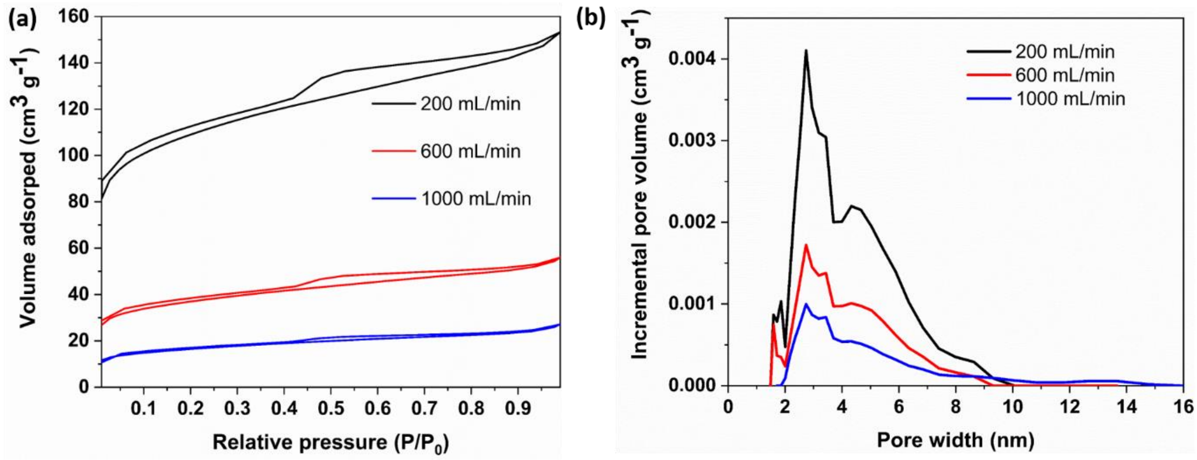

Figure 3-5 (a) N_2 adsorption-desorption isothermal curves and (b) pore size distribution of hard carbon with different argon flow rates at 1400 °C.

Table 3-2 The BET surface area and production yield of hard carbon obtained with different argon flow rates.

Flow rate (mL min^{-1})	BET surface area (m^2 g^{-1})	Mass yield (%)
200	346	9.2
600	123	11.5
1000	55	13.0

3.4 Electrochemical properties in SIBs

3.4.1 Electrochemical performance in hard carbon obtained with different pyrolysis temperature

Fig. 3-6 shows the discharge-charge performance of cotton wool derived hard carbon electrode at current of 20 mA g^{-1}. The initial Coulombic efficiency of HC-CW-1400 is 55.7% (Table 3-3), higher than that of 35.1% and 26.3% for HC-CW-1200 and HC-CW-1000, respectively. The higher initial Coulombic efficiency is due to the lower amount of residual functional groups and smaller surface area with higher pyrolysis temperature, reducing the contact area with the electrolyte and the formation of solid electrolyte interface (SEI).[137,138] Hard carbon electrodes with higher pyrolysis temperatures show a better reversible capacity after six cycles. Both the HC-CW-1000 and the HC-CW-1200 deliver low reversible capacities of 57 and 90 mA h g^{-1}, respectively, while the HC-CW-1400 shows a highest reversible capacity of 154 mA h g^{-1}. It can be seen that the capacity region for the HC-CW-1200 and the HC-CW-1400 can be divided into a slope part above 0.2 V and a plateau part around 0 V, and the HC-CW-1400 shows more capacity during the plateau region than HC-CW-1200, with the HC-CW-1000 only shows the sloping region. As discussed above, the HC-CW-1400 has smallest interlayer distance, more defect sites, narrow pore size distribution, while the HC-CW-1000 material has the largest surface area and shows the most mesoporous structure. The relationship between the structure of HC-CW-T and their corresponding electrochemical performance suggested that the sloping region may be attributed to the sodium ion insertion into the graphene sheets, while the plateau region corresponds to the sodium storage in the defect sites.[83]

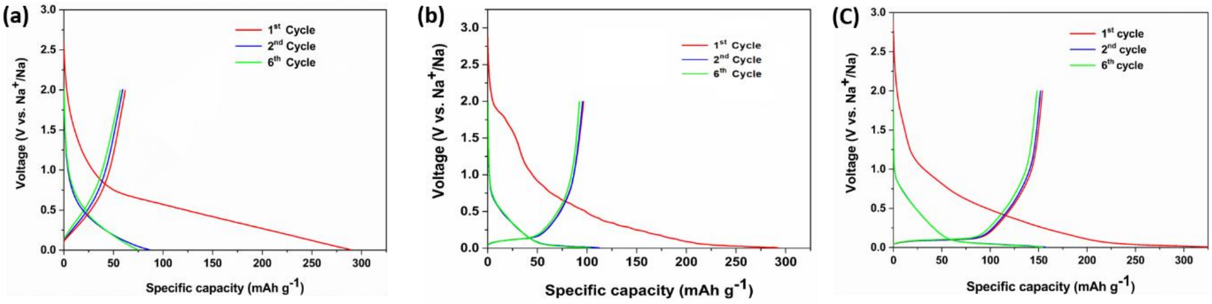

Figure 3-6 Discharge/charge performance of cotton wool derived hard carbon obtained at (a) 1000 °C, (b) 1200 °C, (c) 1400 °C. The profiles obtained between 2.0 and 0.005 V (vs. Na^+/Na) at 20 mA g^{-1}.

Fig. 3-7 shows the electrochemical properties of hard carbon electrodes from resorcinol-formaldehyde gels. The initial Coulombic efficiency is low because of the high surface area, according to the formation of SEI discussed above. The capacity increases from 53 to 151 with increase of synthesis temperature (Table 3-3). The charge-discharge profiles have no obvious plateau part, suggesting the poor adsorption of sodium ions in the micropore structure of resorcinol-formaldehyde gel derived hard carbon during cycling.

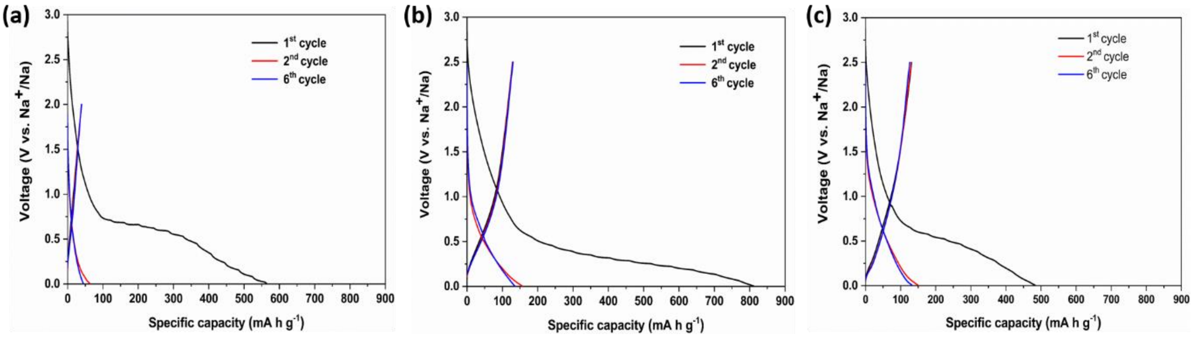

Figure 3-7 Discharge/charge performance of resorcinol-formaldehyde ge derived hard carbon obtained at (a) 1000 °C, (b) 1200 °C, (c) 1400 °C. The profiles obtained between 2.0 and 0.005 V (vs. Na^+/Na) at 20 mA g^{-1}.

Table 3-3 First cycle oxidation capacity and Coulombic efficiency of hard carbon synthesized with different temperatures.

	Cotton wool derived hard carbon		Resorcinol formaldehyde derived hard carbon	
Synthesis temperature	First oxidation capacity (mA h g^{-1})	Initial Coulombic efficiency (%)	First oxidation capacity (mA h g^{-1})	Initial Coulombic efficiency (%)
1000 °C	57	26.3	52.65	9.4
1200 °C	90	35.1	148.7	17.7
1400 °C	154	55.7	151.2	31.2

3.4.2 Electrochemical performance in hard carbon obtained with various gas flow rates

Fig. 3-8 shows the discharge/charge curves of the HC-CW-1400 synthesized at different Ar flow rate. At the current of 20 mA g^{-1}, the HC-CW-1400 obtained at 1000 mL min^{-1} shows the best reversible capacity with 319 mA h g^{-1} in the first cycle, while the HC-CW-1400 obtained at 600 mL min^{-1} and 200 mL min^{-1} have the lower capacity of 289 mA h g^{-1} and 154 mA h g^{-1} in the first cycle. The initial Coulombic efficiency of HC-CW-1400 obtained at 1000 mL min^{-1} is 71.8 %, higher than that of 70.1 % and 55.7 % for the HC-CW-1400 obtained at 600 mL min^{-1} and 200 mL min^{-1}, respectively. The reason is that the HC-CW-1400 synthesized at the higher Ar flow rate has the lower BET surface area, reducing the formation of SEI during the first cycle.[139]

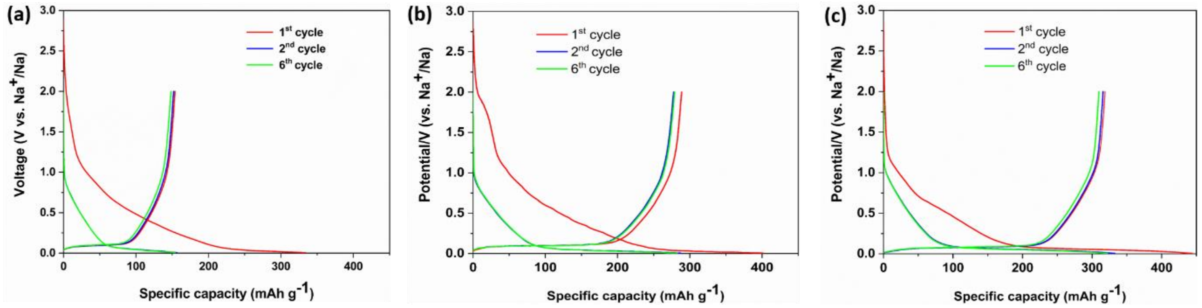

Figure 3-8 Galvanostatic discharge/charge profiles of HC-CW-1400 obtained at the Ar flow rate of (a) 200 mL min^{-1}, (b) 600 mL min^{-1}, (c) 1000 mL min^{-1}. The profiles obtained between 2.0 and 0.005 V (vs. Na^+/Na) at 20 mA g^{-1}.

Table 3-4 First cycle oxidation capacity and initial Coulombic efficiency of hard carbon synthesized with cotton wool with different gas flow rates.

Ar flow rate (mL min-1)	First oxidation capacity (mA h g^{-1})	Initial Coulombic efficiency (%)
200	154	55.7
600	289	70.1
1000	319	71.8

Fig. 3-9 displays the discharge/charge curves of HC-RF-1400 obtained at argon flow rate of 1000 mL min^{-1}. Reversible capacity is around 220 mA h g^{-1} and the initial Coulombic efficiency is 41%, lower than the value obtained from cotton wool derived hard carbon electrodes. In that case, the following study will focus on the hard carbon obtained from cotton wool.

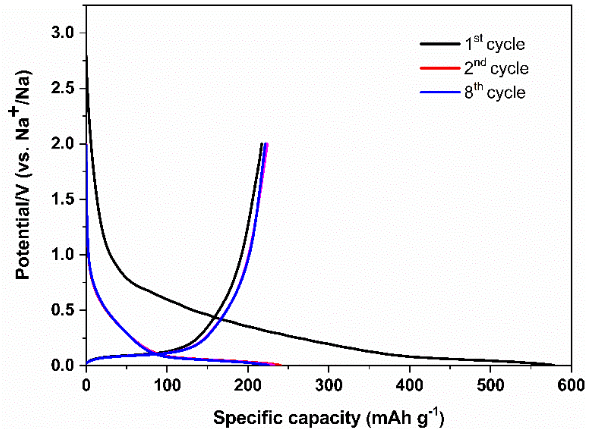

Figure 3-9 Galvanostatic discharge/charge profiles of HC-RF-1400 obtained at the Ar flow rate of 1000 mL min^{-1}. The profiles obtained between 2.0 and 0.005 V (vs. Na^+/Na) at 20 mA g^{-1}.

3.4 Conclusions

Cotton wool and resorcinol-formaldehyde have been used to synthesize hard carbon. Different synthesis conditions such as pyrolysis temperature and gas flow rate have been investigated to find the optimized synthesis route. The sodium storage in hard carbon obtained with different synthesis conditions have been checked. The optimized synthesis condition is the pyrolysis of cotton wool at 1400 ℃ with the argon gas flow rate of 1000 mL min^{-1}. Hard carbon obtained with these synthesis conditions shows a reversible capacity of 319 mA h g^{-1} at current of 20 mA g^{-1}.

4. Synthesis of hard Carbon-TiN/TiC composites by reacting cellulose with $TiCl_4$ followed by carbothermal nitridation/reduction

4.1 Introduction

Titanium nitride and carbide are promising electrode materials in energy storage whilst exhibiting many characteristics such as good thermal stability, electrical conductivity and low cost.[140,141] Carbon-based composites in electrochemical applications provide good electrical conductivity and high chemical resistance. Recently extensive work on supporting a range of materials on carbon to exploit these properties has been reported. For example, Yousef *et al.*[142] embed Co-TiC nanoparticles on carbon nanofibers and then used the composite for fuel cells and dye-sensitized solar cells. Zhang et al.[143] deposited titanium nitride on carbon fibres using a sol-gel method and then applied this coating in flexible supercapacitors. Herein, we report an effective method to obtain HC-TiN or HC-TiC composites by reacting a reactive metal precursor with cellulose before firing to convert the cellulose to HC. Carbothermal nitridation under N_2 gas yielded HC-TiN whereas carbothermal reduction under argon produced HC-TiC. Both composites show similar first cycle capacities to HC, but the titanium nitride composite delivers a better capacity retention (85.2%) after 50 cycles than that of hard carbon (74.3 %).

4.2 Experimental

The composites were synthesized by reacting cotton wool with $TiCl_4$ then firing in nitrogen or argon. Cotton wool (5 g, Fisher Scientific) was dried *in vacuo* overnight. It was then placed into a flask under N_2 and covered with hexane (200 mL, Fisher Scientific, distilled from sodium/benzophenone ketyl ether) followed by addition of different volumes of $TiCl_4$ (between 0 and 0.5mL, Sigma-Aldrich, 99.9% trace metals basis). The mixture was heated to reflux overnight and then the solvent and any remaining precursor was removed in vacuo. The dried material was transferred into a furnace tube in the glove box and then fired under nitrogen or argon. Firing was carried out with a temperature ramp of 4 °C min^{-1} to 1400 °C and this temperature was maintained for 2 h. Pure hard carbon (HC) samples were synthesized for comparison using the same steps but without adding the $TiCl_4$ during synthesis.

4.3 Results and discussions

Scheme 4-1 illustrates the synthesis process of the HC-TiN and HC-TiC composites. The main component in cotton wool is cellulose (~95%), which is a polymer of β-D-glucose. The hydroxide groups on the cellulose are expected to react with the $TiCl_4$ to form C-O-Ti bonds with HCl as the byproduct. Initially reactions were carried out at room temperature since the $TiCl_4$ was expected to be highly reactive with these hydroxide groups, but it was found that titanium loadings on the cellulose were higher when the solution was refluxed. This may be related to poor wetting of the polar cellulose surfaces by the low polarity hexane solvent. Different volumes of $TiCl_4$ (Table 4-1) were added to obtain titanium-containing composites with different composition. After firing, composites of TiN or TiC with hard carbon were produced.

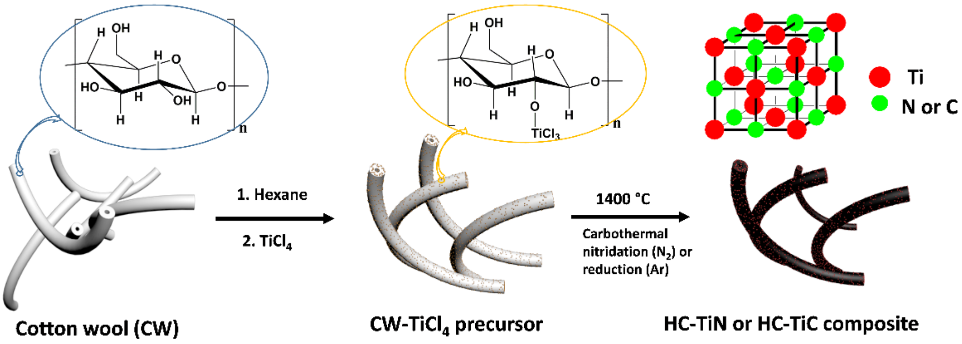

Scheme 4-1 The synthesis process used to make HC-TiN and HC-TiC composites.

Table 4-1 Physical parameters of HC-TiN and HC-TiC composites.

Sample	TiCl$_4$ used in synthesis (mL)	HC parameters		TiN/TiC parameters		Composite surface area (m^2/g)
		d (002) (Å)	I$_D$/I$_G$	a=b=c (Å)	Crystallite size (Å)	
HC-N$_2$(1)	0	3.842(7)	1.71	n/a	n/a	61
1.89% *wt* TiN	0.1 mL	3.887(5)	1.82	4.24714(4)	36(5)	111
8.57% *wt* TiN	0.2 mL	3.915(6)	1.86	4.24262(5)	179(8)	89
10.14% *wt* TiN	0.3 mL	3.939(5)	1.94	4.24599(3)	191(27)	79
15.15% *wt* TiN	0.4 mL	3.962(7)	1.97	4.24430(7)	239(5)	73
17.27% *wt* TiN	0.5 mL	3.964(5)	2.03	4.24113(7)	340(19)	71
HC-Ar(2)	0	3.803(5)	1.58	n/a	n/a	57
4.28% *wt* TiC	0.1 mL	3.934(5)	1.86	4.32272(2)	191(9)	92
8.65% *wt* TiC	0.2 mL	3.967(8)	1.97	4.304718(14)	314(5)	82
16.27% *wt* TiC	0.4 mL	3.988(5)	2.16	4.31932(3)	380(12)	41

(1) Hard carbon obtained under nitrogen gas; (2) Hard carbon obtained under argon gas.

The amount of the titanium-containing phase in these composites was measured by heating the samples in the TGA (Fig. 4-1) to remove the carbon and oxidize the titanium to TiO$_2$.

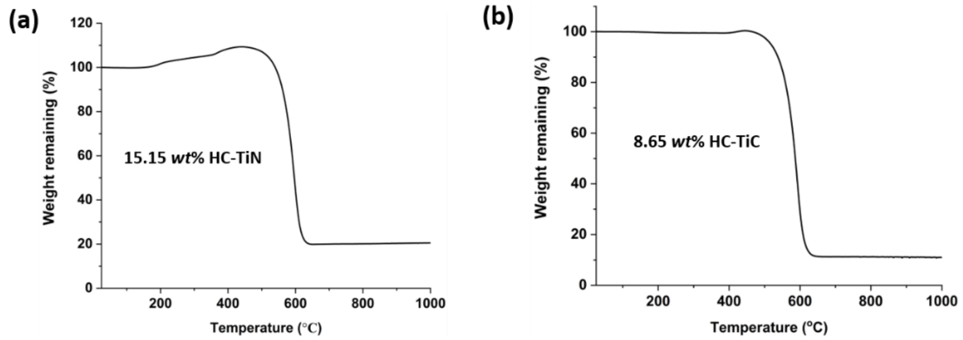

Figure 4-1 TGA analysis of (a) 15.15wt% HC-TiN and (b) 8.65 wt% HC-TiC composites.

$$aC + bTiN + (a + 2b)O_2 \rightarrow bTiO_2 + bNO_2 + aCO_2 \qquad \text{Equation 4-1}$$

61.87 79.85

mx 79.85mx/61.87

Assume the weight of composite is “m” gram, and the mass ratio of TiN in composite is “x”. The calculated TiO_2 should be 79.85mx/61.87 after heating at 1000 °C. The weight remaining is 19.55% from thermogravimetric analysis. In that case, the value of x should be 0.1515.

The fibrous microstructure of the cellulose is obvious in the SEM images of the HC, even after grinding the samples (Fig. 4-2, 4-3).

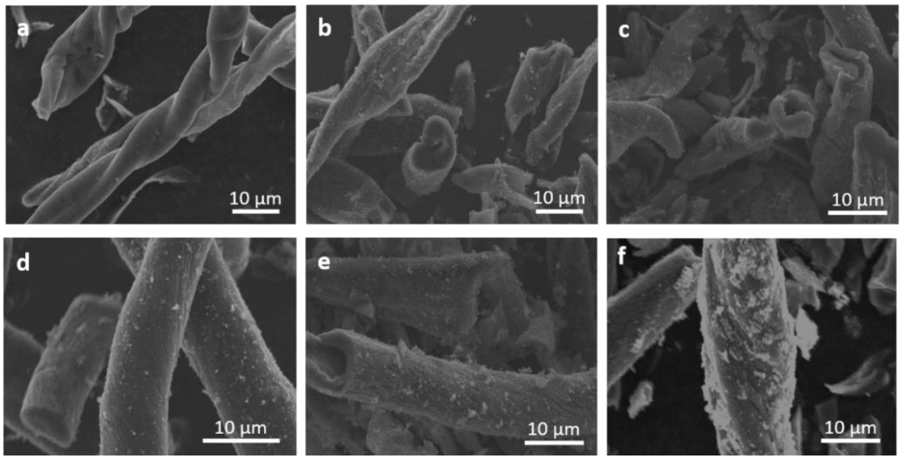

Figure 4-2 SEM images of HC-N_2 and HC-TiN composites with different mass ratios of TiN in the composites: (a) 0; (b) 1.89%; (c) 8.57%; (d) 10.14%; (e) 15.15%; (f) 17.27%.

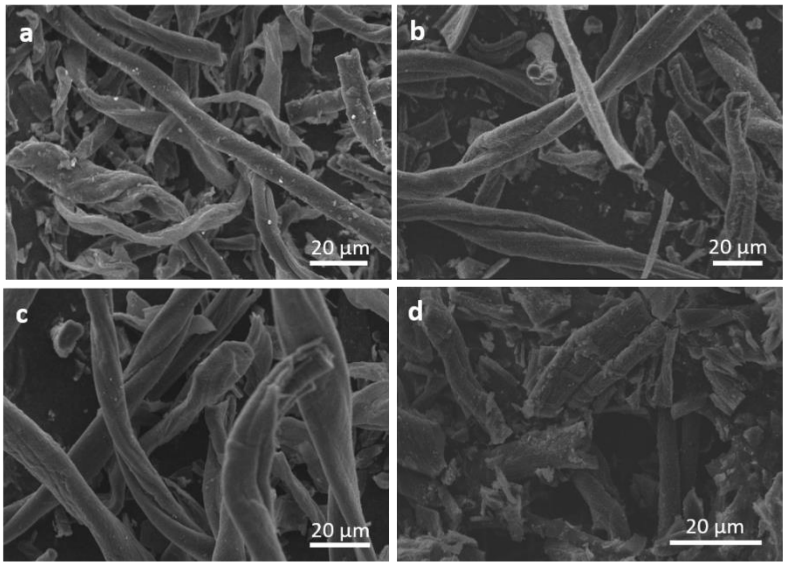

Figure 4-3 SEM images of HC-Ar and HC-TiC composites with different mass ratios of TiC in the composites: (a) 0; (b) 4.28%; (c) 8.65%; (d) 16.27%.

Samples that had been reacted with $TiCl_4$ before pyrolysis had an obvious surface roughening, increasing with the titanium loading and with nanoparticles visible on the surfaces of the fibrous structures, and TEM images confirmed this observation as well as showing crystallite sizes consistent with those listed in Table 1 (Figs. 4-4, 4-5). The images suggest that the surfaces are quite consistent within a particular sample and the corresponding EDX mapping images (Fig. 4-4) reveal that the distribution of titanium across the HC structure is very uniform.

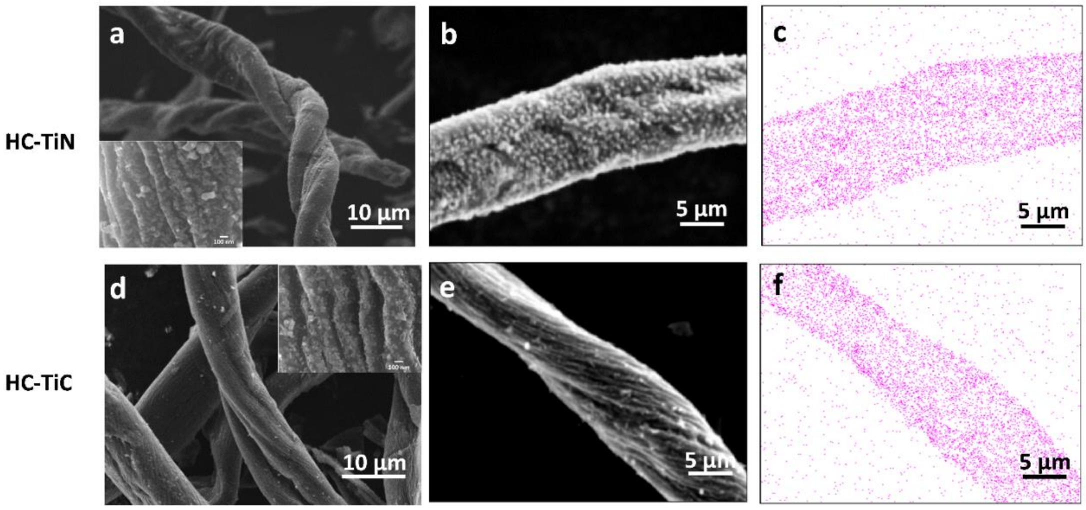

Figure 4-4 SEM images of 15.15 *wt*% HC-TiN (a and b) and 8.65 *wt*% HC-TiC (d and e) composites. The purple dots in the EDX maps (c and f) represent the dispersion of titanium in these samples and are acquired in the same regions as the corresponding SEM images (b and e).

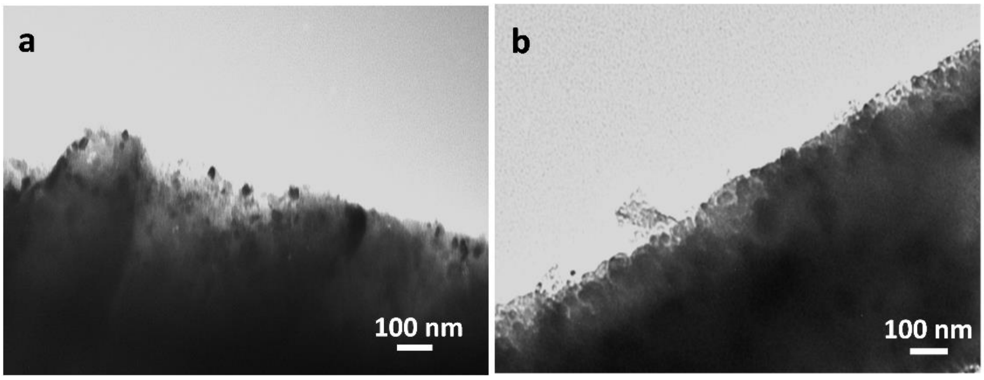

Figure 4-5 TEM images of 15.15 *wt*% HC-TiN (a) and 8.65 *wt*% HC-TiC (b) composites showing crystallites at the surfaces and hard carbon domain features in the body of the fibers.

Fig. 4-6 displays the XRD patterns of composites with different mass contents of titanium nitride or carbide. The broad peaks around 23° correspond to the 002 peak of the graphitic domains of the hard carbon[54]. This peak can be used to calculate the interlayer d-spacing of the hard carbon (Table 4-1), which was found to increase with titanium loading. A wider interlayer separation has been linked to better sodium ion insertion and deinsertion,[144] and may suggest some limited titanium insertion between the layers. The interlayer spacing of thermally expanded graphite can reach 0.43 nm,[145] and others have observed increased interlayer spacings on introducing aluminium ions into graphite[146], so the increases in interlayer spacing observed here are plausible. A second broad HC feature is also observed around 44°, corresponding to the 100 peak of the graphitic domains.

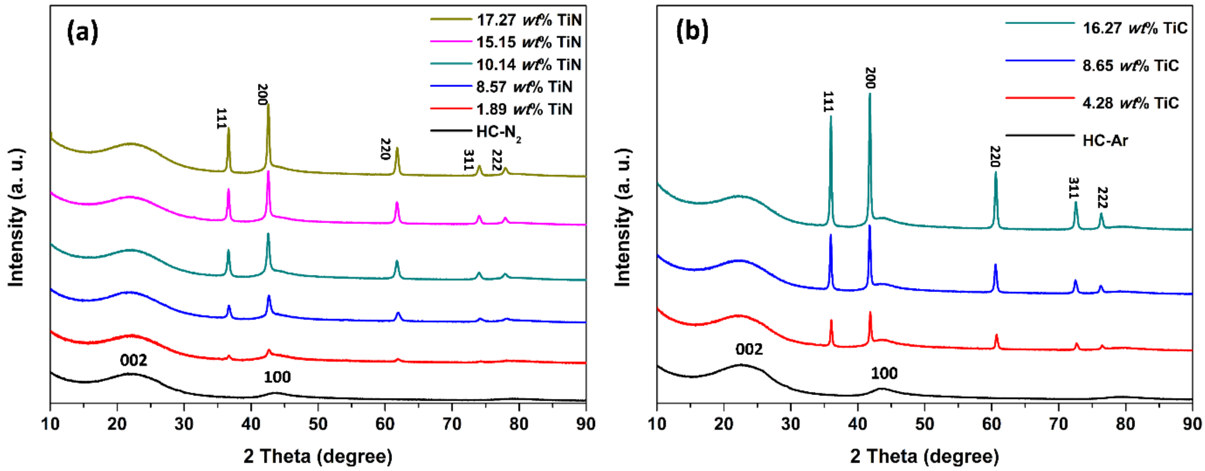

Figure 4-6 The XRD patterns of HC-TiN (a) and HC-TiC (b) composites, with loadings as shown.

As the titanium loading increased, the sharper peaks increased in intensity. These had the familiar rocksalt-type pattern expected for the cubic TiC, TiN or TiO. The patterns were refined and the extracted lattice parameters are shown in Table 4-1. In Fig. 4-7 the lattice parameters are compared with those reported in the Inorganic Crystal Structure Database (ICSD)[147] for the TiC, TiN or TiO phases that were considered to be potential constituents of the composites. It can be seen that the lattice parameter decreases fairly linearly from TiC (~4.32 Å) to TiN (~4.24 Å) and TiO (~4.17 Å), and that the reported lattice parameters for these phases occur in quite narrow bands. The lattice parameters from Table 4-1 are shown as two bands in Fig. 4-7, where it is clear that the composites fired in nitrogen all have lattice parameters close to the ICSD values for TiN, and those fired in argon are all close to TiC. These systems are known to form solid solutions and the presence of the other two anions in the samples cannot be ruled out, but this is difficult to measure in the presence of a large excess of carbon. For both composites, the diffraction peaks become narrower as the titanium loading increases, implying that the crystallite sizes become larger. The HC-TiN composites have broader diffraction peaks than the HC-TiC composites with similar $TiCl_4$ concentrations. Crystallite size of TiN varies from 3.6 to 34.0 nm while that of TiC varies from 19.1 to 38.0 nm (Table 4-1, data fitted in the PDXL software).

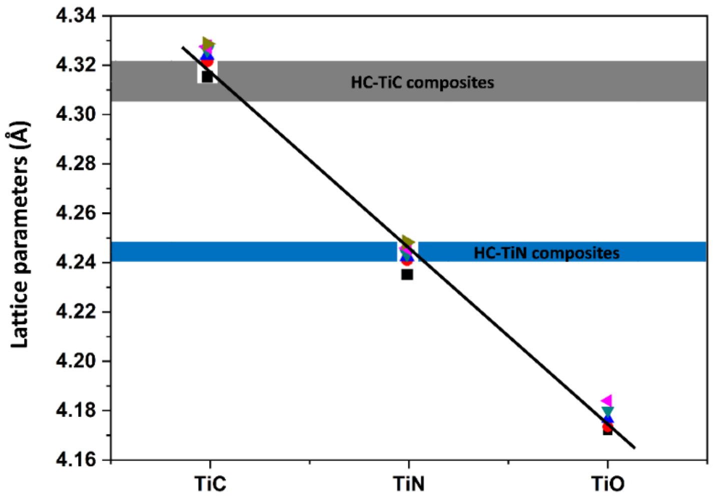

Figure 4-7 Symbols and best-fit line showing the literature lattice parameters of TiC[148-152], TiN[149, 153-157] and TiO[158-162] from ICSD.[147] The blue and grey banded regions represent the range of lattice parameters found for the components designated as TiN or TiC (Table 4-1) in the composites obtained in this study.

The melting points of titanium nitride and titanium carbide are 3228 K (2930 °C) and 3458 K (3160 °C), respectively. Tammann temperatures are typically 50-75% of the melting point and are expected to be above 1614 K and 1729 K, respectively. The synthesis temperature in our experiment is 1698 K (1400 °C). Hence the larger titanium carbide crystallite sizes are not consistent with annealing rates at this firing temperature. On the other hand, the synthesis temperature is 86% of the melting point of titanium (1966 K or 1668 °C), which is a potential intermediate during the synthesis process. After reaction with the oxidic cellulose surface the titanium is likely to be present in a form chemically similar to TiO_2. The high temperature synthesis is likely to involve carbothermal reduction of the titanium-containing species either combined with (equations (4-2) and (4-3)), or followed by (equations (4-4) to (4-5)), reaction with gaseous nitrogen or further carbon from the HC surface. The larger crystallite sizes of TiC suggest that equations (4-4)-(4-6) are important, since if the more sinterable titanium metal is present during the synthesis it could react more rapidly utilizing gas phase diffusion of nitrogen to make TiN than solid state diffusion of carbon to make TiC.

$$\mathrm{Ti}O_2 + \frac{1}{2}N_2 + 2\mathrm{C} \rightarrow \mathrm{TiN} + 2\mathrm{CO} \qquad \text{Equation 4-2}$$

$$\mathrm{Ti}O_2 + 3\mathrm{C} \rightarrow \mathrm{TiC} + 2\mathrm{CO} \qquad \text{Equation 4-3}$$

$$\mathrm{Ti}O_2 + 2\mathrm{C} \rightarrow \mathrm{Ti} + 2\mathrm{CO} \qquad \text{Equation 4-4}$$

$$\mathrm{Ti} + \frac{1}{2}N_2 \rightarrow \mathrm{TiN} \qquad \text{Equation 4-5}$$

$$\mathrm{Ti} + \mathrm{C} \rightarrow \mathrm{TiC} \qquad \text{Equation 4-6}$$

Raman spectroscopy is particularly useful to investigate the HC component of the composites when the PXRD is dominated by the metal nitrides.[163] In Fig. 4-8, the Raman plots show broad peaks due to hard carbon around 1310 and 1595 cm^{-1}, which can be attributed to the disordered (D-band) and ordered graphitic (G-band) structures in hard carbon, respectively.[54,126] The integrated intensity of the D-band is stronger than that of G-band, suggesting that the composites retain the highly disordered graphitic structure of hard carbon. The integrated intensity ratio I_D/I_G goes up from 1.71 to 2.03 (Table 4-1) with increasing titanium loading in HC-TiN composites, and from 1.58 to 2.16 (Table 4-1) with increasing titanium in HC-TiC. This suggests that the presence of TiN or TiC in the composites increases disorder, in accordance with previous reports of introducing metallic atoms to an amorphous substrate.[164,165]

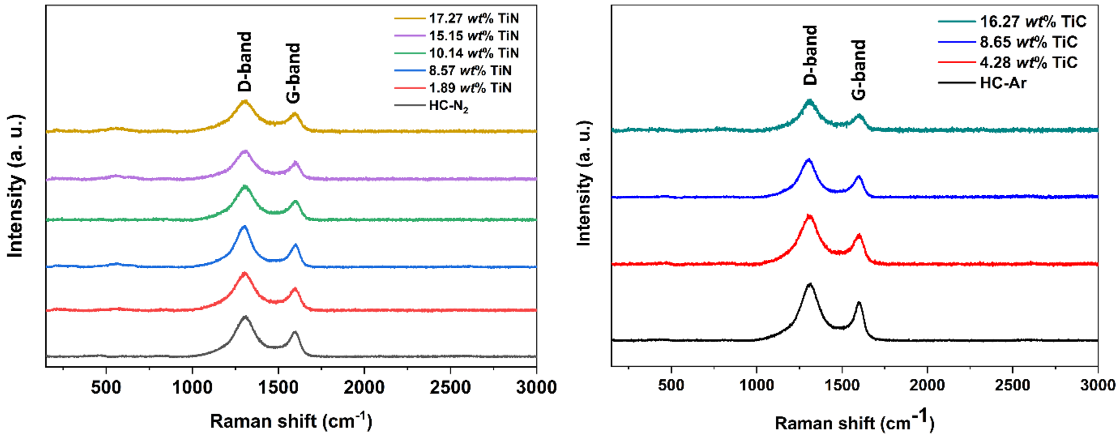

Figure 4-8 Raman spectra of HC-TiN (a) and HC-TiC (b) composites with titanium loadings as marked.

There are no obvious strong peaks between 300 and 600 cm^{-1}, where the presence of any titanium dioxide would be expected to produce strong peaks (Fig. 4-9).[163]

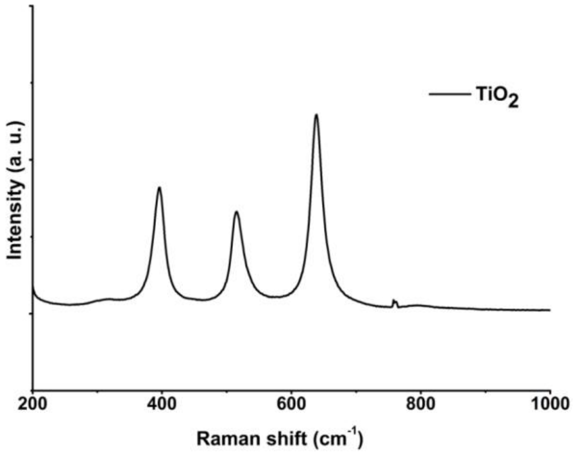

Figure 4-9 Raman spectrum of commercial TiO_2 (Sigma-Aldrich, anatase, ≥ 99%) with Raman shift between 200 and 1000 cm^{-1}.

XPS data for the non-loaded HC samples can be seen in Fig. 4-10. The C 1s deconvolution spectra show binding energies of 284.5 and 284.6 eV, respectively, which are typical of sp^2 carbon.[166] The peaks with higher binding energy can be attributed to sp^3 C, C-O, C=O, and π-π* shake-up satellites.[144,166] The high peak intensity ratio of sp^2/sp^3 suggests high levels of structural defects in the hard carbon[167], corroborating the above Raman discussion. The N 1s spectrum only shows a small nitrogen component (0.1 % atom concentration) in HC-N_2 and more discussion will be given later.

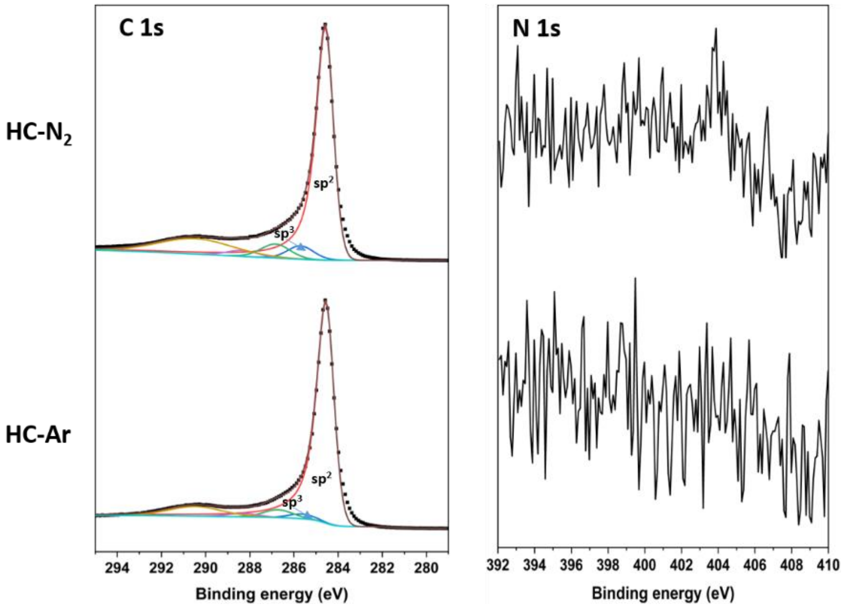

Figure 4-10 XPS deconvolution spectra of C 1s, and N 1s of HC-N_2 and HC-Ar.

The survey spectra and high resolution XPS spectra of the HC-TiN and HC-TiC composites are shown in Fig. 4-11 and 4-12. The atomic concentration of C: N: O: Ti is 83.4: 4.7: 7.9: 4.0 in HC-TiN composite, while that of C: O: Ti is 92.5: 5.1: 2.4 in HC-TiC composite. Peak attributions from the C 1s, O 1s, N 1s and Ti 2p core-level regions are collected in Table 4-2. The obvious peak at lower binding energy of 281.8 eV in HC-TiC is associated with TiC and the smaller shoulder at 283.0 eV corresponds to titanium subcarbide.[168] The Ti $2p_{3/2}$ feature at 455.1 eV in HC-TiC also shows the presence of TiC. The peak at 455.4 eV corresponds to TiN in HC-TiN composite, while the peak at higher binding energy of 456.4 eV can be assigned to Ti-O-N, due to charge transfer from Ti to O that causes the chemical state shift toward to higher binding energy.[169-171] The peaks at 458.5 and 458.7 eV correspond to the surface oxide from HC-TiN and HC-TiC, respectively. The presence of surface oxidation is also in consistent with the analysis of the O 1s spectrum. The core-level O 1s peaks at 530.1 eV can be attributed to surface oxidation of the composites, which were handled in air before loading into the instrument.[169,172] Another two peaks with higher binding energy are from absorbed carbonyl groups,[173] which is consistent with discussion of the C 1s. The peak at 397.4 eV in the N 1s spectrum indicates stoichiometric TiN.[172] The peak appears at a lower binding energy of 396.3 eV corresponds to oxynitride species, which is consistent with the Ti-O-N components in Ti 2p analysis. The components at 398.5 and 401.1 eV can be related to oxygen species and free molecular N_2 on the surface of TiN, respectively.[172] The N 1s spectrum in Fig. 4-10 shows a small nitrogen component (0.1 % atom concentration) in HC-N_2, and the spectrum fitting is good without the presence of C-N in HC-TiN, suggesting no obvious evidence of nitrogen doping in hard carbon or in HC-TiN composite. Some XPS studies use Ar^+ etching before measurement,[174,175] and without this step it is unsurprising that surface oxide is seen (the XRD and Raman suggest it is thin), although working without etching should show more representative surface chemistry. The XPS data confirm the presence of TiN and TiC on the carbon surfaces, consistent with the XRD and Raman analysis.

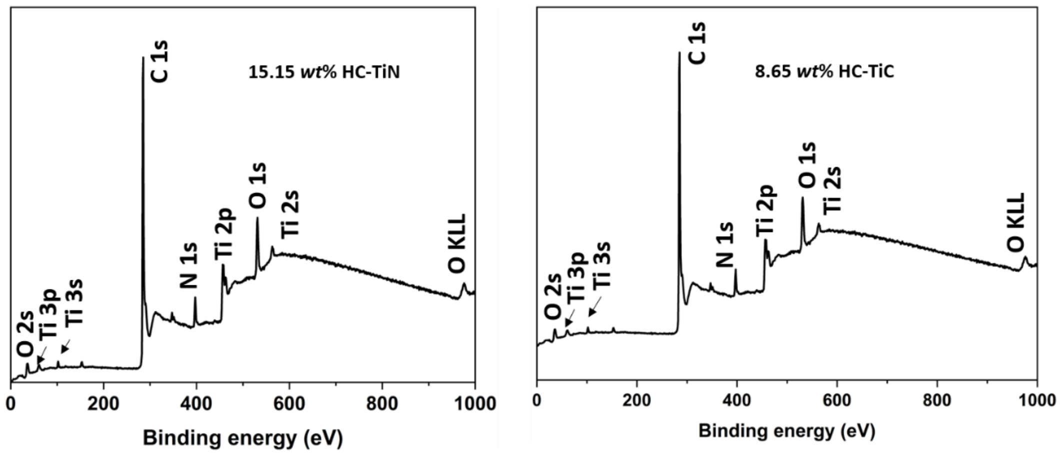

Figure 4-11 XPS survey spectra of (left) 15.15 *wt*% HC-TiN composite and (right) 8.65 *wt*% HC-TiC composite.

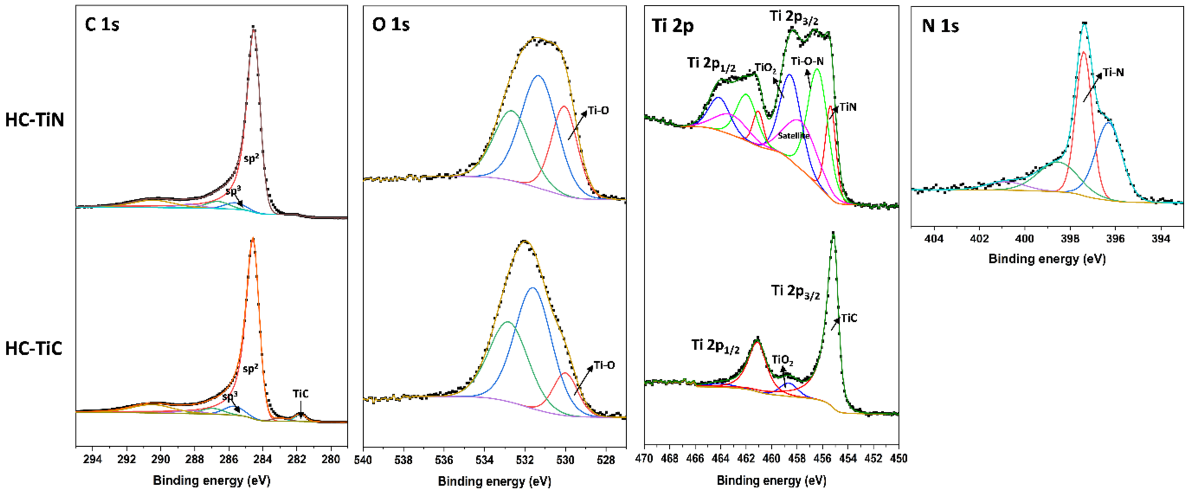

Figure 4-12 High resolution XPS spectra of the C 1s, O 1s, N 1s and Ti 2p regions for HC-TiN and HC-TiC composites with 15.15 *wt*% TiN and 8.65 *wt*% TiC, respectively.

Table 4-2 C 1s, O 1s, N 1s and Ti 2p core-level XPS peaks with likely chemical states

Material	C 1s		O 1s		Ti $2p_{3/2}$		N 1s	
	BE (eV)	State	BE (eV)	State	BE (eV)	State	BE (eV)	State
HC-TiN	284.5	C-C, sp^2	530.1	O-Ti	455.4	Ti-N	396.3	N-O-Ti
	285.6	C-C, sp^3	531.3	O=C	456.4	Ti-O-N	397.4	N-Ti
	286.7	C-O	532.6	O-C	457.7	Satellite	398.6	N-O
	288.3	C=O			458.5	TiO_2	400.99	N_2
	290.4	Satellite						
HC-TiC	281.8	C-Ti	530.1	O-Ti	455.1	Ti-C		

283.0	subcarbide	531.6	O=C	458.8	TiO_2
284.6	C-C, sp^2	532.8	O-C		
285.7	C-C, sp^3				
286.9	C-O				
288.3	C=O				
290.5	Satellite				

N_2 adsorption and desorption isotherms of the HC-TiN and HC-TiC composites are shown in Fig. 4-13. All can be classified as type IV with H4 hysteresis, implying that the materials possess mesoporous.[176] A feature common to these hysteresis loops is that complete closure points should appear at nitrogen's boiling point around $P/P_0 = 0.42$. However, for some materials containing micropores, low pressure hysteresis can be extended to the lowest attainable pressures as seen in these isotherms.[133-135] The pore size distribution (Fig. 4-14) shows a range of sizes from below 2 nm to around 14 nm. At low concentration of $TiCl_4$, the specific surface area (Table 4-1) of the composites increases when compared with the pure hard carbon. That may be because of particles forming on the surface or the reaction between the titanium chloride and the cellulose may roughen the surface. Further increases in titanium loading increase the TiN or TiC particle size, and then the surface area does not increase further (HC-TiN) or decreases (HC-TiC). The reduced surface area may also be due to covering or filling of micropores near the surface of the HC.

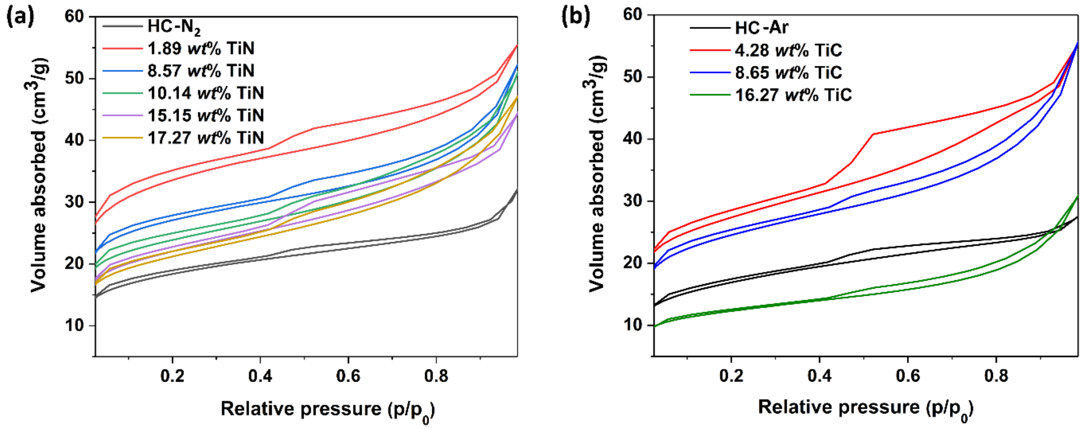

Figure 4-13 N_2 adsorption and desorption profile of HC-TiN (a) and HC-TiC (b), with loadings as shown.

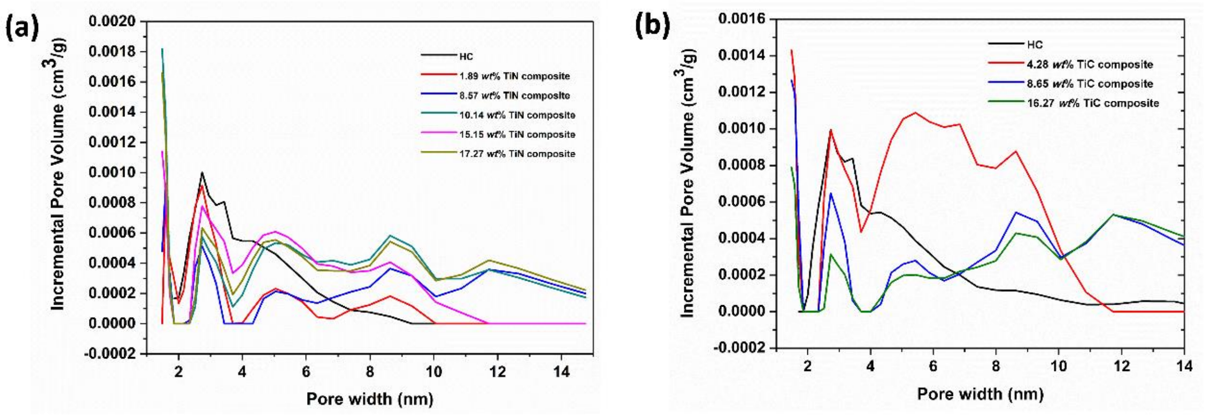

Figure 4-14 Pore size distribution of HC-TiN (a) and HC-TiC (b), with loadings as shown. Data obtained by DFT method.

Fig. 4-15 shows the first cycle differential capacity plot of composites with different TiN loading. The irreversible peak around 0.6 V in the first cycle can be assigned to the formation of SEI layer. [177] The pair of sharp redox peaks around 0.1 V can be attributed to the sodium insertion/disinsertion in the hard carbon.[55,56]

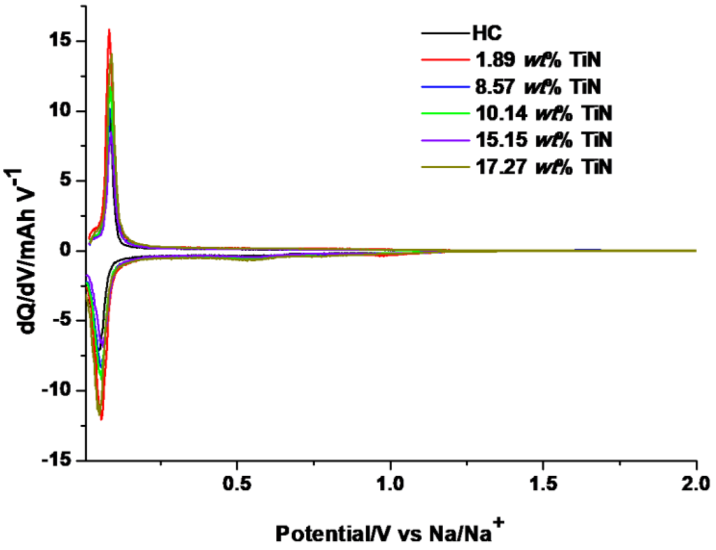

Figure 4-15 The first cycle of dQ/dV vs potential curve obtained from HC and 15.15 *wt*% HC-TiN composites.

The viability of the composites for sodium-ion battery applications was tested in sodium half cells with a 1 mol dm^{-3} $NaClO_4$ in 1:1 EC/DEC electrolyte. Fig. 4-16 shows the first cycle of charge-discharge profiles of the pure HC fired in N_2 and HC-TiN composites and The pure hard carbon has the highest first cycle specific capacity of 290.7 mA h g^{-1} at current of 50 mA mA g^{-1}, which is a competitive value compared with the capacities of other hard carbons obtained from various biomass sources. For example, Hu[45] reported leaf-based carbon and the charge capacity is 270 mA h g^{-1} at 40 mA g^{-1}. Xu[32] obtained nitrogen-rich hard carbon by the pyrolysis of shrimp skin with the capacity of 276 mA h g^{-1} at a current of 100 mA g^{-1}. Ding[55] synthesized hard cabron from peat moss with capacity of 298 mA h g^{-1} at current 50 mA g^{-1}.

The values for the HC-TiN composites were all similar to 290.7 mA h g^{-1}. (280.6 mA h g^{-1} at 1.89 *wt*%; 273.3 mA h g^{-1} at 8.57 *wt*%; 271.4 mA h g^{-1} at 10.14 *wt*%; 283.4 mA h g^{-1} at 15.15 *wt*%; 261.1 mA h g^{-1} at 17.27 *wt*%). The low firstcycle Coulombic efficiency of pure HC (68.4% efficiency) is mainly caused by the formation of the solid electrolyte interface (SEI), which is proportional to the surface area of HC exposed to the electrolyte.[177] The measured BET surface area of 15.15 *wt*% HC-TiN composite is 73.1 m^2 g^{-1}, which may explain its slightly lower first cycle Coulombic efficiency (66.8%), and utilization of this material might require pre-sodiation.

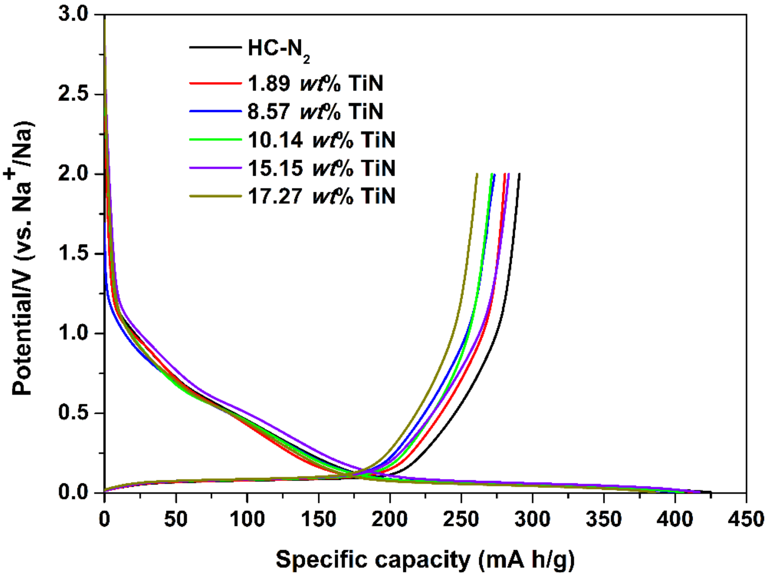

Figure 4-16 First cycle charge-discharge profiles of HC-N_2 and HC-TiN compositions between 2.0 and 0.005 V (vs. Na^+/Na) at 50 mA g^{-1}.

The 15.15 *wt*% HC-TiN composite continued to have similar capacities to those of HC over the first 20 charge/discharge cycles, but then as the capacity of HC drops the composite exhibits a better capacity retention (Fig. 4-17). At the 50th cycle, the HC-TiN composite had a Coulombic efficiency of 99.5% and reversible capacity of 241.5 mA h g^{-1}, 85.2% of its initial capacity. The HC had a 50th cycle capacity of 215.9 mA h g^{-1}, retaining 74.3% of its initial value.

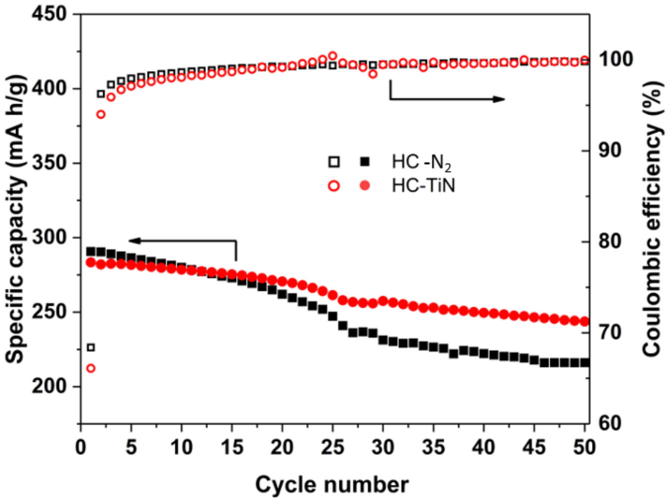

Figure 4-17 Cycling performance of HC-N_2 and the 15.15 *wt*% HC-TiN composite between 2.0 and 0.005 V (vs. Na^+/Na) at 50 mA g^{-1}.

Electrochemical impedance spectroscopy (Fig. 4-18) shows that the HC and 15.15 *wt*% HC-TiN composite have similar charge transfer resistances (R_{ct}) initially, but that after 50 cycles the HC had become more resistive (R_{ct}=296 Ω) than the composite (R_{ct}=105 Ω), suggesting that the highly conductive TiN on the surface plays a role to improve the charge transfer kinetics.

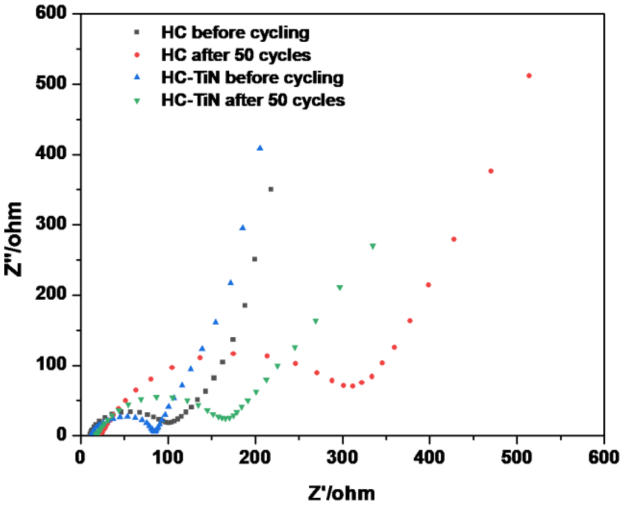

Figure 4-18 Nyquist plots of HC and 15.15 *wt*% HC-TiN composites before and after 50 cycles.

Ex situ grazing incidence XRD patterns of the HC-TiN composites removed from cells at various stages of cycling (Fig. 4-19) showed Cu from the backing foil and TiN. The TiN particle size decreases from 14.7 to 11.2 nm (Table. 4-3) after the first reduction process. In the tenth cycle, the particle size almost has no change in the reduced or oxidized electrode, which may be due to reactions occurring only on the surface of TiN. Refinements of the data showed no change in the lattice parameter comparing the reduced *vs* oxidized materials or comparing the materials after 1 *vs* 10 cycles (Table 4-3). A previous study showed that titanium nitride can be reduced to the metal in lithium batteries,[178] but its storage mechanism in sodium batteries is not clear. Research in our group[105,106,123,124] has shown that in several cases only the surface of metal nitrides reacts, and the small variations seen here suggest that TiN has only reacted in the surface region during cycling *vs* sodium.

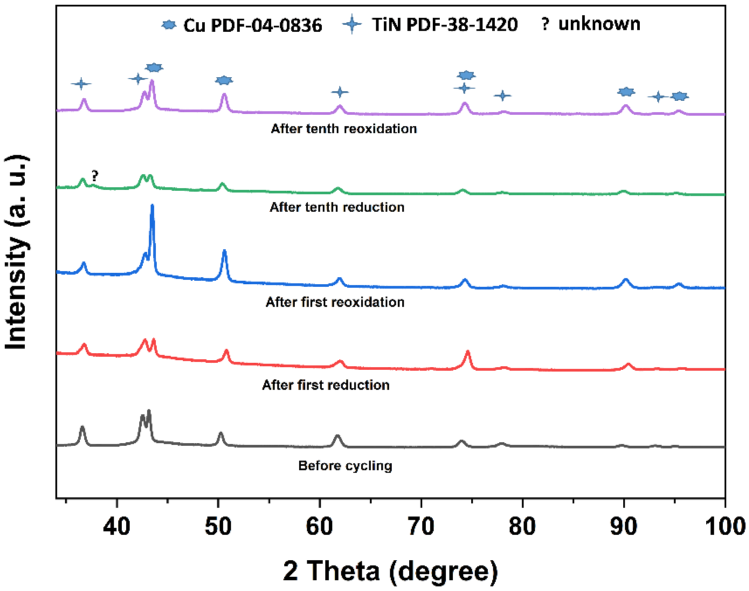

Figure 4-19 *Ex situ* grazing incidence XRD patterns of 15.15 *wt*% HC-TiN composite-based electrodes at various stages of cycling when reducing to 5 mV and oxidizing back to 2 V.

Table 4-3 Lattice parameters of TiN in the composites before cycling and after different cycling times.

Galvanostatic cycling stage at which sample was removed from cell	Particle size (Å)	TiN Lattice parameter (Å)	R_{wp} (%)	R_p (%)
Before cycling	147(12)	4.24476(19)	2.9	2.1
After first reduction	112(5)	4.24215(15)	3.5	2.8
After first reoxidation	95(15)	4.2439(3)	3.3	2.4
After tenth reduction	91(19)	4.2416(2)	2.9	2.3
After tenth oxidation	91(15)	4.23701(13)	3.2	2.5

Galvanostatic cycling of the HC-TiC composite electrodes (Fig.4-20) showed the 8.65 *wt*% HC-TiC composite electrode to have the best capacity (280.8 mA h g^{-1}), again a little lower than the pure HC fired in Ar (284.5 mA h g^{-1}). The capacity of the other composites was 263.7 mA h g^{-1} in 4.28 *wt*% HC-TiC and 247.8 mA h g^{-1} in 16.27 *wt*% HC-TiC.

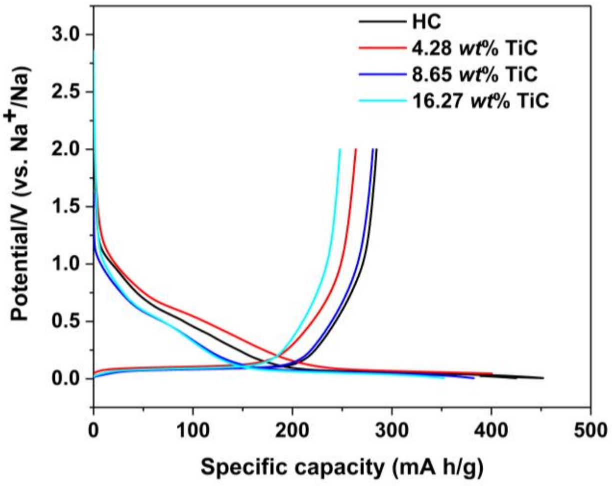

Figure 4-20 First cycle charge-discharge profiles of HC-Ar and HC-TiC composites electrodes between 2.0 and 0.005 V (vs. Na^+/Na) at 50 mA/g

Previous studies show TiC can be used to increase the conductivity of composite electrodes,[179,180] thus enhancing the capacity. This is not observed here, the TiC composites produce slightly lower capacities and, unlike TiN, do not improve the cycling behavior (Fig. 4-21). The larger TiC crystallite size of TiC in HC-TiC composite may reduce its ability to participate in reactions, or the TiC surfaces may be less reactive than the TiN. The coulombic efficiency of the 8.65 *wt*% HC-TiC composite was 99.6% after 50 cycles, while the capacity decreased from 280.8 to 186.8 mA h g^{-1} after 50 cycles, a capacity retention of 66.5%.

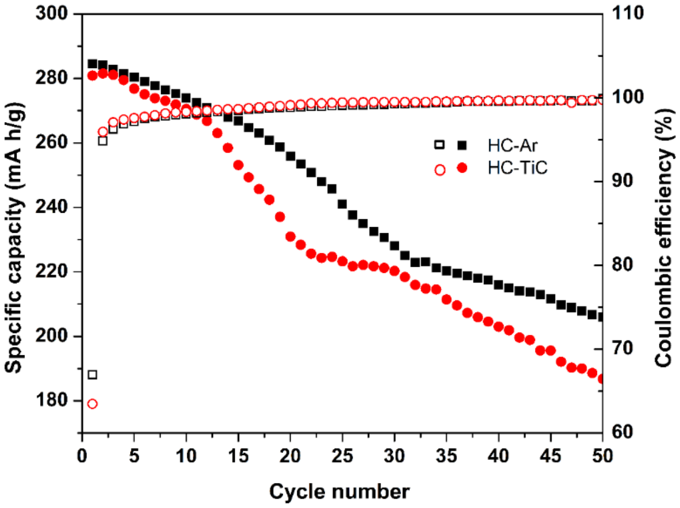

Figure 4-21 Cycling performance of HC-Ar and the 8.65 *wt*% HC-TiC composite between 2.0 and 0.005 V (vs. Na^+/Na) at 50 mA g^{-1}.

The HC-TiN composites prepared by the new methodology presented above have some promise in SIBs and the method is applicable to depositing other metal nitrides or carbides on the carbon surfaces. This could be for batteries, but the literature[181,182]also suggests that such carbon-metal nitride/carbide composites could be applied in electrocatalysis and supercapacitors.

4.4 Conclusions

Reactions of titanium tetrachloride with cellulose followed by carbothermal nitridation or reduction during firing produce hard carbon with nanocrystalline titanium nitride or carbide decorated over the surfaces. In sodium cells both composites show similar first cycle capacities to hard carbon, but the titanium nitride composite delivers a better capacity retention (85.2%) after 50 cycles than that of hard carbon (74.3 %). Moreover, we expect the synthesis method demonstrated here will provide an effective way to obtain composites with other metal nitrides and carbides for sodium cell and other energy applications.

5. Synthesis of vanadium nitride-hard carbon composites from cellulose and their performance for sodium ion batteries

5.1 Introduction

Vanadium nitride (VN) has a cubic and NaCl structure type. It has been used in the sodium ion battery due to the good conductivity and high theoretical capacity. The use of VN in sodium ion batteries was first studied by Cui et al.[107] who reported VN microparticles with stable, reversible capacity of ~300 mA h g^{-1} at 124 mA g^{-1} and reported HRTEM and XANES data that suggested the conversion of VN to $VN_{0.35}$ as part of the mechanism of charge storage. Yuan[110] *et al* developed VN nanocrystals embedded into N-doped hollow carbon spheres that delivered a capacity of 360 mA h g^{-1} at 100 mA g^{-1} in sodium half cells. Song[111] reported VN quantum dots dispersed onto graphene with a reversible capacity of 237 mA h g^{-1} at 74 mA g^{-1}. More recently, Wei *et al*[183] reported a new layered VN material that delivered a capacity of 372 mA h g^{-1} at 50 mA g^{-1}.

Based on the outstanding theoretical capacity of VN of 1238 mA h g^{-1}, associated to the three electron transfer by completely reducing V^{3+} to V^0, and encouraged by the promising electrochemistry of VN-based materials for sodium-ion applications reported in previous studies, here we selected VN as a high capacity material to deposit onto a hard carbon (HC) to improve its performance. We employ a cheap and high-performance hard carbon made from cotton wool as a baseline material, which delivered a reversible capacity of 302 mA h g^{-1} at 50 mA g^{-1}, comparable to the state-of-the-art hard carbon electrodes for sodium ion batteries. VN is relatively expensive and undergoes a significant volumetric expansion in the conversion reaction with sodium, therefore, VN is incorporated in the form of small nanoparticles deposited on the hard carbon surface, and the mass percentage of VN in the composite is kept below 15%*wt*.

The preparation of the hard carbon decorated with VN nanoparticles was achieved *via* the reaction of the hard carbon precursor (cotton wool) with a vanadium source ($VOCl_3$), followed by firing under N_2 to form a hard carbon material with a thin, homogeneously dispersed VN coating. This novel synthesis method uses a single firing step (that is required anyway for the synthesis of the hard carbon) and it avoids the use of reactive gas conditions (ammonia) used in previous studies for the preparation of VN-based materials.[110,111] Furthermore, a significant improvement in capacity is obtained upon incorporation of the VN on our hard carbon: with 8.6 *wt*% VN, the hard-carbon based composite electrode achieves a first cycle reversible capacity of 354 mA h g^{-1} at 50 mA g^{-1}, 16% higher than the bare hard-carbon electrode. The capacity retention of the VN-based composite with 8.6 *wt*% VN is also superior, with a reversible capacity of 294 mA h g^{-1} retained after 50 cycles. The additional capacity obtained by the incorporation of VN on the hard carbon is ascribed to the reversible conversion reaction of VN to $VN_{0.2}$ based on the XRD characterization of the electrodes after full discharge and charge in sodium half-cells.

5.2 Experimental

VN-HC composites were obtained by a variation to the synthesis process used for TiN-HC composites (section 4.2).[184] Under N_2, hexane (200 mL, Fisher Scientific, distilled from sodium/benzophenone ketyl ether) was added to a flask containing cotton wool (5 g, Fisher Scientific, dried overnight at 80 °C). $VOCl_3$ (volumes between 0 and 2 mL, Sigma-Aldrich) was added and the flask was heated to reflux (75 °C) overnight. The solvent and any remaining precursor was removed *in vacuo*. The dried material was then fired under nitrogen at 1400 °C (ramp rate 4 °C min^{-1} then maintained for 2 h).

5.3 Results and discussions

We have developed a strategy to make metal nitride-HC composites based on the reaction of hydrolysable metal-containing precursors with cellulose so that the hydroxide groups of the cellulose form M-O-C bonds to the metal. This distributes the metal ions across the surface, giving a uniform coating of the metal after a single pyrolysis step under nitrogen that is used anyway in the formation of HC itself (Fig. 1a). Previously we used $TiCl_4$ to distribute TiN nanoparticles onto HC.[184] VCl_4 has become difficult to obtain and has a limited shelf life, so here we used $VOCl_3$ as the reactive vanadium source.

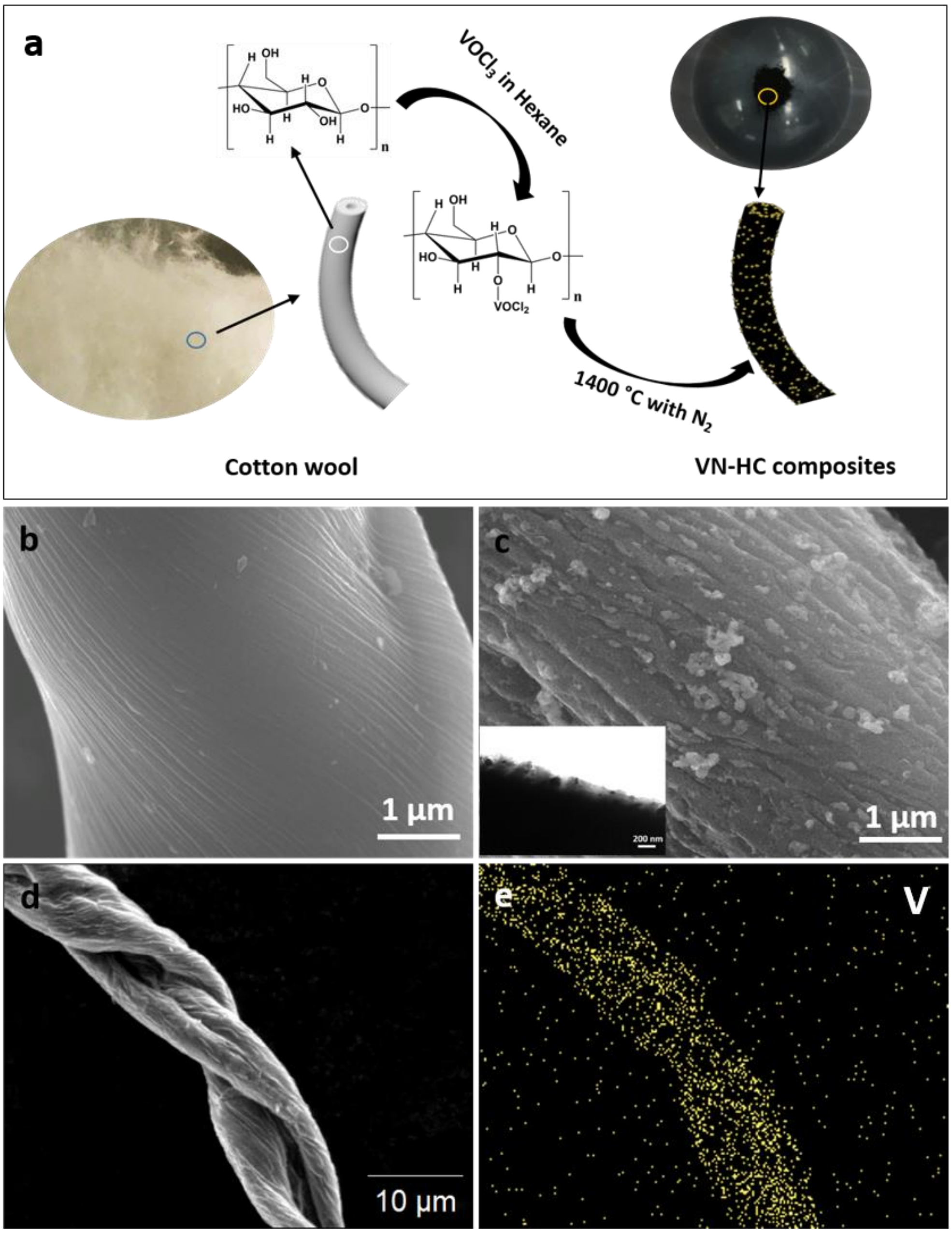

Figure 5-1 (a) Scheme illustrating the synthesis of the VN-HC composites; SEM image of (b) HC and (c) 8.6 wt% VN-HC composite, with inset TEM image; (d and e) EDX mapping image of the 8.6 wt% VN-HC composite. Further SEM images can be found in Fig. 5-2.

Table 5-1 Structural parameters for VN-HC composites

Samples	VOCl3 volume (mL)	HC		VN		
		d_{002} (Å)	I_D/I_G	crystallite size (nm)	a (Å)	BET surface area (m^2 g^{-1})
HC	0	3.747 (9)	1.71	-	-	69
4.6 *wt*% VN-HC	0.1	3.938 (5)	1.74	26 (2)	4.15304 (3)	45
6.5 *wt*% VN-HC	0.2	3.910(6)	1.75	35 (3)	4.15111 (3)	53
8.6 *wt*% VN-HC	0.4	3.960 (8)	1.82	39 (2)	4.15447 (6)	62
10.7 *wt*% VN-HC	0.8	3.923 (8)	1.86	46 (2)	4.15554 (2)	55
14.6 *wt*% VN-HC	2.0	3.966 (9)	1.90	56 (6)	4.16183 (1)	42

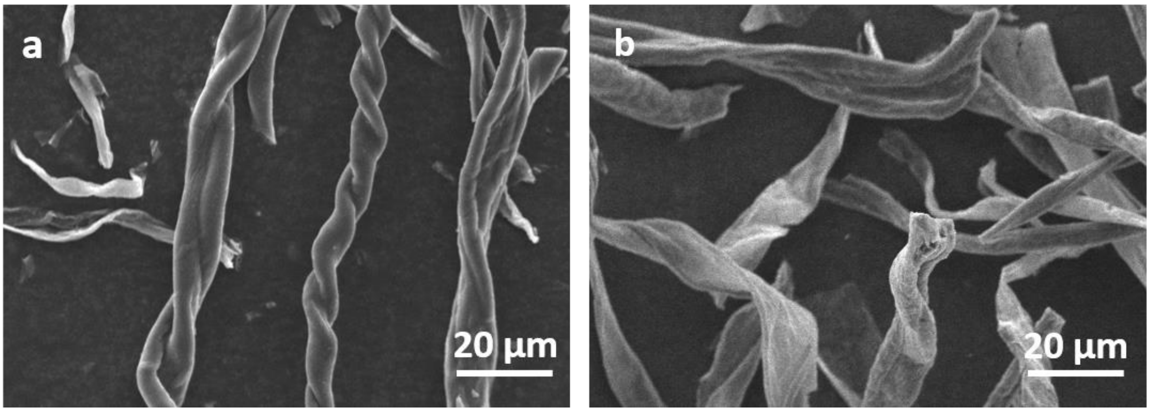

Figure 5-2 SEM images of (a) HC and (b) 8.6 *wt*% VN-HC composite.

Reaction of VOCl$_3$ with cotton wool produced a reddish brown material and the colour changed to green if exposed to air. After firing in N$_2$ at 1400 °C the fibrous, black carbon composite was ground to a fine powder. Various volumes of VOCl$_3$ were used in the synthesis to effect different loadings of VN on the HC (Table 5-1). SEM (Fig. 5-1b and Fig. 5-2a) shows the the fibrous structure of the HC with a diameter of 5-10 µm, maintaining the morphology that was originally present in the cellulose. The surface of the HC fibers are noticeably rougher in the vanadium-containing samples (Fig. 5-1c and Fig. 5-2b). TEM (Fig. 5-1c inset) shows that this roughness is due to the presence of nanoparticles on the HC surface. EDX maps (Figs. 5-1d and 5-1e) show that vanadium disperses evenly on the HC structure.

XRD patterns of the composites showed the expected rocksalt-type reflections of VN (PDF No. 35-0768) plus two broad peaks around 23 and 44 degrees that can be attributed to the 002 and 100 peaks of HC. The 200 peak of VN overlaps the 100 peak of HC, meaning that more structural information about the HC can be obtained by Raman (below). The VN peaks in the composites become narrower with increasing VN content, from which the particle size of VN was found to have increased from 26 nm at 4.6% loading to 56 nm at 14.6% (Table 5-1).

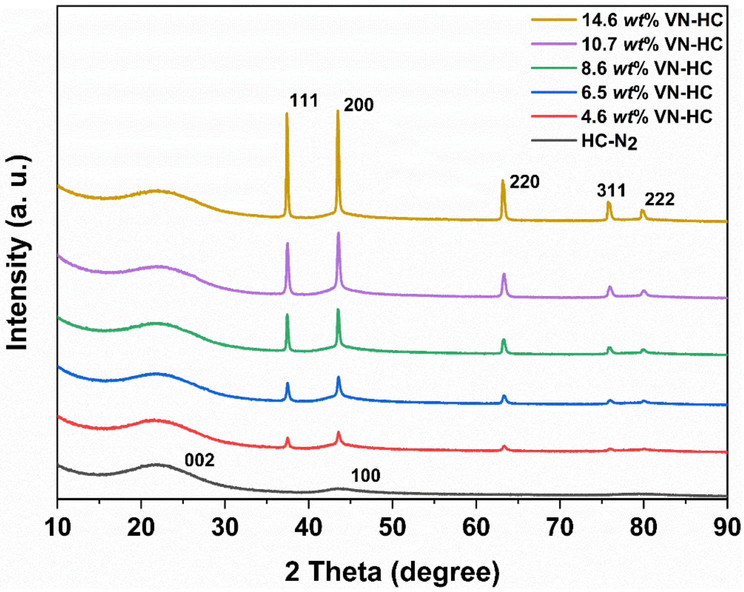

Figure 5-3 XRD patterns of HC and VN-HC composites with different VN loading.

Thermogravimetric analysis (Fig. 5-4) of the VN-HC composites was used to determine the VN content in the composite. The mass loss between 325 and 500 °C combined mass loss due to burning HC and mass increase due to oxidizing VN.

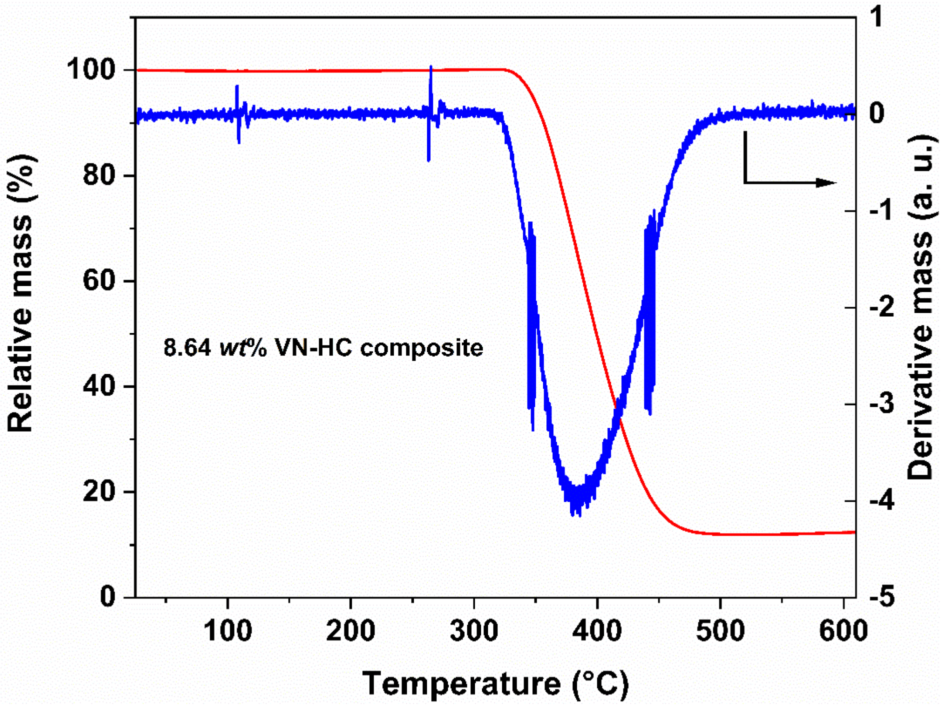

Figure 5-4 TGA and differential TGA results of 8.6 *wt*% VN-HC composite.

After TGA analysis, the remaining product was checked by PXRD and can be verified as V_2O_5 (Fig. 5-5).

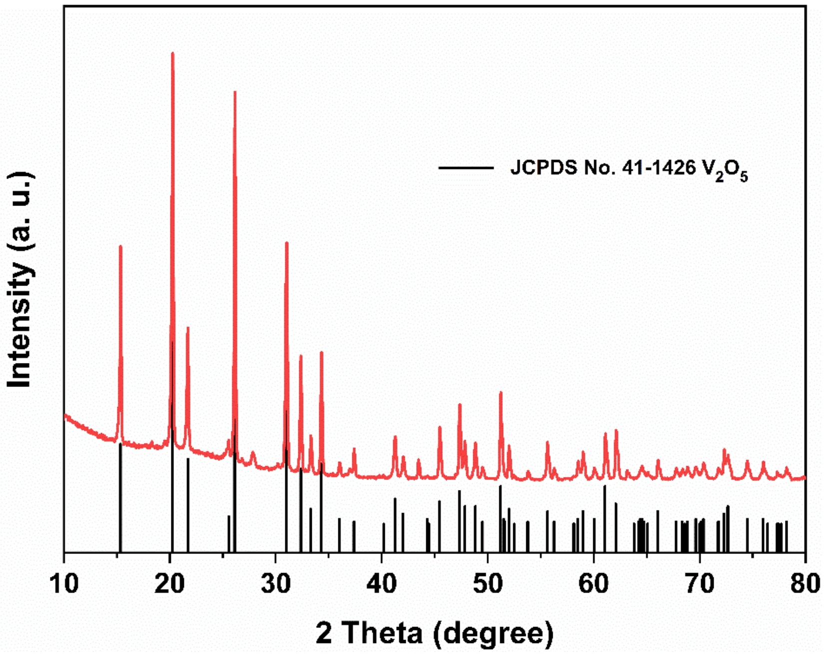

Figure 5-5 XRD pattern of V_2O_5 obtained from firing 8.6 *wt*% VN-HC composite during TGA measurement in oxygen.

Hence the vanadium content was calculated from this mass change.

$$aC + 2bVN + \frac{2a+5b}{2}O_2 = aCO_2 + bV_2O_5 \qquad \text{Equation 5-1}$$

mx 181.8mx/129.8

Assume the weight of composite is “m” gram, and the mass ratio of VN in composite is “x”. The calculated V_2O_5 should be 181.8mx/129.8 after heating at 610 °C. The weight remaining is 12.1% from thermogravimetric analysis. In that case, the value of x should be 0.08639.

Raman spectroscopy is useful to identify highly disordered materials, and as mentioned above the XRD peak overlap meant that Raman was more informative regarding the HC part of the composites (Fig. 5-6). Two broad peaks around 1310 and 1595 cm^{-1} can be ascribed to disordered (D-band) and ordered graphitic (G-band) structures in HC, respectively.[126] The spectral analysis by curve fitting employed the D, G and D_3 bands. The D and G bands were fitted with Lorentzian functions while a small D_3 band contributed with Gaussian function as described by others[185]. The intensity ratio I_D/I_G increases from 1.71 to 1.90 (Table 5-1) with increasing vanadium loading, suggesting the presence of VN increases the disorder of HC. That is consistent with previous reports of introducing metallic atoms to the amorphous substrate.[165] There are no obvious strong peaks below 1000 cm^{-1}, which would have been expected to be observed if significant vanadium oxide was present (Fig. 5-7).

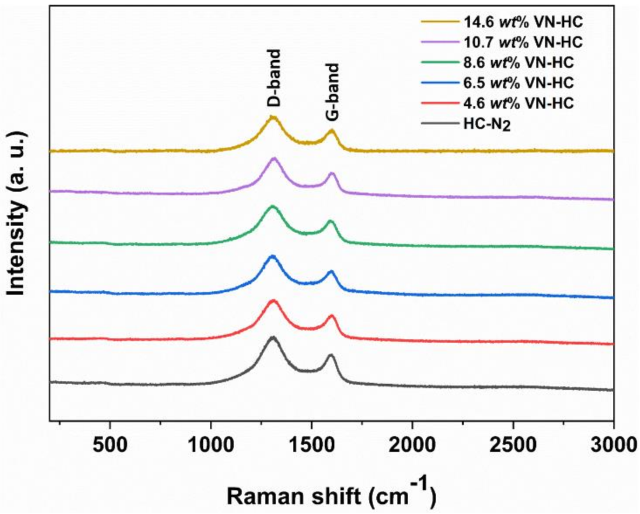

Figure 5-6 Raman spectra of VN-HC composites with different VN loadings.

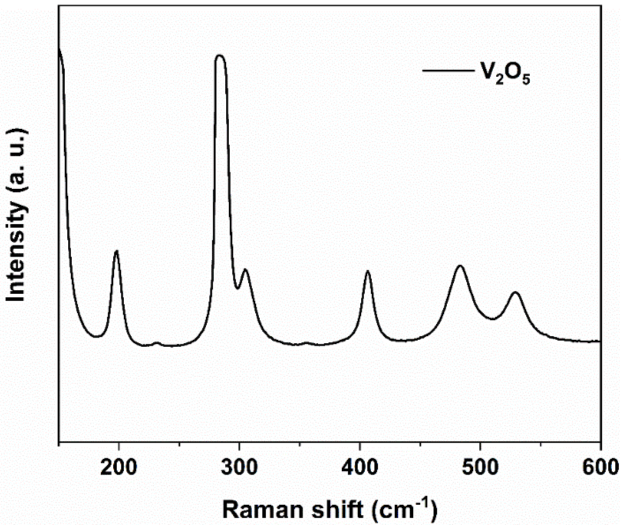

Figure 5-7 Raman spectrum of V_2O_5 obtained from firing 8.6 *wt*% VN-HC composite during TGA measurement in oxygen.

Fig. 5-8a displays the nitrogen adsorption-desorption isotherms of HC-VN composites. All the samples exhibit type IV isotherms and H4 type hysteresis, which means the samples contain micro-and mesopores. The pore size distribution (Fig. 5-8b) obtained by density functional theory (DFT) supports the presence of micro and mesopores. Table 5-1 shows the calculated BET surface area. As the volume of $VOCl_3$ used in synthesis increased from 0.1 to 0.4 mL, the surface area of the composites increased from 45 to 62 m^2 g^{-1}, suggesting the carbothermal reduction of the vanadium precursor and the formation of nanoparticles increased surface area. There is no evidence of pore blocking leading to reduced surface area. However, then, as the volume of $VOCl_3$ increased from 0.4 to 2 mL, the surface area decreased from 62 to 42 m^2 g^{-1}, which can be attributed to pore blocking and the increased particle size of VN.

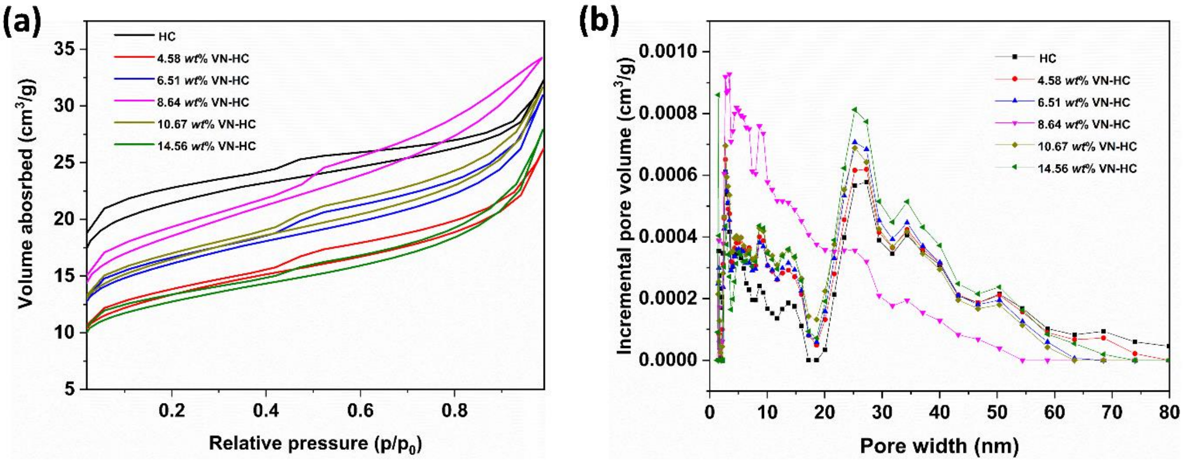

Figure 5-8 (a) Nitrogen adsorption-desorption isotherms of HC-N_2 and HC-VN composites; (b) pore size distribution calculated by using DFT method.

The surface composition of 8.6 *wt*% VN-HC was probed using XPS. The measured atom concentrations in the top few nm of the sample were C 93.4%, N 1.3%, O 2.9% and V 2.4 %,. The high resolution C 1s spectrum and survey spectrum can be seen in Fig. 5-9. The main C 1s peak at 284.6 eV is compatible with the binding energy from sp^2 carbon, while the peaks with higher binding energy can be attributed to sp^3 carbon, C-O, C=O and π-π*satellite.[144,167]

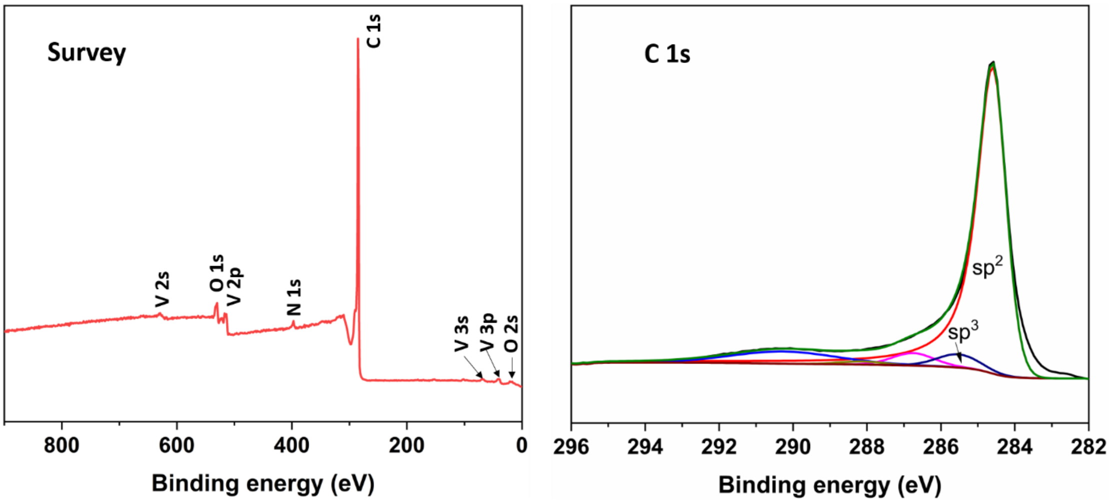

Figure 5-9 XPS survey and C 1s spectrum of 8.6 *wt*% VN-HC composite.

The strong peak in the N 1s region at 397.3 eV (Fig. 5-10a) corresponds to N in vanadium nitride,[186] with oxynitride and surface-bound nitrogen species also observed at higher binding energies.[187] The main component in the O 1s spectrum (Fig. 5-10b) with binding energy of 530.1 eV corresponds to vanadium oxide,[186] while another two peaks with binding energy of 531.2 eV and 532.9 eV can be assigned to absorbed carbonyl groups on the hard carbon,[188,189] which is consistent with the components in the C 1s region. As the vanadium oxide does not appear in the XRD pattern or Raman spectra, the content is small and can be attributed to air exposure of the surface.[111,190] For the $V2p_{3/2}$ components, peak position at 513.7 eV is corresponding to VN and binding energy at 516.8 eV is attributed to shake-up satellite originating from poorly screened core hole states[191,192], while the signal at 515.4 eV and 517.4 eV are related to oxidation state higher than 3^+.[111,193] In our previous study,[184] we discussed the absence of nitrogen doping in hard carbon and the spectrum fitting here is good without the presence of C-N at 286.2 eV in C 1s,[194] suggesting no obvious evidence of nitrogen doping of the HC component.

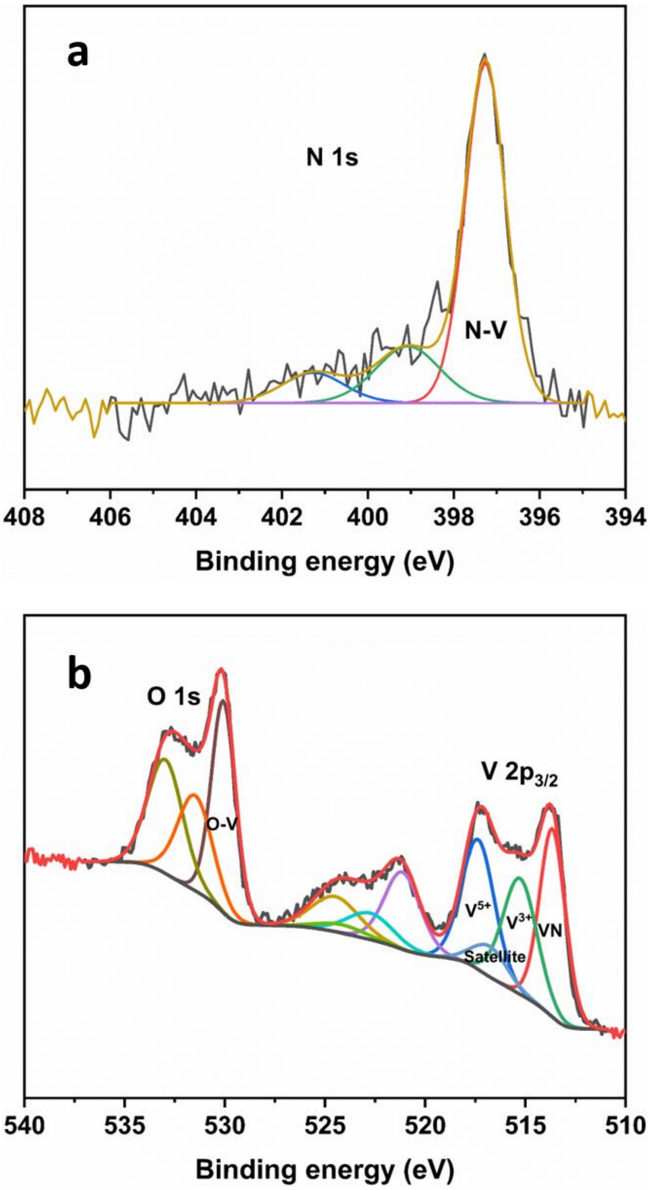

Figure 5-10 Fitted N 1s (a), and O 1s and V 2p (b) XPS spectra of 8.6 *wt*% HC-VN composite.

The electrochemical performance of the VN-HC composites was evaluated in sodium half cells by charge/discharge cycling over the voltage range 0.005-2 V (vs the sodium counter electrode). Fig. 5-11 shows the first cyclic differential capacity plots of HC and the VN-HC composite electrodes. The first pair of small cathodic peaks at around 1.07 V and 0.52 V (insert in Fig. 5-11) can be assigned to the decomposition of electrolyte and formation of a solid electrolyte interface (SEI) and irreversible adsorption/insertion of sodium on the hard carbon.[195]

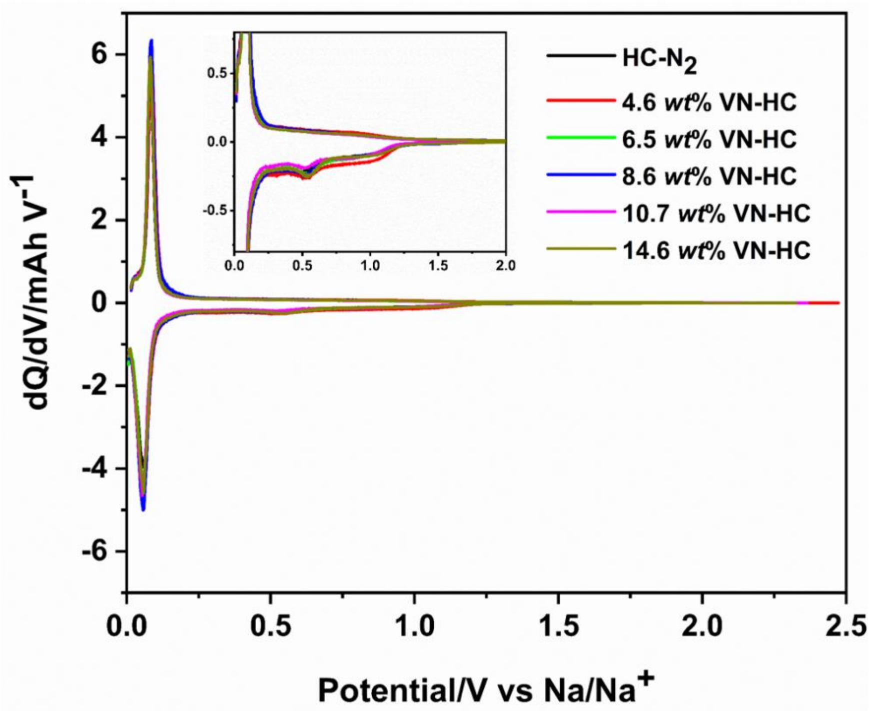

Figure 5-11 The first cyclic differential capacity plots of VN-HC composites with different VN content at current of 50 mA g^{-1}.

These processes only appear in the first cycle (see Fig. 5-12). The main process of sodium insertion and extraction from the hard carbon produces a sharp peak centered at ca, 0.1 V versus Na$^+$/Na, in agreement with previous work.[50] The height of this main peak changes little with cycling, demonstrating good cyclability of the VN-HC composite electrodes. Previous research reported that the sodiation/desodiation of VN shows a pseudocapacitive behavior without distinct redox peaks apart from a gradually increased cathode current towards 0 V.[107] The potential range is close to that of the main feature peaks of HC thus the peaks correspond to sodiation/desodiation of VN is not clear seen in the differential capacity plots.

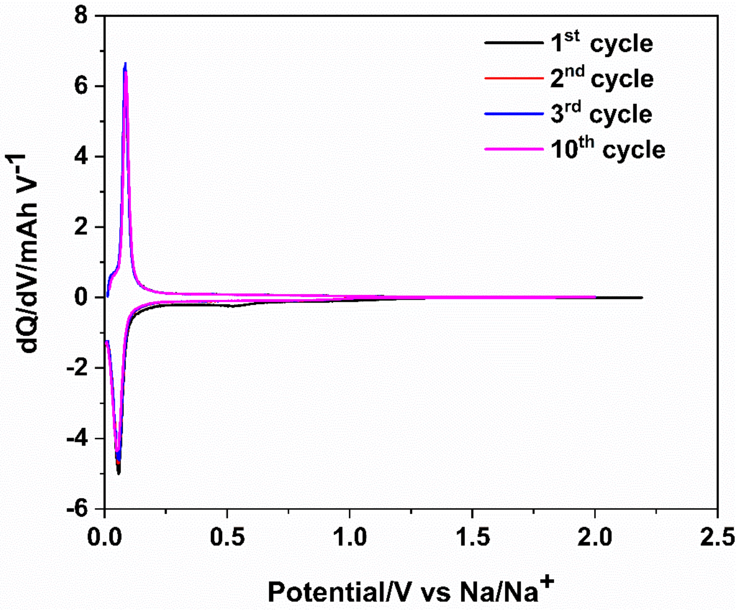

Figure 5-12 Differential capacity plots of 8.6 *wt*% VN-HC electrode at 50 mA g^{-1} in first 10 cycles.

Fig. 5-13 shows the first charge/discharge profiles of HC and VN-HC electrodes at a current of 50 mA g^{-1}. The HC electrode exhibited an initial reduction (sodiation) specific capacity of 433 mA h g^{-1} and an oxidation (reversible, desodiation) specific capacity of 302 mA h g^{-1}, with a 70% first cycle coulombic efficiency. Similar performance has been reported for hard carbon obtained from cotton wool (by heating at 1300 °C), which delivered an oxidation (reversible) capacity of 315 mA h g^{-1} at 30 mA g^{-1} with first cycle coulombic efficiency of 83%.[69] The lower first cycle coulombic efficiency obtained here can be ascribed to the higher BET surface area (69 m^2 g^{-1}, compared to 38 m^2 g^{-1} in previous work[69]). The use of PVDF binder has also been reported to decrease the coulombic efficiency[196], and further work will investigate the use of alternative binders such as sodium alginate, used in previous work.[69]

On the other hand, the VN-HC electrodes showed oxidation (reversible, de-sodiation) capacities of 317, 333, 354, 306 and 284 mA h g^{-1}, with increasing VN content. Therefore, an increase of 52 mA h g^{-1} in the oxidation (reversible) capacity is achieved upon incorporation of 8.6 wt% VN on HC. This increase of 52 mA h g^{-1} in specific capacity (normalized by the mass of the whole active material, VN and hard carbon) corresponds to a very high specific capacity of 605 mA h g^{-1} when normalized by the mass of VN in the VN-HC composite. Since VN is the source of this extra capacity, normalization by the mass of VN in the composite electrode provides a more accurate measure of the degree of utilization of VN in the VN-HC composite in the energy storage reactions, and the value of capacity of 605 mA h g^{-1} is the highest specific capacity of VN in sodium ion batteries that has been reported. The specific capacity of the VN-HC composite electrode with 8.6 %wt VN of 354 mA h g^{-1} also exceeds or is comparable with the capacity of VN-based materials used previously in sodium-ion batteries, [107,110,111,183] whereas the material here developed has clear advantages in terms of the low content of VN (which is the most expensive component), use of very cheap carbon precursors (cotton wool) and use of an environmentally friendly and easily scalable synthesis route.

The maximum capacities are not achieved with maximum addition of VN into the hard carbon. The maximum in the BET surface area of the composites peaks at 8.6 wt% VN-HC (Table 5-1), the composition that also exhibits the highest sodium storage capacity. This suggests that surface area is important, although charge storage is not purely a surface area related effect since surface area is lower in all of the composites than that of the hard carbon itself. Calculated VN surface area based on the loadings and crystallite sizes shown in Table 5-1 would suggest that the VN surface area should increase with increasing VN content – the fact that it does not is likely to be due to a larger degree of VN aggregation at the higher loadings.

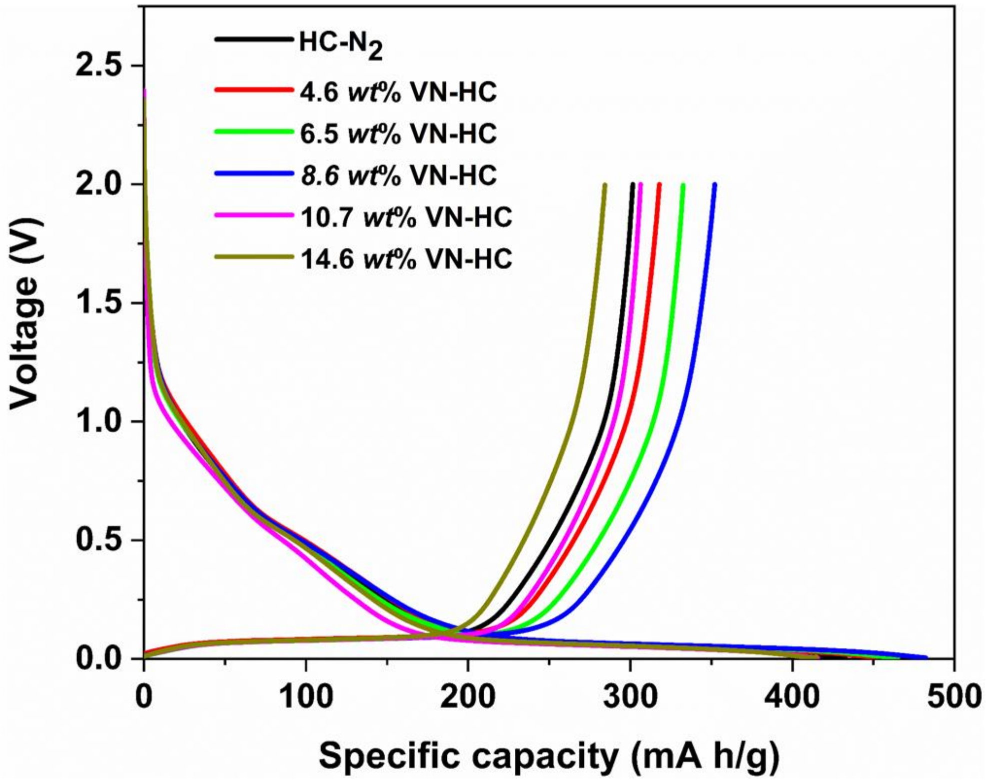

Figure 5-13 First cyclic charge-discharge capacity curves of VN-HC composites with different VN content.

In order to understand the energy storage reactions undergone by VN in the VN-HC composites, and elucidate the origin of the increase in capacity observed upon addition of VN to the hard carbon material, an *ex situ* XRD characterization of the electrodes before and after cycling was done (Fig. 5-14). The pristine electrode, prior to cycling, showed peaks attributed to vanadium nitride and the copper substrate. After the first electrochemical reduction (sodiation) to 0.005 V, a new peak at 54.1 degrees appeared, which can be ascribed to $VN_{0.2}$[197], and the VN peaks decreased in intensity. The fact that VN peaks are observed for the fully sodiated electrodes suggests that the cores of the VN particles remain unreacted.

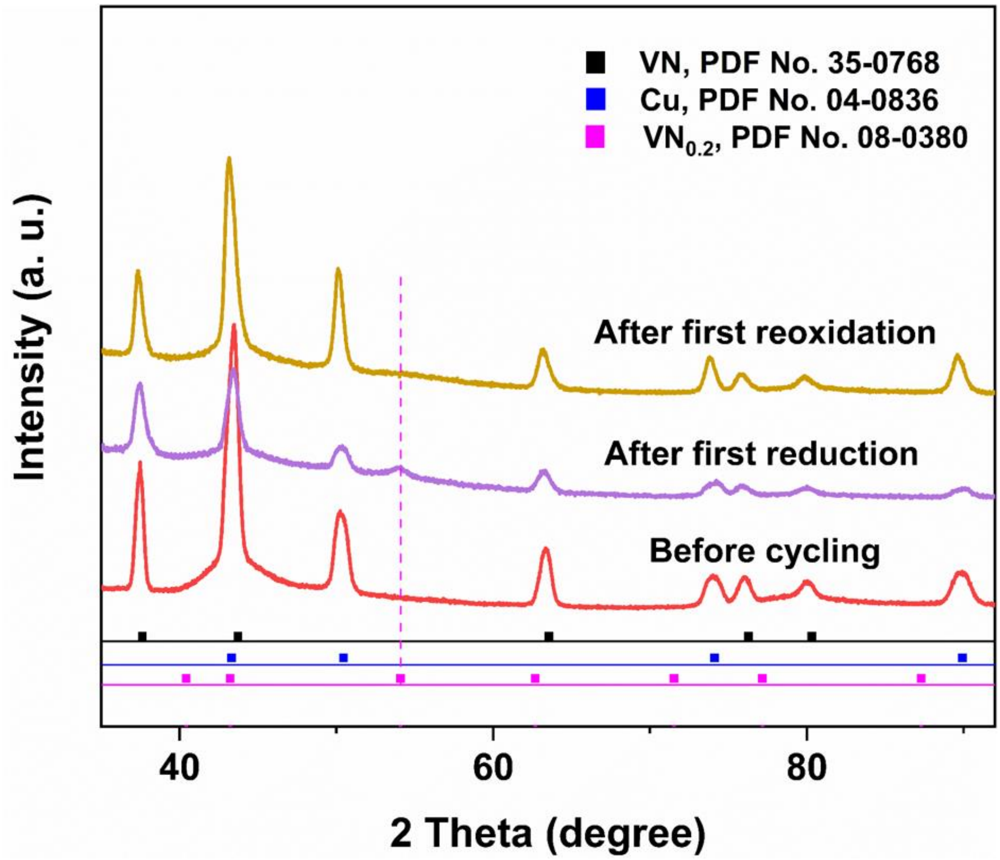

Figure 5-14 Ex-situ XRD patterns of 8.6 wt% VN-HC electrode before and after first cycling.

Rietveld refinement of the XRD data (Fig. 5-15, Table 5-2) showed that the lattice parameter of VN in the reduced and oxidized samples was the same, confirming that the sodiation reactions occur on the surface of the VN nanoparticles. From the BET data described above we know that the surface area decreases above 8.6 wt% VN and this change is likely to be responsible for the declining capacity at higher loadings. Other products of the electrochemical sodiation of VN (e.g. sodium nitride) appear to be amorphous, since they could not be detected by XRD. After the electrochemical oxidation (de-sodiation) of the sample to 2 V, the new peak associated with $VN_{0.2}$ disappears and the VN reflections increase in intensity, becoming close to that in the original pattern, demonstrating that VN energy storage reactions are reversible.

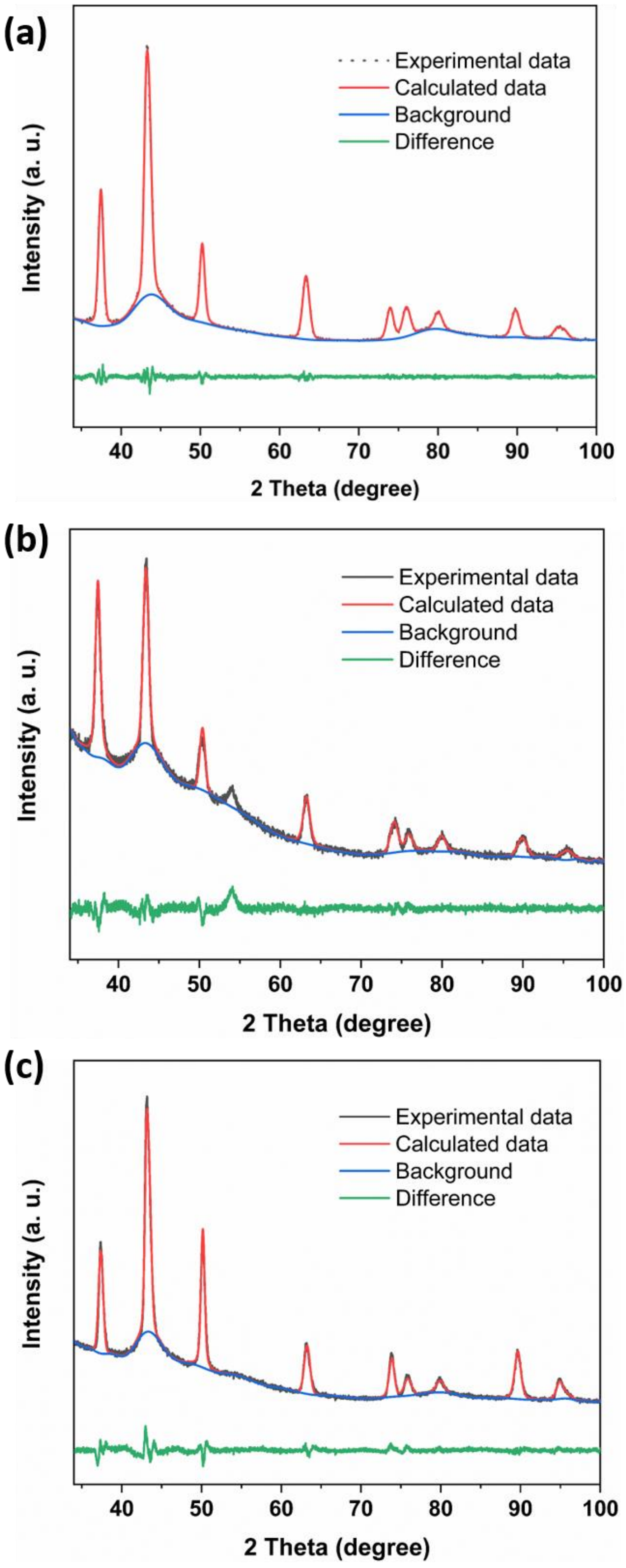

Figure 5-15 Rietveld fits to ex-situ XRD data of 8.6 *wt*% VN-HC electrode (a) before cycling (b) after first reduction (c) after first reoxidation by GSAS package.

Table 5-2 Lattice parameters of VN in the composites at different cycling stage

Galvanostatic cycling stage at which sample was removed from cell	VN		
	Lattice parameter (Å)	R_{wp} (%)	R_p (%)
Before cycling	4.14463 (18)	3.1	2.4
After first reduction	4.15533 (21)	3.5	2.6
After first reoxidation	4.14929 (24)	3.0	2.3

Fig. 5-16 shows the cycling performance of HC and VN-HC electrodes at 50 mA g^{-1} in 50 cycles. The 8.6 *wt*% VN-HC electrode exhibited an initial coulombic efficiency of 73%, higher than that of 70% from HC, and reached over 98% before the 10th cycle. The VN-HC electrodes showed initial coulombic efficiency of 69%, 72%, 73%, 74% and 69% with increasing VN loading. After 50 cycles, the oxidation (reversible) capacity of the 8.6 *wt*% VN-HC electrode was 294 mA h g^{-1}, retaining 83% of its first cycle capacity (a repeat data set is in Fig. S8), while that of the HC electrode decreased to 239 mA h g^{-1}. Therefore, the difference in capacity of the VN-HC electrode with 8.6%wt VN and the HC electrode is 55 mA g^{-1}, very close to the initial difference in capacity of 52 mA h g^{-1}.

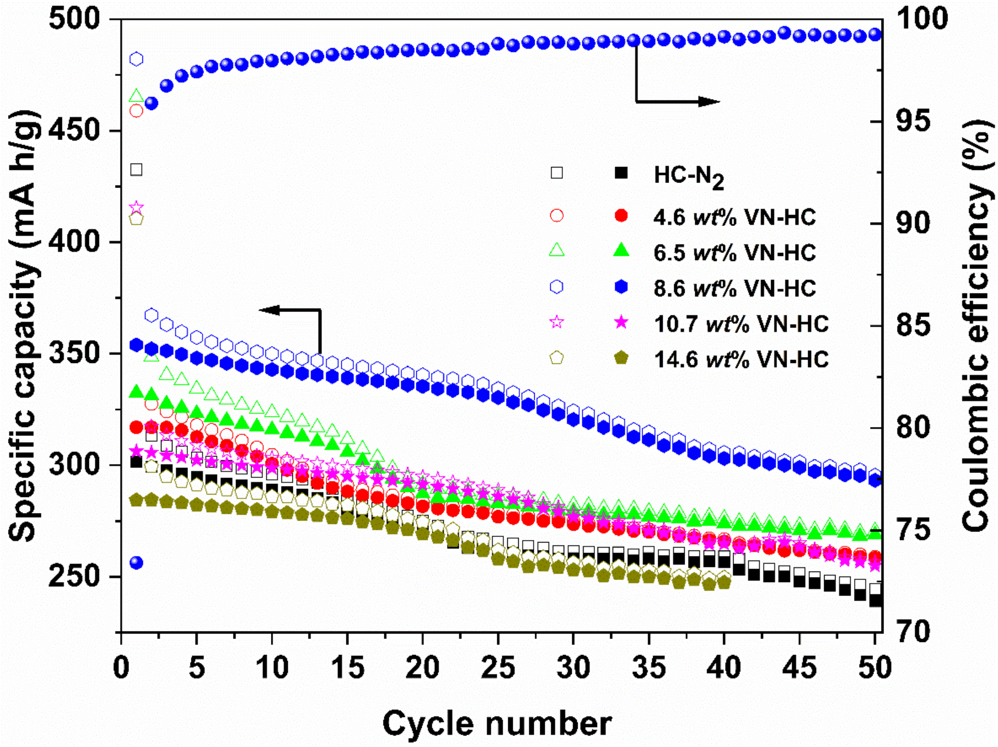

Figure 5-16 Cyclic performance of HC and VN-HC composites electrodes.

Fig. 5-17 shows the electrochemical impedance spectra for the HC and VN-HC before cycling (inset in Fig. 5-17) and after 50 cycles. Electrochemical impedance spectroscopy (EIS) was measured at room temperature with a frequency range from 0.05 Hz to 500 kHz, and the voltage before cycling is around 2.9 V and after cycling is around 1.0 V. It is observed that the HC electrodes show a larger increase in their charge transfer resistance with cycling: the semicircle in the Nyquist plot has a width of ca. 147 Ω in the VN-HC composite compared with ca. 277 Ω in the HC electrode after 50 cycles (values obtained by fitting the data to the equivalent circuit shown in Fig. 5-17). The lower charge transfer resistance of the VN-HC composites, compared to pure HC, could be due to the contribution of the energy storage reaction on VN nanoparticles, in agreement with the fact that the measured specific capacity is higher.

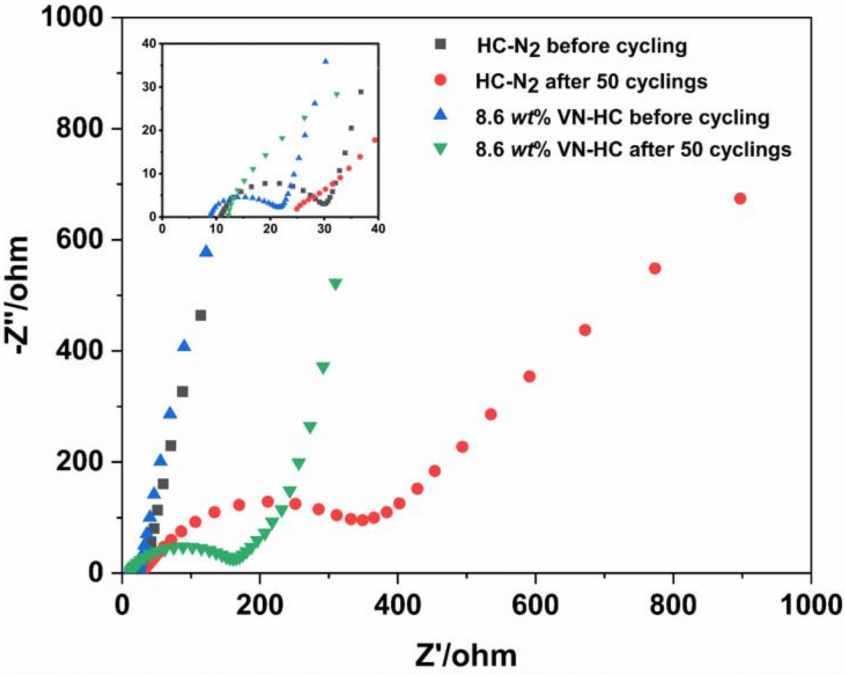

Figure 5-17 Nyquist plots of HC and 8.6 *wt*% VN-HC composite electrodes before and after 50 cycles.

On the other hand, the rate of decrease of specific capacity with cycling is similar for VN-HC and HC electrodes, which suggests that the cause of capacity fade is the same in both cases. A recent study has shown that the capacity of cycled hard carbon electrodes in sodium half cells can be quantitatively recovered (95% of the original capacity) by replacing the electrolyte, separator and sodium metal counter electrode in the cell, indicating that the main cause of capacity degradation is due to the reactivity of the sodium metal counter electrode with the electrolyte, rather than degradation of the hard carbon.[196] This is supported by the fact that the capacity loss only affects the electrochemical reactions taking place at potentials <0.1 V, and the fact that the capacity loss in this low potential region is more severe at a higher current density (Figs. 5-18).

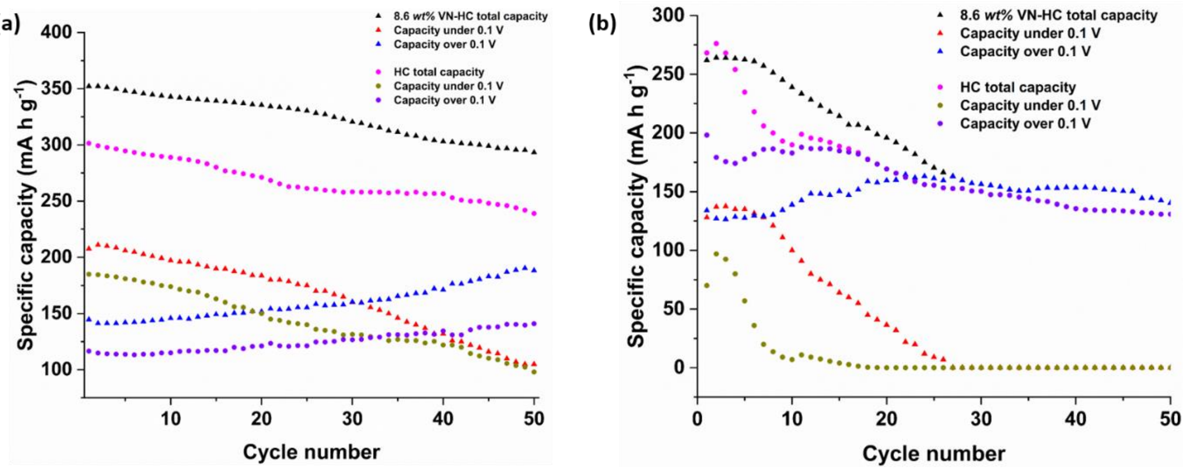

Figure 5-18 Analysis of the total capacity and capacity contributions under and over 0.1 V for pure hard carbon and 8.6 *wt*% VN-HC. Specific current is (a) 50 mA/g and (b) 200 mA/g.

This behavior is consistent to that reported previously by Bommier *et al*,[196] who explained it as reaction of the sodium counter electrode with the electrolyte, forming an SEI whose resistance increases with time. Since the measurements here reported were done in 2-electrode sodium half-cells, with sodium as both the reference and counter electrode, the increasing resistance of the sodium SEI means that the potentials applied to the hard carbon electrode during the sodiation reactions become higher with cycling. The lower voltage limit of 5 mV vs. the sodium counter electrode increasingly becomes higher than a potential limit of 5 mV vs. a Na^+/Na reference electrode, because the IR drop contribution becomes increasingly higher. Due to the very shallow voltage profile of the HC and VN-HC electrodes at low potentials (Figs. 5-19 and 5-20), the increase in the low potential limit value due to the increase in IR drop contributions produces a significant effect on the measured capacity, but this does not appear to be related to degradation of the HC or VN-HC electrode.

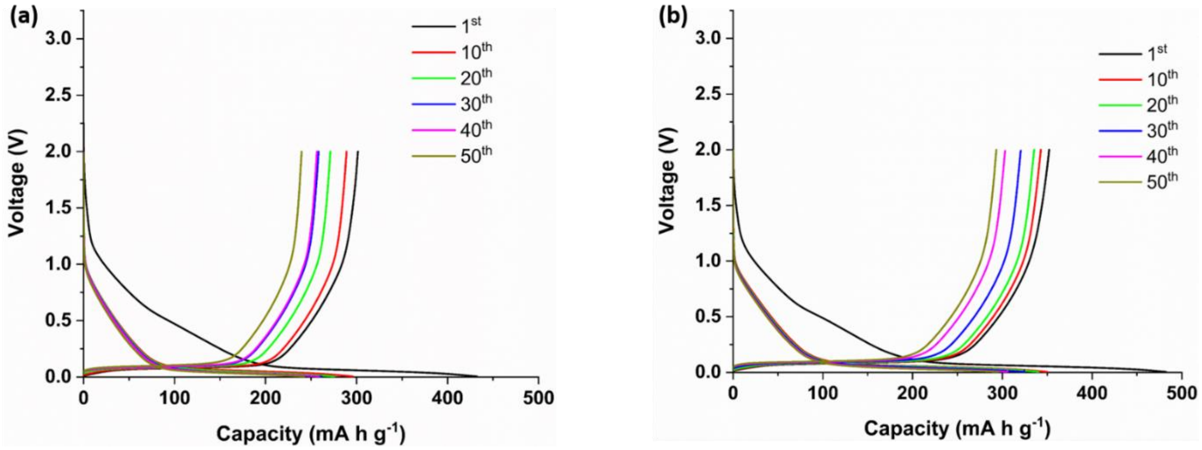

Figure 5-19 Evolution of charge-discharge voltage profile of (a) pure hard carbon and (b) 8.6 *wt*% VN-HC. Specific current: 50 mA/g.

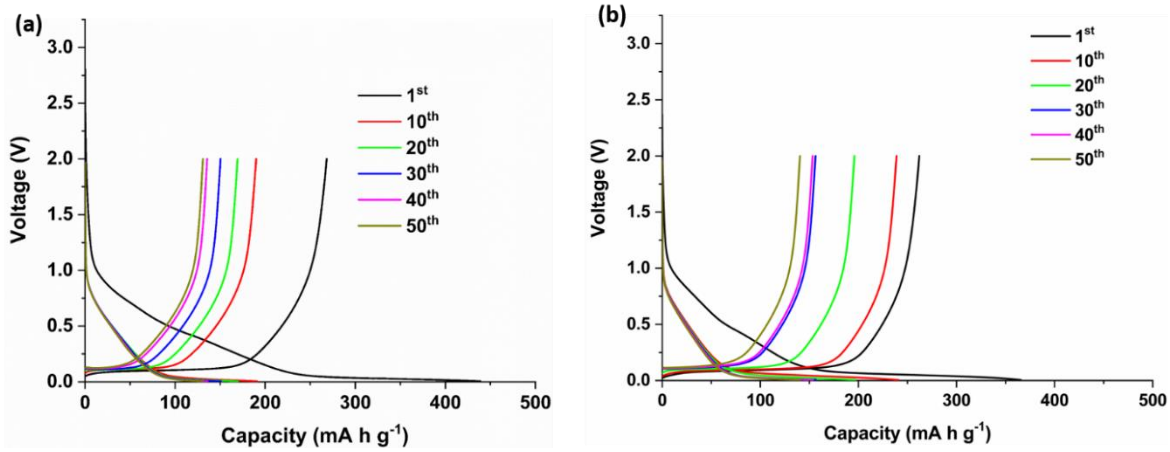

Figure 5-20 Evolution of charge-discharge voltage profile of (a) pure hard carbon and (b) 8.6 *wt*% VN-HC. Specific current: 200 mA/g.

5.4 Conclusions

VN-HC composites have been synthesized using a pyrolysis process after reacting $VOCl_3$ with cellulose. The samples contained hard carbon with a morphology that emulates the fibrous structure of the cellulose precursor, with vanadium nitride nanoparticles distributed across the surfaces. The addition of 8.6 *wt*% VN to the hard carbon showed the best electrochemical performance, with initial reversible (oxidation) capacity of 354 mA h g^{-1} (52 mA h g^{-1} higher than the capacity of pure hard carbon). The additional capacity delivered by VN-HC composites, compared to pure HC, is maintained during cycling, consistent with the conclusion from previous studies that the degradation of capacity with cycling is due to the reactivity of the sodium metal counter-electrode with the electrolyte, rather than degradation of the electrode material.[196] When the additional capacity associated with addition of VN is normalised by the mass of VN only (rather than the sum of the masses of VN and hard carbon), a very high value of specific capacity of ca. 605 mA h g^{-1} is obtained, demonstrating good utilisation of the VN in sodiation conversion reactions. The XRD characterization of the electrodes after the first reduction (sodiation) shows the transformation of VN to $VN_{0.2}$ and other amorphous phases, and back again to VN after the first oxidation (de-sodiation). XRD also shows that the core of the VN nanoparticles remain unreacted, thus further decreasing of nanoparticle size could lead to improved performance. Other strategies for optimisation of the material could include the use of soft carbons combined with the hard carbon to improve the initial coulombic efficiency,[198] which will be the subject of further work. Overall, the new material reported here shows promising electrochemical performance and a reaction mechanism in which the advantages of HC and VN for applications in SIB are combined to produce a material with high structural stability. We expect that this facile and effective method can be extended to synthesize other metal nitride/carbon composites to apply in electrocatalysis, supercapacitors and other energy technology.

6. Amorphous silicon nitride or silicon oxycarbide coated on hard carbon for sodium ion batteries

6.1 Introduction

Stoichiometric silicon nitride (Si_3N_4) with low electrical conductivity was regarded as an inactive material in lithium ion batteries (LIBs),[199] albeit with a reported low capacity (40 mA h g^{-1}) reported when the particle size of Si_3N_4 was reduced. On the other hand, non-stoichiometric silicon nitride ($SiN_{0.92}$[200], $SiN_{0.89}$ and $SiN_{0.83}$[201]) show high capacities with conversion reaction in LIBs. In these works, silicon nitrides are assumed to be converted to conductive silicon with formation of inactive nitride components such as Si_3N_4, Li_3N and Li_2SiN_2. However, to our best knowledge, silicon nitride has not been reported as an anode material in SIBs.

Silicon oxycarbides (SiOCs) have been widely reported as anode material in LIBs in recent years. SiOCs are composed of free carbon phase (C_{free}) and SiO_4hase, in which it is considered that oxygen is partly substituted by carbon in silica. In the case of sodium, quite a few SiOCs have been investigated as anode materials in SIBs. In 2015, Weinberger et al. first reported silicon oxycarbide spheres for sodium ion batteries. The SiOC spheres deliver reversible capacity of 200 mA h g^{-1} at current of 25 mA g^{-1}, with initial Coloumbic efficiency of 47%.[202] Chandra et al. produced silicon oxycarbides by simple pyrolysis of low-cost silicone oil at different temperature in a H_2/Ar flow condition. The SiOCs sample obtained at 900 °C contained a large amount of amorphous free carbon species, displaying a reversible capacity of 160 mA h g^{-1} at 25 mA g^{-1} after 200 cycles in SIBs.[203]

To obtain an understanding of the sodium storage mechanism in SiOCs, Dou et al.[204] and Chandra et al.[205] applied *ex situ* characterization methods. The XPS and ^{29}Si MAS NMR measurements of electrodes cycled to different potential suggested the presence of reversible redox activity of Si but not the SiOC, and reversible insertion/deinsertion of sodium into amorphous SiOCs during cycling.[204] Chandra et al. ascribed the sodium storage in SiOCs to three mechanisms at different voltages.[205] First, in the slope region down to 0.4 V, sodium insertion mainly happens in C-rich SiO_4 phase and micropores. Second, in the slope region between 0.4-0.1 V, insertion of sodium is found in O-rich SiO_4 phases. Finally, in the low voltage plateau below 0.1 V, sodium continues to be inserted in the SiO_4 phases and also reacts with amorphous Si to form Na-rich Si compounds. Although only a few works above reported the SiOCs in the application of SIBs, the plateau region below 0.1 V and good capacity performance make SiOCs a promising anode alternative in SIBs.

Here we report on a synthesis of amorphous silicon nitride or silicon oxycarbides supported on hard carbon and their application in sodium ion batteries. The physical properties of silicon nitride or silicon oxycarbide samples have been investigated by XRD, Raman and XPS measurement. While the silicon oxycarbide-hard carbon composites show similar capacity to pure hard carbon, the silicon nitride-hard carbon composites show a reversible capacity of 351 mA h g^{-1} at 50 mA g^{-1}, better than that of 284 mA h g^{-1} from pure hard carbon.

6.2 Experimental

Hard carbon composites with silicon nitride and silicon oxycarbide were obtained by a variation to the synthesis process in section 4.2. Dry hexane (200 mL, Fisher Scientific, distilled from sodium/benzophenone ketyl ether) was added to a flask containing cotton wool (5 g, Fisher Scientific, dried overnight at 80 °C). $SiCl_4$ (volumes between 0 and 0.8 mL, Sigma-Aldrich) was added and the flask was heated to reflux (75 °C) overnight. The solvent and any remaining precursor was removed *in vacuo*. The dried material was then fired under argon or nitrogen at 1200 °C and 1400 °C (ramp rate 4 °C min^{-1} then maintained for 2 h).

6.3 Results and discussions

Previously we reacted titanium chloride or vanadium oxytrichloride with hydroxide groups from cellulose before firing cellulose to make hard carbon composites. The temperature was 1400 °C as that was the optimised temperature to get the best capacity from hard carbon. Fig. 6-1 shows the XRD patterns of composites with silicon nitride and silicon carbides by reacting with different volume of silicon chloride at 1400 °C under nitrogen or argon (respectively). The intensities of sharp peaks corresponding to silicon nitride (Fig. 6-1a) or silicon carbide (Fig. 6-1b) increase with adding more volume of silicon chloride. The narrower peak width indicates more crystalline structure by introducing more silicon nitride or silicon carbide. Samples from pyrolysis with nitrogen or argon were labelled as HC-Si_3N_4-v and HC-SiC-v composites, respectively, where “v” represents the volume of $SiCl_4$ used in the synthesis process.

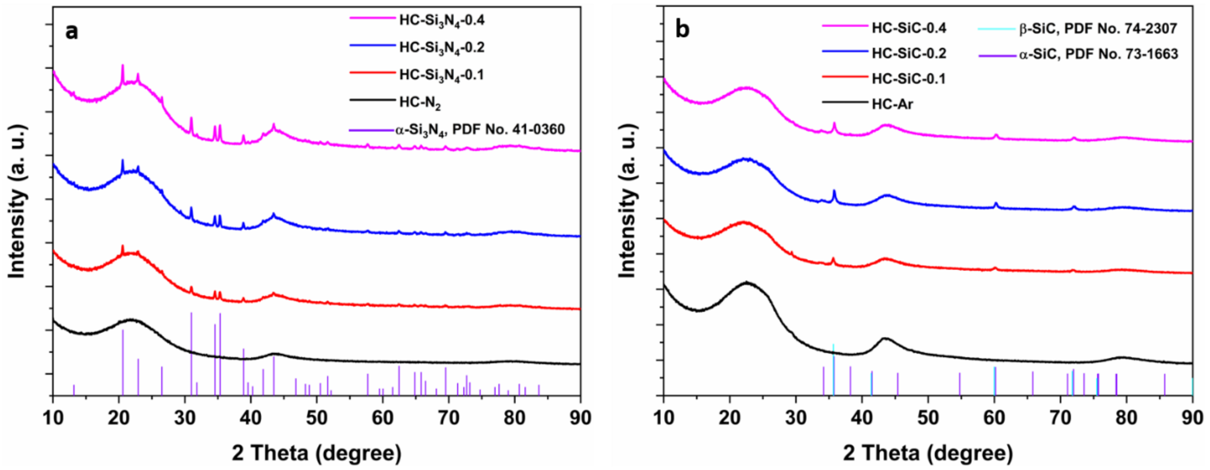

Figure 6-1 XRD patterns of composites with (a) silicon nitride and (b) silicon carbide produced by reacting cellulose with different volumes of silicon chloride and firing under nitrogen or argon at 1400 °C.

The composites with different content of silicon nitride or silicon carbide were prepared as ink and then made as the working electrodes. The electrochemical performance was investigated by galvanostatic cycling with potential limitation (GCPL). The HC-Si_3N_4 electrodes showed oxidation capacities of 292, 303 and 289 mA h g^{-1} with increasing content of silicon nitride. For the HC-SiC electrodes, the oxidation capacities are 289, 262 and 243 mA h g^{-1} with increasing content SiC. The presence of crystalline silicon nitride and silicon carbide increases the capacity with low silicon content and then decreases capacity with more content, a pattern similar to that seen in the titanium and vanadium systems.

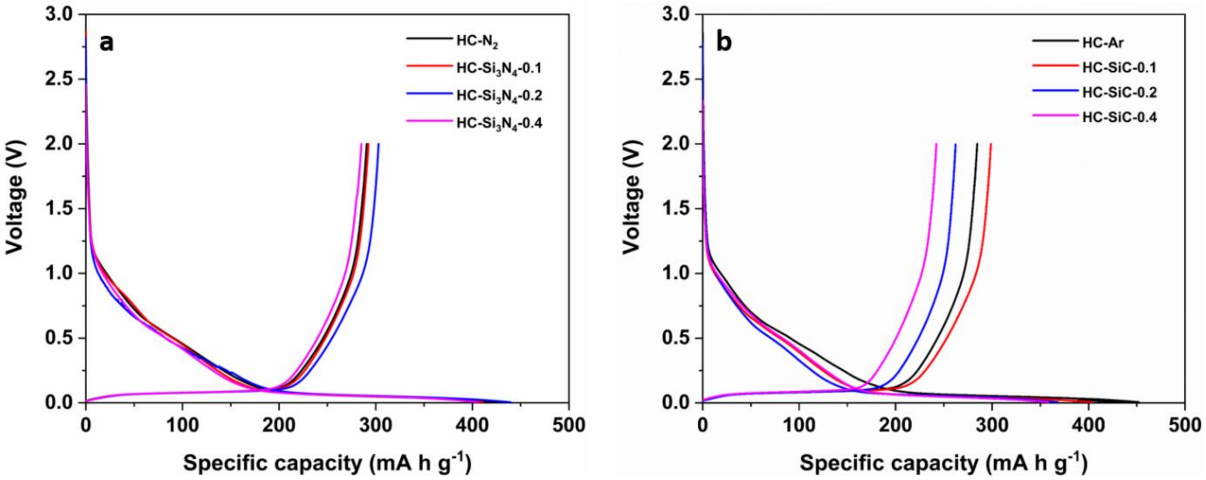

Figure 6-2 First cycle charge-discharge capacity curves of composites with (a) silicon nitride and (b) silicon carbide produced by reacting cellulose with different volumes of silicon chloride and firing under nitrogen or argon at 1400 °C.

As more silicon was added to the composites fired at 1400 °s it was clear that crystallite sizes were increasing and that might reduce the accessibility of the material for sodium storage reactions. Previous work had shown that reducing the temperature to 1200 °C in the silicon nitride system results in amorphous material.[206] Firing the cellulose-based precursors to hard carbon at this temperature resulted in composites with amorphous silicon nitride or amorphous silicon oxycarbide. These products pyrolysis with nitrogen were labelled as HC-SiN_x-v ($0<x<1.33$) and pyrolysis with argon were labelled as HC-SiOC-v composites, respectively, where “v” represents the volume of $SiCl_4$ used in the synthesis process.

Fig. 6-3a and d show TEM images of the HC-SiN_x-0.4 and HC-SiOC-0.4 composites. It can be seen that nanoparticles with no obvious sign of crystallinity are dispersed on the carbon substrate. EDX mapping (Fig. 6-3c and f) results corresponding to SEM images (Fig. 6-3b and e) indicate that silicon was uniformly distributed onto the hard carbon substrate, with some larger particles also visible on the surface of the fibres.

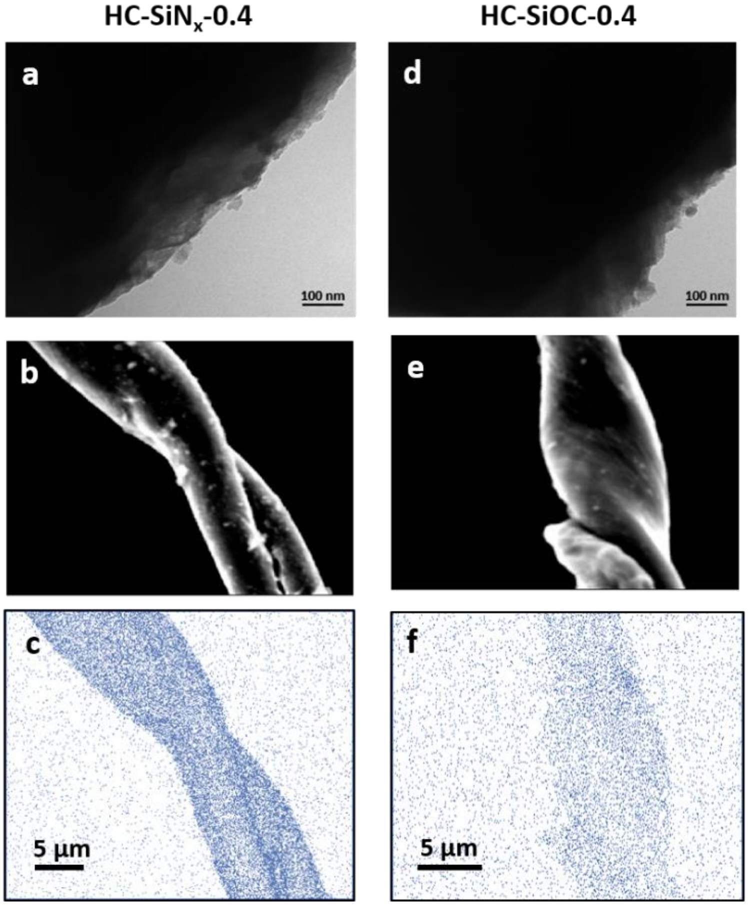

Figure 6-3 TEM, SEM and EDX images of the (a-c) HC-SiN$_x$-0.4 and (b) HC-SiOC-0.4 composites. Blue dots in the EDX mapping represent the location of the silicon signal and the scale bars in the EDX maps also apply to the SEM images.

Phase compositions were investigated by XRD. No peaks were absorbed in the nitrogen-fired materials other than the usual two broad peaks from hard carbon (Fig. 6-4a), indicating the silicon-containing component to be amorphous. Table 6-1 shows the interlayer distance from hard carbon. The d_{002} is basically unchanged after introducing the amorphous silicon content. Fig. 6-4b shows the XRD patterns of hard carbon coated with silicon oxycarbide. In this case, in addition to the two broad peaks from hard carbon, a small peak corresponding to 3C cubic silicon carbide (PDF No. 74-2307) appears around 35.7°. The crystalline phase in silicon carbide can be ascribed to the different behaviours of silicon nitride and silicon carbide. Previous researchers reported that the amorphous-crystalline transition temperature of silicon nitride varies from 1200 to 1500 °C in relation to synthesis method and the properties of amorphous materials,[207,208] while that of silicon carbide is around 900 °C,[209] which indicates the amorphous silicon carbide can be transferred to cubic silicon carbide during pyrolysis at 1200 °C. The interlayer distance from hard carbon has been shown in table 6-1.

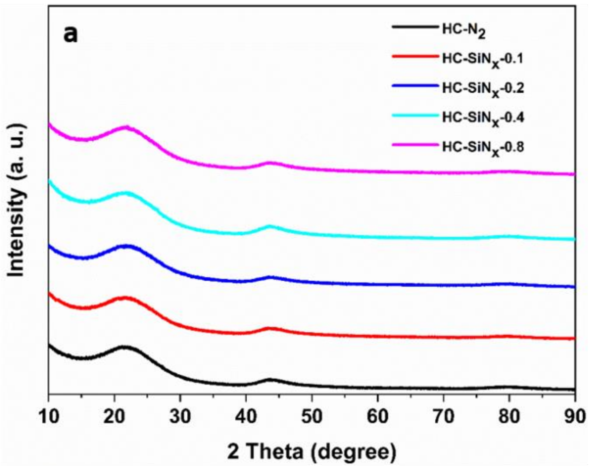

Figure 6-4 XRD patterns of composites with (a) silicon nitride or (b) silicon oxycarbide produced by reacting cellulose with different volumes of silicon chloride and firing under nitrogen or argon at 1400 °C.

The amount of silicon-containing phase in the composites was measured by thermogravimetric analysis (Fig. 6-5). The mass loss between 400 and 650 ºC can be attributed to the burning of hard carbon and the oxidation of silicon nitride or silicon carbide. The non-stoichiometric property makes it difficult to calculate the exact mass ratio of SiN_x and SiOC in the composite. In addition, the oxidation product at 1000 °C is not the pure silicon dioxide due to the oxidation resistance of silicon nitride and silicon carbide.[210,211] The typical combustion analysis makes it difficult to measure the Si content. Loadings here are calculated by assuming that Si_3N_4 and SiC are present in the composite and that they are fully oxidized to silicon dioxide, whilst recognizing that that results in some uncertainty about the actual loading.

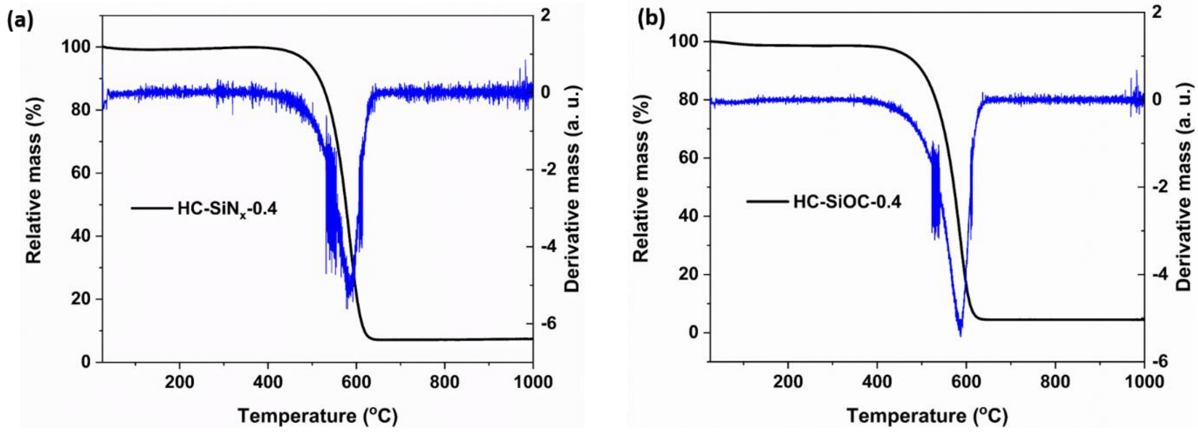

Figure 6-5 TGA and TGA differential results of (a) HC-SiN_x-0.4 and (b) HC-SiOC-0.4 composites.

$$\mathrm{aC} + bSi_3N_4 + (\mathrm{a} + 7\mathrm{b})\mathrm{O}_2 \rightarrow 3bSiO_2 + 4\mathrm{bN}O_2 + aCO_2 \text{ Equation 6-1}$$

$$aC + bSiC + (a + 2b)O_2 \rightarrow bSiO_2 + (a + b)CO_2 \text{ Equation 6-2}$$

Assume the weight of HC-Si_3N_4-0.4 composite is "m" gram, and the mass ratio of Si_3N_4 in composite is "x". The calculated SiO_2 should be 180.27mx/140.27 after heating at 1000 °C. The weight remaining is 8.92% from thermogravimetric analysis. In that case, the value of x should be 6.9%. For the HC-SiOC-0.4 composite, the similar calculation process was carried out and the mass content is 3.9%.

Table 6-1 Structural parameters for hard carbon coated with SiN_x and SiOC.

Samples	TGA (*wt*%)	BET (cm^2 g^{-1})	d_{002} (Å)	I_D/I_G
HC-N_2	-	75	4.040 (6)	2.2
HC-Si_3N_4-0.1	4.6	75	4.029 (9)	2.2
HC-Si_3N_4-0.2	5.1	64	4.024 (7)	2.5
HC-Si_3N_4-0.4	6.9	84	4.004 (9)	2.5
HC-Si_3N_4-0.8	10.5	99	4.042 (7)	2.2
HC-Ar	-	86	4.020 (7)	2.6
HC-SiC-0.1	3.4	41	4.002 (8)	2.3
HC-SiC-0.2	3.5	43	4.004 (8)	2.3
HC-SiC-0.4	3.9	26	4.002 (7)	2.3
HC-SiC-0.8	4.4	62	4.028 (8)	2.2

Fig. 6-6 shows the Raman spectra of the hard carbon composites with various mass ratios of carbon to silicon nitride or silicon oxycarbide. No obvious peak of silicon nitride (~440 cm^{-1})[212] or silicon carbide (~860 cm^{-1})[213] was shown in the spectrum. Two broad peaks with Raman shift of 1310 and 1610 cm^{-1} corresponds to the disordered (D-band) and ordered graphitic (G-band) structures in hard carbon, respectively.

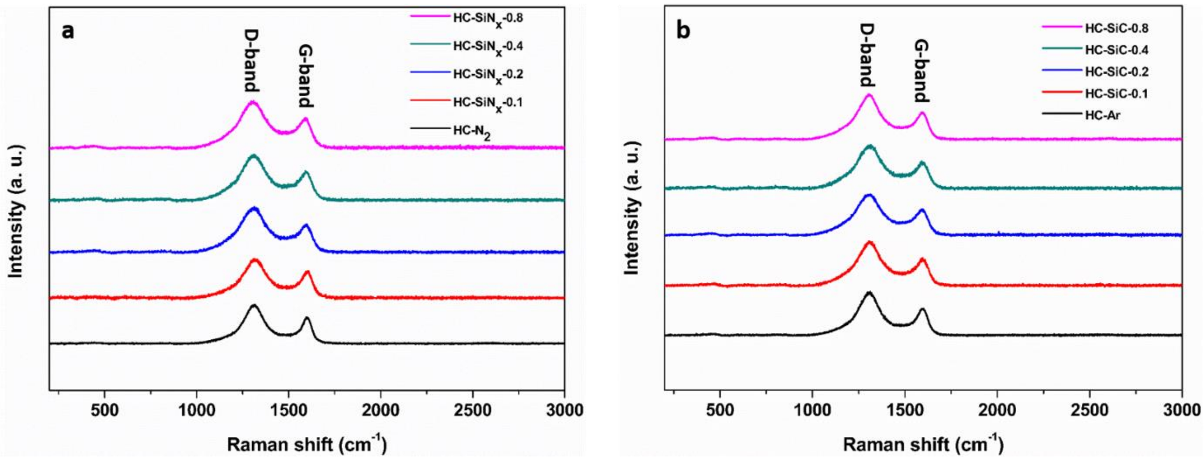

Figure 6-6 Raman spectra of hard carbon composites with with (a) silicon nitrides and (b) silicon oxycarbides with loadings as labelled.

The curve fitting (Fig. 6-7) applied D and G bands with Lorentzian functions, and G3 band with Gaussian functions described by others.[185] The intensity ratio of I_D/I_G (> 2.2) shows a highly disordered structure of hard carbon, which is a good indicator for good sodium insertion performance.[53,54]

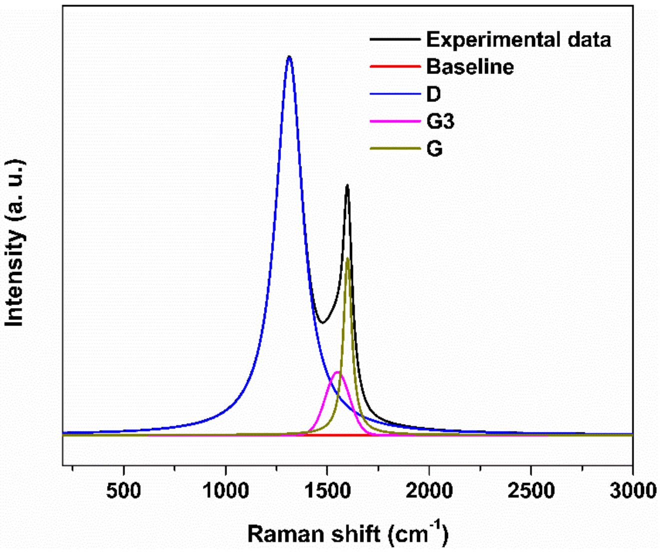

Figure 6-7 Typical Raman spectrum fitting of HC-SiN_x-0.4 composite.

Fig. 6-8 displays the nitrogen adsorption/desorption isotherms of hard carbon composites with silicon nitrides and oxycarbides. The spectrum shows type IV isotherms and H4 type hysteresis, suggesting the presence of micro-and mesopores in the samples. A feature common to these hysteresis loops is that complete closure points should appear at nitrogen's boiling point around $P/P_0 = 0.42$. However, for some materials containing micropores, low pressure hysteresis can be extended to the lowest attainable pressures as seen in these isotherms.[133-135]

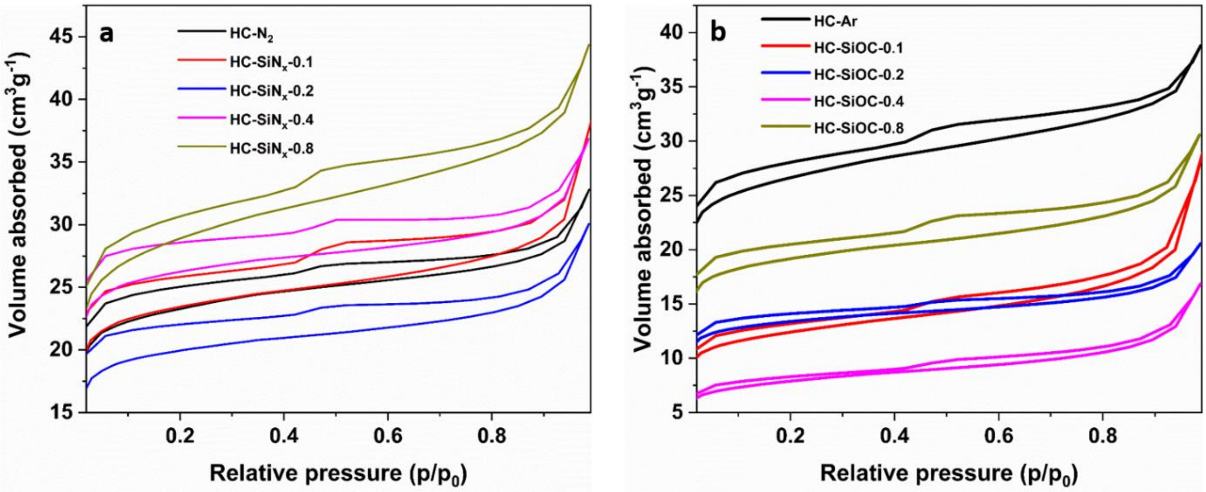

Figure 6-8 Nitrogen adsorption-desorption isotherms of hard carbon composites with (a) silicon nitrides and (b) silicon oxycarbides with loadings as labelled.

The pore size distributions calculated from the isotherms (Fig. 6-9) prove the presence of micro and mesopores. BET surface area (Table 6-1) was calculated to link with the initial Coulombic efficiency which will discussed later. As the volume of silicon tetrachloride increases, the BET surface area does not change significantly for the silicon nitride composites, while the BET surface area of silicon oxycarbides composites decreases dramatically to the half value of that of pure hard carbon. The reason may be that the amorphous-crystalline transition temperature is different between silicon nitride and silicon carbide as we discussed above. The lower transition temperature for carborthermal reduction of silicon carbide would result crystalline particles and then decrease the BET surface area.

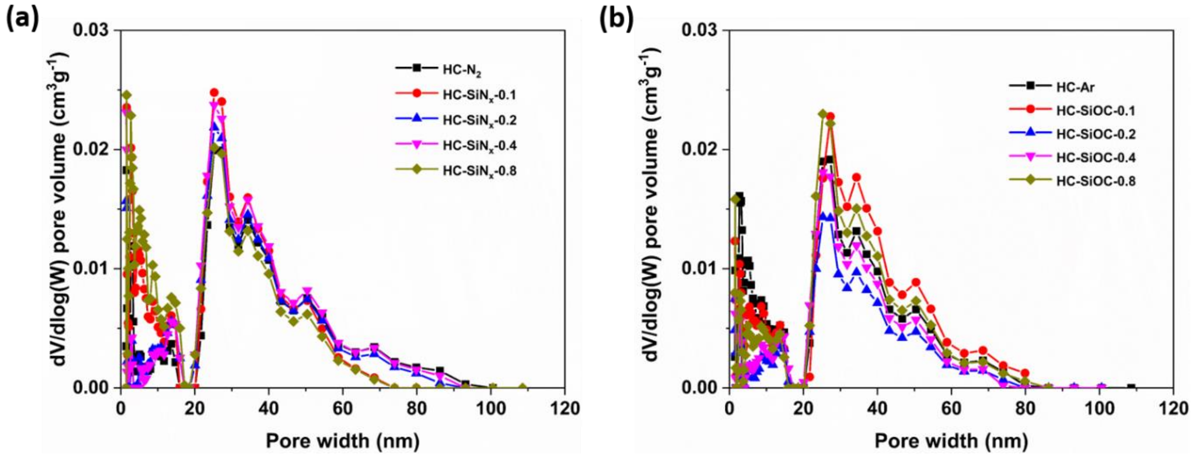

Figure 6-9 Pore size distribution of hard carbon composites with (a) silicon nitrides and (b) silicon oxycarbides with loadings as labelled.

Fig. 6-10 shows exemplar Si 2p XPS spectra and curve-fitting for the SiN_x and SiOC composites. XPS data were analysed using the Casa XPS software package with the XPS binding energy scale calibrated to graphitic carbon at 284.6 eV. Core peaks were fitted with a nonlinear Shirley-type background.[128] Peak positions and areas were optimised by a weighted least-squares fitting method using 70% Gaussian and 30% Lorentzian line shapes. The chemical shift in XPS spectrum is related to the electric charge distribution around the atoms. The Pauling electronegativity of elements involved in our measurement increase in the order Si (1.8) < C < (2.5) < N (3.0) < O (3.5).[214] Thus the Si 2p binding energy peak shifts to higher position with increasing electronegativity of the neighbouring atoms. For the SiN_x composites, the fitted Si 2p spectrum consists of two intense peaks around 103.6 and 102.1 eV correspond to Si-O and Si-N, respectively,[211,215,216] and one weak peak around 102.8 eV, which can be attributed to silicon oxynitride.[208,217] The presence of SiN_x can be further confirmed by the N 1s spectrum in Fig. 6-10b. The binding energy at 397.7 and 399.6 eV corresponds to the SiN_x and silicon oxynitride, respectively.[201,218] For comparison, the spectrum for SiOC composites show a Si-O peak around 103.7 eV and two more peaks around 100.9 and 102.1 eV, which agree well with Si-C and Si-O-C, respectively.[219-221] No obvious Si-C peak around 282.8 eV[221] can be found in the C 1s (Fig. 6-10c) even though both components of Si and C are significant, which is similar to other reports.[222,223] In both systems, oxygen appears in the spectra although no oxygen was deliberately introduced. At least some of that oxygen concentration is surface contamination after exposure to air as has been reported previously.[223-225]

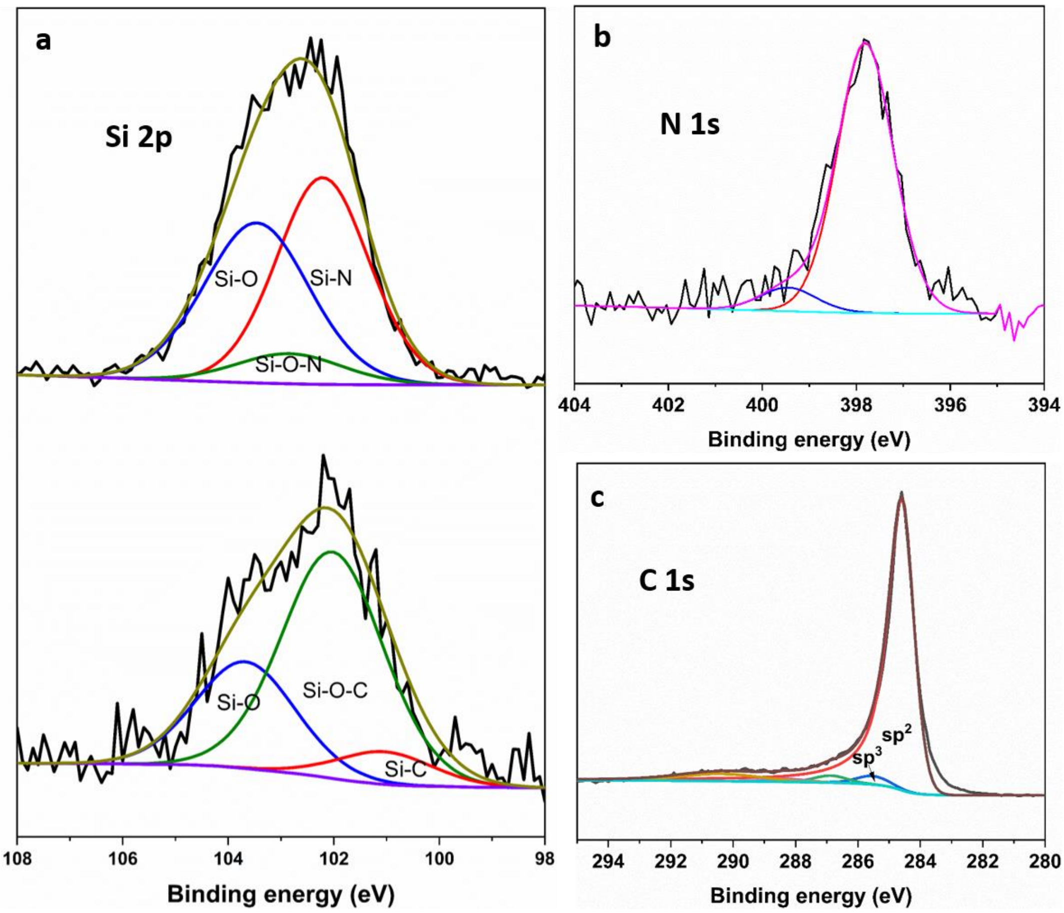

Figure 6-10 (a) Si 2p XPS spectrum and curve fitting of HC-SiN$_x$-0.4 and HC-SiOC-0.4 composites; (b) N 1s spectrum of HC-SiN$_x$-0.4 and (c) C 1s spectrum of HC-SiOC-0.4.

The composites were suspended into inks and made into electrodes to investigate their electrochemical properties. The electrolyte was 1 M $NaClO_4$ in EC/DEC. Sodium half-cells were assembled in the glove box and then multiple charge-discharge cycles were performed under galvanostatic conditions. XPS measurement was also carried out on electrodes before and after cycling. HC-SiN$_x$-0.4 and HC-SiOC-0.4 electrodes were running at 50 mA g^{-1} and then stopped after full discharging. For the comparison, two more electrodes were prepared without any charging-discharging. The cells were disassembled in the glovebox before transferred to the XPS chamber. Ar-ion sputtering was carried out with an etching rate of 2 nm min^{-1} for 6 min. Fig. 6-11 displays the Si 2p spectrum of HC-SiN$_x$-0.4 and HC-SiOC-0.4 electrodes without cycling after Ar-ion etching to remove a surface layer. After sputtering, HC-SiN$_x$-0.4 electrode shows a Si-N peak at 102.2 eV while HC-SiOC-0.4 electrode shows Si-O, Si-O-C and Si-C peaks at 103.7, 102.0 and 100.9 eV, respectively. It indicates the SiN component and SiO$_x$C$_y$ component in the HC-SiN$_x$-0.4 and HC-SiOC-0.4 electrodes, respectively.

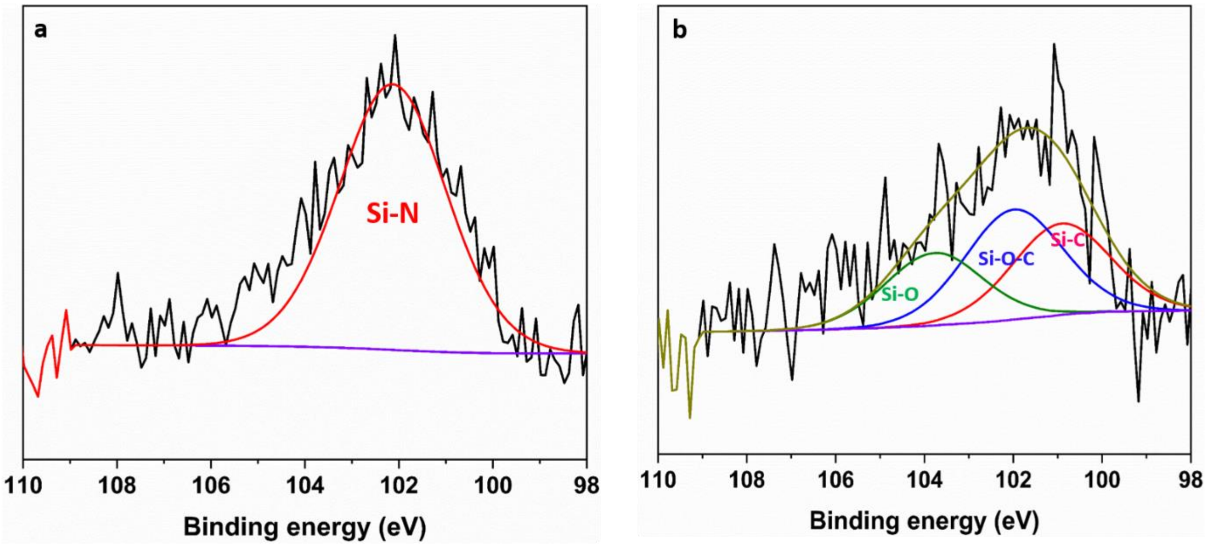

Figure 6-11 Si 2p spectrum of (a) HC-SiN$_x$-0.4 and (b) HC-SiOC-0.4 electrodes before sodiation.

Fig. 6-12 shows the first cyclic differential capacity plots of composites with silicon nitride and silicon oxycarbide. The sharp peaks around 0.1 V *versus* Na$^+$/Na is related to the sodium insertion/disinsertion from hard carbon.[73,205] In addition, the broad peaks around 0.5 and 1.1 V *versus* Na$^+$/Na correspond to the decomposition of electrolyte and formation of a solid electrolyte interface (SEI).[74]

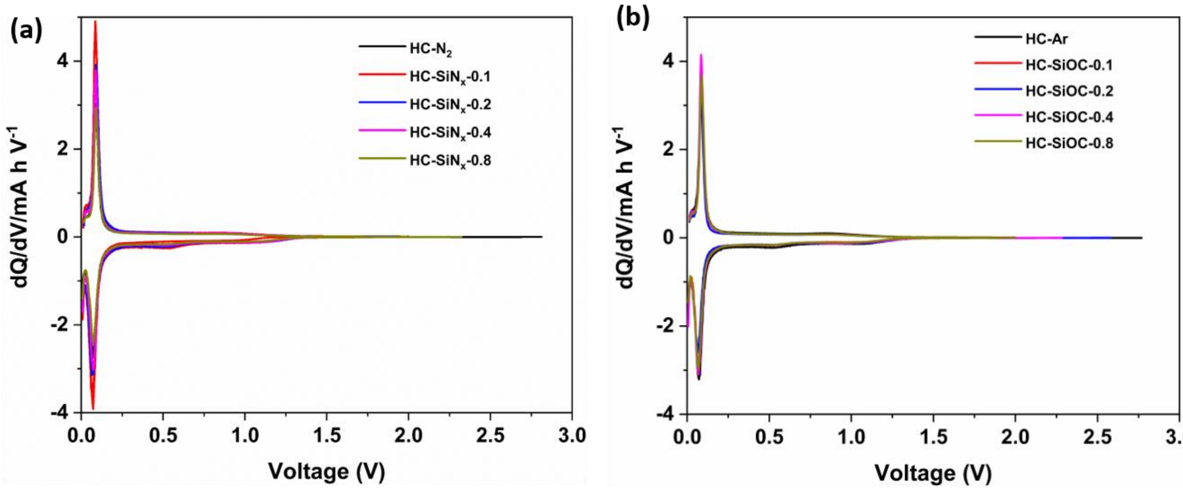

Figure 6-12 First cycle differential capacity plots of hard carbon composites with (a) silicon nitrides and (b) silicon oxycarbides with loadings as labelled.

Differential capacity plots showed that an SEI layer had formed by sodiation in discharging and this was further examined by XPS. Fig. 6-13 shows C 1s depth profile of a sample after first discharging. SEI layer were formed during sodiation by discharging in the half cell. SEI induced by diglyme-based electrolyte contains both organic (i.e., RONa and ROCO$_2$Na, near the electrolyte/SEI interface) and inorganic (Na$_2$CO$_3$, near the SEI/electrode interface) components.[226,227] The increased intensity of C-C species with increased etching depth is associated with contribution from HC located underneath the SEI layer.[228] For HC-SiN$_x$-0.4 composite, the C 1s peak intensity corresponding to C=O species decreases in the first two sputtering steps and then stays the same. While the C=O species almost remain constant with the increase of sputtering time in HC-SiOC-0.4 composite. The different intensity decrease trends are related to the amount of organic species.[226] It has been reported that organic species of RCH_2ONa facilitates sodium ion transport.[229] Thus the higher amount of organic species in HC-SiN_x-0.4 reduce the energy barrier of Na^+ diffusion, inducing better capacity performance.

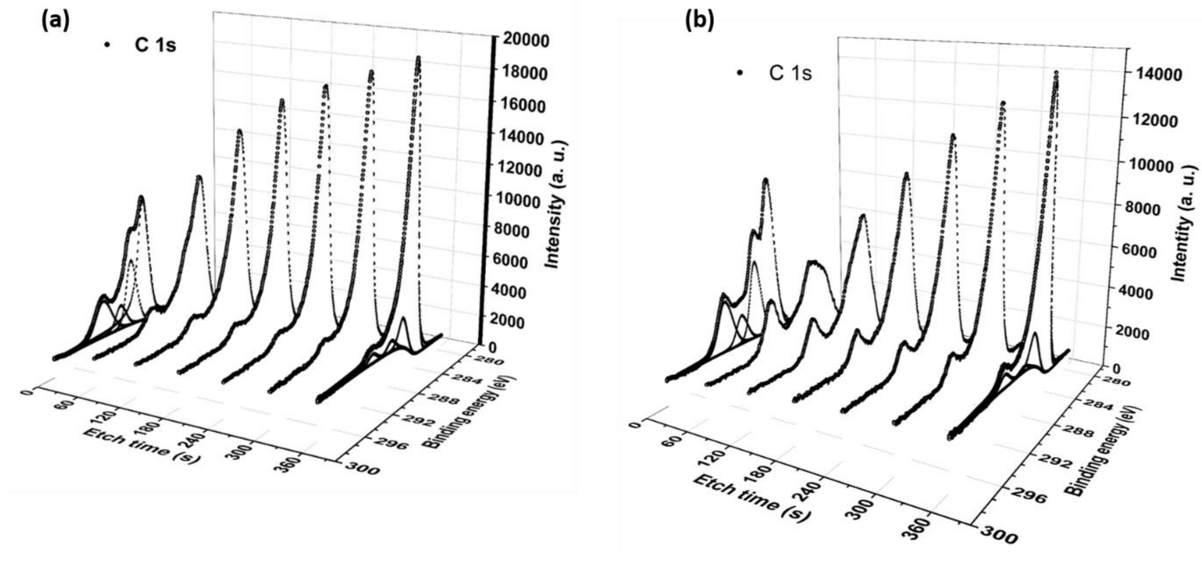

Figure 6-13 The C 1s depth profile of (a) HC-SiN_x-0.4 and (b) HC-SiOC-0.4 composites after first discharging as a function of Ar-ion etch time.

Fig. 6-14a shows the cyclic performance of hard carbon and composites with silicon nitride loading. The HC-SiN_x electrodes showed oxidation capacities of 303, 312, 351 and 326 mA h g^{-1}, with increasing silicon nitride content. When the silicon chloride increased from 0 to 0.4 mL, the reversible capacity at 50 mA g^{-1} after 50 cycles increased from 243 to 299 mA h g^{-1}. The capacity decreased to 280 mA h g^{-1} when the amount of silicon chloride used in the synthesis process was further increased to 0.8 mL. The increase of 67 mA h g^{-1} in the oxidation (reversible) capacity was achieved upon incorporation of 6.9 wt% Si_3N_4 on HC. This increase of 67 mA h g^{-1} in specific capacity (normalized by the mass of the whole active material, Si_3N_4 and hard carbon) corresponds to a very high specific capacity of 971 mA h g^{-1} when normalized by the mass of Si_3N_4 in the HC-SiN_x-0.4 composite. The initial Coulombic efficiency (ICE) is 66% and 69% for HC-N_2 and HC-SiN_x-0.4 electrode, respectively. Both Coulombic efficiencies reach 96% in the second cycle, 98% in the ninth cycle and retain similar values over the remaining 40 cycles.

The composites with silicon oxycarbides (Fig. 6-14b) deliver similar oxidation capacity of 295 mA h g^{-1} in the first cycle, better than that of 283 mA h g^{-1} from HC-Ar. After 50 cycles, composites showed reversible capacity around 260 mA h g^{-1} and capacity retention of 88.1%, while the HC-Ar showed capacity of 245 mA h g^{-1} and capacity retention of 86.5%. Due to the decrease of BET surface area after loading silicon oxycarbides on hard carbon, the composites show a higher ICE (around 72%) than the pure hard carbon (63%).

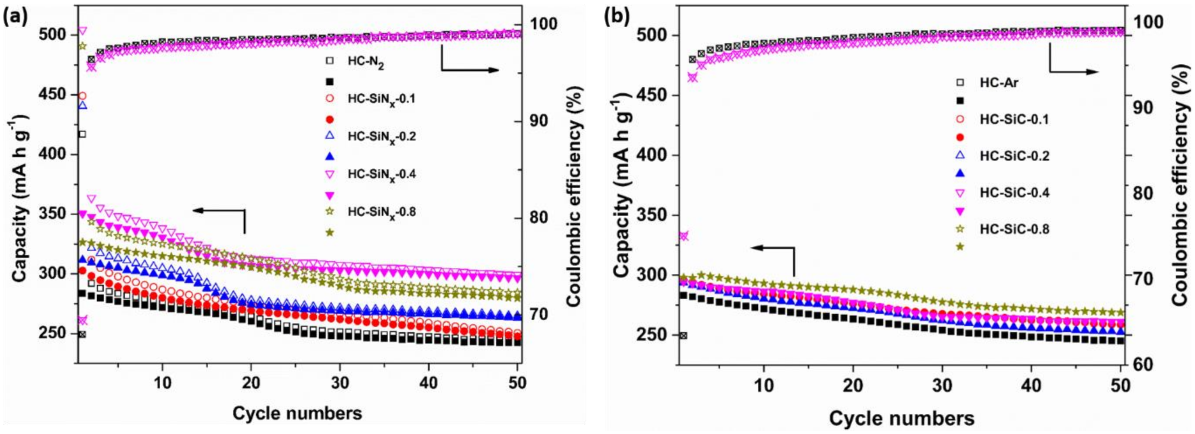

Figure 6-14 Cycling performance of hard carbon composites with (a) silicon nitrides and (b) silicon oxycarbides with loadings as labelled. Open symbols show reduction capacity and closed symbols show oxidation capacity.

Fig. 6-15 shows the electrochemical impedance spectra (EIS) of HC-SiN$_x$-0.4 and HC-SiOC-0.4 electrodes in 50 cycles. The width of semicircle in the Nyquist plot decreases after 10 cycles, which is related to the formation of stable SEI on the surface of electrode. In the later 40 cycles, the width of semicircle becomes wider, suggesting the increase of charge transfer resistance during cycling.

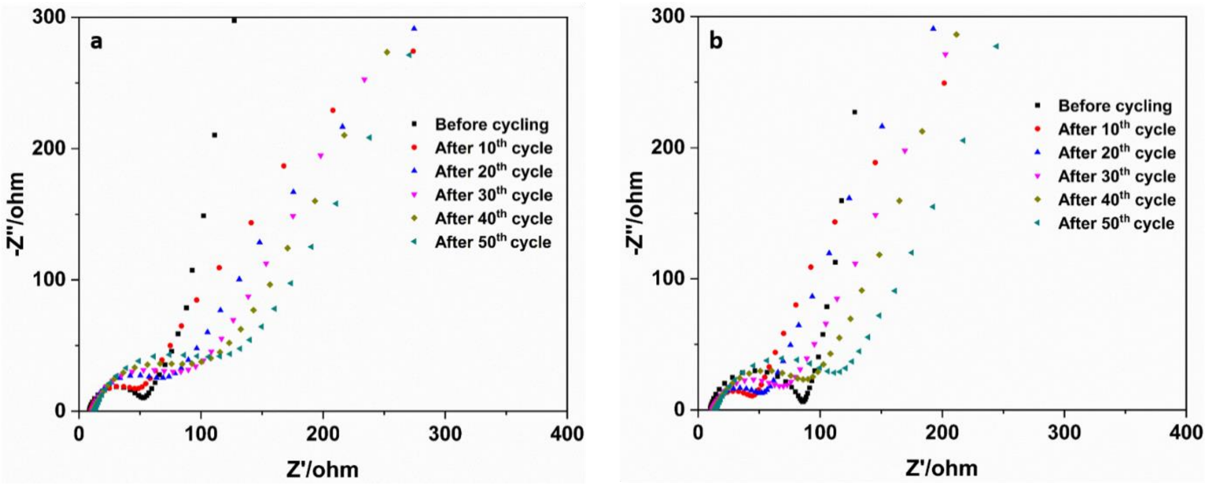

Figure 6-15 Nyquist plots of HC-SiN$_x$-0.4 and HC-SiOC-0.4 electrodes in 50 cycles.

Fig. 6-16 displays the EIS of hard carbon obtained with nitrogen and argon gas. While the charge transfer resistance is similar for both hard carbon and composites before cycling, the silicon nitrides and silicon oxycarbides coated hard carbon show a smaller semi-circle diameter after 50 cycles, suggesting the presence of silicon nitrides and silicon oxycarbides decreases the charge transfer resistance.

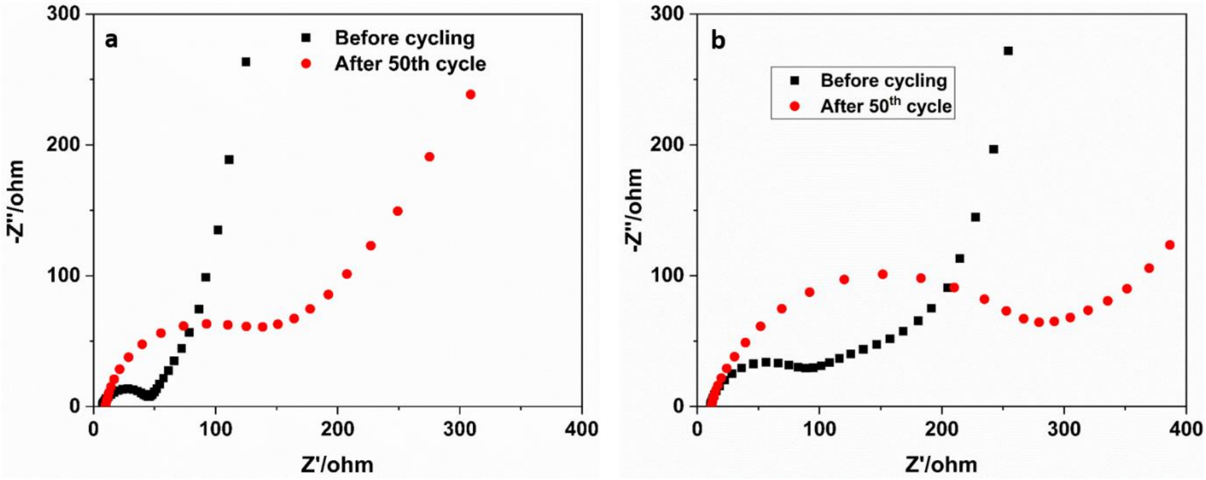

Figure 6-16 Nyquist plots of HC-N_2 and HC-Ar electrodes before and after 50 cycles.

6.4 Conclusions

Hard carbon composites with silicon nitride and silicon oxycarbide have been obtained by carbothermal nitridation and carbothermal reduction process, respectively. Amorphous SiN_x and SiOC particles were dispersed evenly on hard carbon. The silicon oxycarbide-hard carbon composite maintained an oxidation capacity of 260 mA h g^{-1} at 50 mA g^{-1} after 50 cycles, and the composite shows a higher ICE (around 72%) than the pure hard carbon (63%) due to a lower surface area. The as-prepared HC-SiN_x-0.4 electrode shows a reversible capacity of 299 mA h g^{-1} and a capacity retention of 85.2% at 50 mA g^{-1} after 50 cycles. EIS analysis suggests that the better capacity performance is mainly due to the presence of silicon nitride and silicon oxycarbides increase the charge transfer conductivity during cycling.

7. Conclusions and future perspectives

The development of sodium ion batteries (SIBs) has attracted much attentions due to the low cost of raw materials in consider of large scale grid storage system. The published papers with topic of "sodium ion battery" increased from 84 in 2011 to 2349 in 2019 (Web of Science Core Collection).[230] Numerous anode materials especially for carbon based materials have been obtained to contribute to sodium battery community. Graphite, which is commonly used in LIBs, was not suitable for SIBs due to the unmatchable value between the interlayer distance and sodium ionic radius. A good attempt was expanding the interlayer spacing from 3.7 to 4.3 Å, resulting a good capacity of 283 mA h g^{-1} at 20 mA g^{-1}.[145] On the other hand, by using ether-based electrolytes, the reduced strength of the carbon-sodium bonds contributed to ultrafast intercalation/de-intercalation, inducing a good reversible capacity of 100 mA h g^{-1} at high current of 10-30 mA g^{-1} in graphite.[231] However, carbon materials with low degree graphitization were reported extensively due to the relatively high capacity performance. Hard carbon shows attractive sodium storage performance by enlarging the interlayer spacing and controlling defects and porosity. These carbon materials[55,56,232] deliver high capacity over 250 mA h g^{-1} and a plateau region at low potential (cal. 0.2 V *vs* Na^+/Na), which makes it as the most promising candidate among all the anode materials in SIBs.

Nitrides and carbides have been attracted attention due to the high theoretical capacity in SIBs. However, quite a few nitrides and carbides were investigated. Hector's group reported the first use of metal nitride (Ni_3N) as anode active material in SIBs in 2013.[105] The good capacity performance result from surface reaction makes the Cu_3N[106] and Sn_3N_4[123] as the good examples by using metal nitrides in SIBs. On the other hand, molybdenum carbide was most studied metal carbide in SIBs after Çakır et al.[116] and Sun et al.[117] theoretically proved the possibility of applying Mo_2C in SIBs. The continued works with nitrides and carbides makes them as promising materials in SIBs.

The focus of this thesis was try to synthesize nitrides/carbides coated on hard carbon and apply these composites on sodium ion batteries. In the first part of the thesis, cotton wool and resorcinol-formaldehyde were used to synthesize hard carbon. Pyrolysis temperature and gas flow rate were investigated to find the optimized synthesis route. The sodium storage properties of hard carbon obtained under different synthesis conditions were investigated. Hard carbon obtained from cotton wool at 1400 °C shows a reversible capacity of 319 mA h g^{-1} at current of 20 mA g^{-1}. Similar performance has been reported for hard carbon obtained from cotton wool (by heating at 1300 °C), which delivered an oxidation (reversible) capacity of 315 mA h g^{-1} at 30 mA g^{-1}.[69] More recently, hard carbon produced by pyrolysing lotus seedpod at 1200 °C achieved a higher reversible capacity of 328 mA h g^{-1} at 50 mA g^{-1}.[74] Other biomass materials are likely to feature in future work to further develop hard carbon capacity.

The sodium storage analysis is consistent with the traditional insertion/absorption mechanism in the hard carbon. The slope region is more related with interlayer distance and degree of graphitization while the plateau part is more related to the micropores size and volume. Recent papers show that there still is no settled view in the scientific community on the sodium storage mechanism of hard carbon. Cao *et al.*[50] showed that Na intercalation into graphene sheets occurs in the plateau region at low potentials and Ji *et al.*[84] proposed that the slope capacity corresponded to the defect concentration in the hard carbon. Thus further research work is required to full understand the application of hard carbon in SIBs.

In the second part, the focus was synthesis of composites based on hard carbon. An effective way to obtain composites with metal nitrides and carbides for sodium cell and other energy applications has been proposed. Titanium chloride was used to investigate the synthesis process as the titanium nitride and titanium carbide are stable when heating temperature is 1400 °C. Reactions of titanium tetrachloride with cellulose followed by carbothermal nitridation or reduction during firing produce hard carbon with nanocrystalline titanium nitride or carbide decorated over the surfaces (Fig. 7-1). In sodium cells both composites show similar first cycle capacities to hard carbon, but the titanium nitride composite delivers a better capacity retention (85.2%) after 50 cycles than that of hard carbon (74.3 %). *Ex situ* grazing incidence XRD patterns of the HC-TiN composites suggest the reactions occurring only on the surface region of TiN. The TiC composites produce slightly lower capacities and, unlike TiN, do not improve the cycling behaviour. The larger TiC crystallite size of TiC in HC-TiC composite may reduce its ability to participate in reactions, or the TiC surfaces may be less reactive than the TiN.

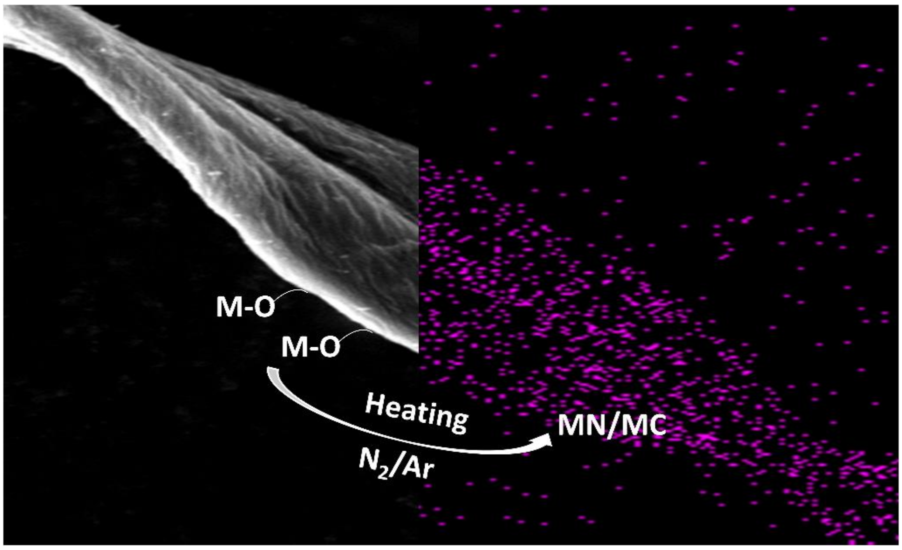

Figure 7-1 The synthesis procedure for HC-MN or HC-MC obtained from cotton wool with nitrogen or argon gas, respectively.

Recently some researchers reported the application of TiN in lithium ion batteries. Zhang et al.[233] reported that 10% TiN coated $LiFePO_4$ delivered a discharge capacity of 159 mA h g^{-1} at 0.1 C. Zhang et al.[143] deposited TiN on carbon fibres using a sol-gel method and then applied this coating in flexible supercapacitors. To our best knowledge, however, this work was the first to apply nanocrystalline titanium nitride or carbide in SIBs. Moreover, the method is applicable to depositing other metal nitrides or carbides on carbon surfaces. This could be for batteries, but the literature[181,182]also suggests that such carbon-metal nitride/carbide composites could be applied in electrocatalysis and supercapacitors.

In the third part, the aim was to obtain hard carbon composites with high capacity. VN-HC composites have been synthesised using the same pyrolysis process after reacting $VOCl_3$ with cellulose. A VN-HC composite with 8.6 *wt*% VN showed the largest reversible capacity of 293 mA h g^{-1} after 50 cycles at 50 mA g^{-1}. Since VN is the source of this extra capacity, normalization by the mass of VN in the composite electrode provides a more accurate measure of the degree of utilization of VN in the VN-HC composite in the energy storage reactions, and the value of capacity of 605 mA h g^{-1} is the highest specific capacity of VN in sodium ion batteries that has been reported. The XRD characterization of the electrodes after the first reduction (sodiation) showed the transformation of VN to a new phase ($VN_{0.2}$ and other amorphous phases), and back again to VN after the first oxidation (de-sodiation). XRD also showed that the core of the VN nanoparticles remained unreacted, thus further decreasing of nanoparticle size could lead to improved performance.

Some VN works were reported in SIBs previously, Song[111] reported VN quantum dots dispersed onto graphene with a reversible capacity of 237 mA h g^{-1} at 74 mA g^{-1}. More recently, Wei *et al*[183] reported a new layered VN material that delivered a capacity of 372 mA h g^{-1} at 50 mA g^{-1}. Moreover, the use of VN in sodium-ion batteries was studied by Cui et al.[107] who reported VN microparticles with stable, reversible capacity of ~300 mA h g^{-1} at 124 mA g^{-1} and reported HRTEM and XANES data that suggested the conversion of VN to $VN_{0.35}$ as part of the mechanism of charge storage. The different conversion products reported here indicated that the conversion mechanism needs to be investigated for the further work.

In the fourth part, the aim was to apply cheap nitrides/carbides precursor to obtain hard carbon composites. Hard carbon composites with silicon nitrides and silicon oxycarbides have been obtained by the similar synthesis process. The silicon oxycarbide coated hard carbon showed oxidation capacity of 260 mA h g^{-1} at 50 mA g^{-1} in 50 cycles, and the small BET surface area of composites delivers high initial Coulombic efficiency around 72%. Weinberger et al.[202] synthesized SiOC spheres and showed reversible capacity around 200 mA h g^{-1} at 25 mA g^{-1} with initial Coloumbic efficiency of 47%.[202] Kaspar et al.[234] obtained SiOC-hard carbon composites from the polyorganosiloxane and glucose. During sodium insertion process, SiOC/HC_G shows a reversible capacity of 201 mA h g^{-1} in the first cycle and 141 mA h g^{-1} in 50 cycles at current of 37 mA g^{-1}. The capacity retention is 70%, which is worse than that of 86% obtained from our work.

The as-prepared silicon nitride coated on hard carbon shows a reversible capacity of 351 mA h g^{-1} at 50 mA g^{-1}, better than that of 284 mA h g^{-1} from pure hard carbon. The increase of 67 mA h g^{-1} in the oxidation (reversible) capacity was achieved upon incorporation of 6.9 wt% Si_3N_4 on HC. This increase of 67 mA h g^{-1} in specific capacity (normalized by the mass of the whole active material, Si_3N_4 and hard carbon) corresponds to a very high specific capacity of 971 mA h g^{-1} when normalized by the mass of

Si_3N_4 in the HC-SiN_x-0.4 composite. The HC-SiN_x-0.4 electrode delivered a capacity of 299 mA h g^{-1} and the retention of 85% in 50 cycles. To our best knowledge, this is first time silicon nitride has been used in SIBs. The good capacity performance suggests that the hard carbon coated with silicon nitride can be applied as anode materials in SIBs.

Overall, the thesis gave a mini review on the application of nitrides, carbides and hard carbon in SIBs. An effective methodology to obtain hard carbon composites with nitrides or carbides was introduced. The as-prepared new materials such as VN-HC and SiN_x-HC showed higher reversible capacity, and TiN-HC, and SiOC exhibited better capacity retention. The electrochemical performance and related reaction mechanism (Fig. 7-2) indicated that the nitrides/carbides coated on hard carbon can be applied in SIBs.

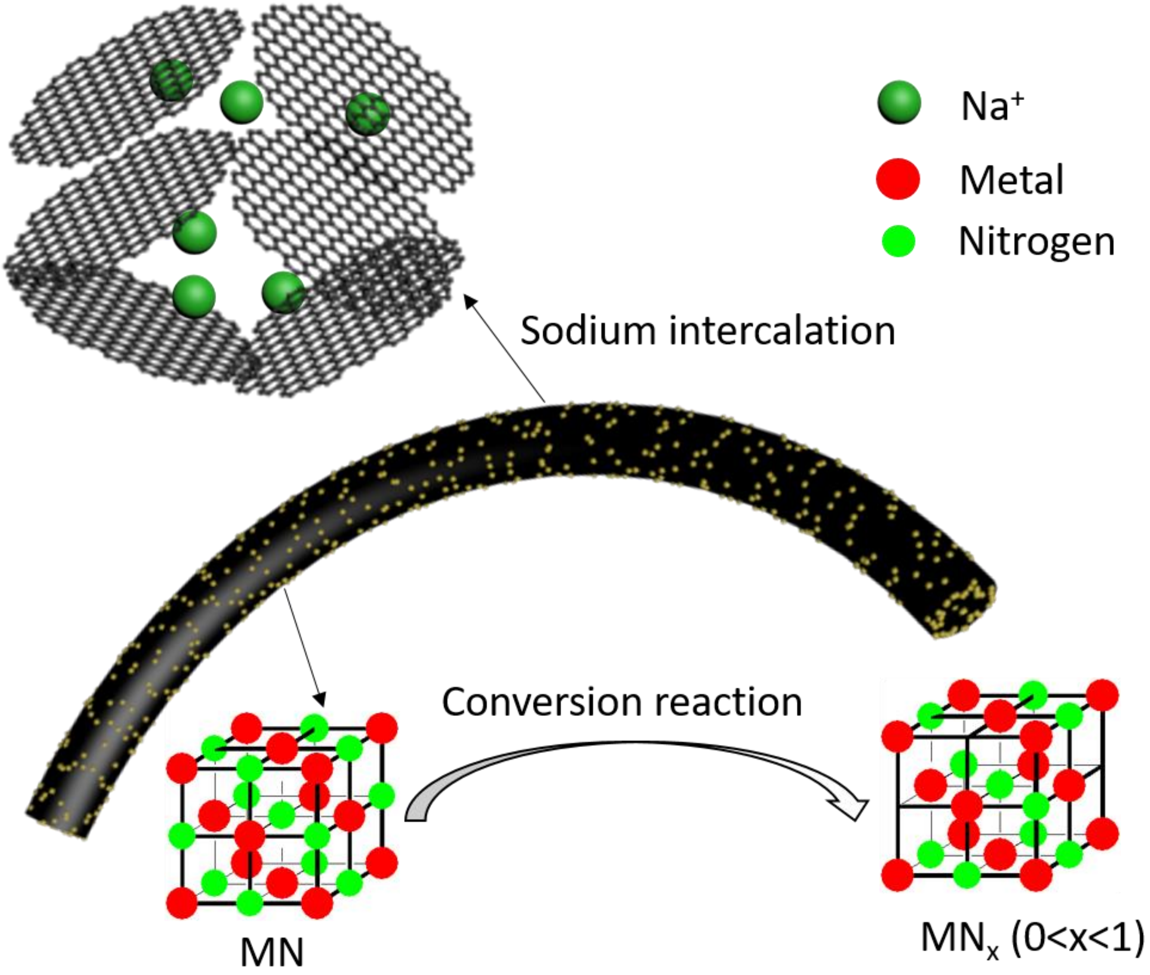

Figure 7-2 Sodium intercalation and conversion reaction illustrate the sodium storage in HC-MN composites.

8. References

(1) Parant, J.-P.; Olazcuaga, R.; Devalette, M.; Fouassier, C.; Hagenmuller, P. Sur Quelques Nouvelles Phases de Formule Na_xMnO_2 ($x \leqslant 1$). *J. Solid State Chem.* **1971**, *3*, 1-11.

(2) Whittingham, M. S. Chemistry of intercalation compounds: metal guests in chalcogenide hosts. *Prog. in Solid State Chem.* **1978**, *12*, 41-99.

(3) Nagelberg, A. S.; Worrell, W. L. A thermodynamic study of sodium-intercalated tantalum(IV) and titanium(IV) sulfides. *J. Solid State Chem.* **1979**, *29*, 345-354.

(4) Braconnier, J. J.; Delmas, C.; Fouassier, C.; Hagenmuller, P. Electrochemical Behavior of the Sodium Cobalt Oxide (Na_xCoO_2) Phases. *Mater. Res. Bull.* **1980**, *15*, 1797-1804.

(5) Slater, M. D.; Kim, D.; Lee, E.; Johnson, C. S. Sodium-ion Batteries. *Adv. Funct. Mater.* **2013**, *23*, 947-958.

(6) Carmichael, R. S.: *Practical handbook of physical properties of rocks and minerals*; CRC press, 2017.

(7) Adelhelm, P.; Hartmann, P.; Bender, C. L.; Busche, M.; Eufinger, C.; Janek, J. From lithium to sodium: cell chemistry of room temperature sodium–air and sodium–sulfur batteries. *J. Nanotechnol.* **2015**, *6*, 1016-1055.

(8) Pan, H.; Hu, Y.-S.; Chen, L. Room-temperature stationary sodium-ion batteries for large-scale electric energy storage. *Energy Environ. Sci.* **2013**, *6*, 2338-2360.

(9) Yabuuchi, N.; Kubota, K.; Dahbi, M.; Komaba, S. Research development on sodium-ion batteries. *Chem. rev.* **2014**, *114*, 11636-11682.

(10) Matsumoto, K.; Hwang, J.; Kaushik, S.; Chen, C.-Y.; Hagiwara, R. Advances in sodium secondary batteries utilizing ionic liquid electrolytes. *Energy Environ. Sci.* **2019**, *12*, 3247-3287.

(11) Che, H.; Chen, S.; Xie, Y.; Wang, H.; Amine, K.; Liao, X.-Z.; Ma, Z.-F. Electrolyte design strategies and research progress for room-temperature sodium-ion batteries. *Energy Environ. Sci.* **2017**, *10*, 1075-1101.

(12) Jache, B.; Adelhelm, P. Use of graphite as a highly reversible electrode with superior cycle life for sodium-ion batteries by making use of co-intercalation phenomena. *Angew. Chem. Int. Ed.* **2014**, *53*, 10169-10173.

(13) Seh, Z. W.; Sun, J.; Sun, Y.; Cui, Y. A Highly Reversible Room-Temperature Sodium Metal Anode. *ACS Cent. Sci.* **2015**, *1*, 449-455.

(14) Ding, C.; Nohira, T.; Kuroda, K.; Hagiwara, R.; Fukunaga, A.; Sakai, S.; Nitta, K.; Inazawa, S. NaFSA–C1C3pyrFSA ionic liquids for sodium secondary battery operating over a wide temperature range. *J. Power Sources* **2013**, *238*, 296-300.

(15) Delmas, C.; Braconnier, J. J.; Maazaz, A.; Hagenmuller, P. Soft chemistry in A_xMO_2 sheet oxides. *Rev. Chim. Miner.* **1982**, *19*, 343-351.

(16) Hwang, J. Y.; Myung, S. T.; Sun, Y. K. Sodium-ion batteries: present and future. *Chem. Soc. Rev.* **2017**, *46*, 3529-3614.

(17) Kundu, D.; Talaie, E.; Duffort, V.; Nazar, L. F. The emerging chemistry of sodium ion batteries for electrochemical energy storage. *Angew. Chem. Int. Ed.* **2015**, *54*, 3431-3448.

(18) Delmas, C.; Fouassier, C.; Hagenmuller, P. Structural classification and properties of the layered oxides. *Physica B+ c* **1980**, *99*, 81-85.

(19) Delmas, C.; Braconnier, J.-J.; Fouassier, C.; Hagenmuller, P. Electrochemical intercalation of sodium in Na_xCoO_2 bronzes. *Solid State Ion.* **1981**, *3*, 165-169.

(20) Yabuuchi, N.; Kajiyama, M.; Iwatate, J.; Nishikawa, H.; Hitomi, S.; Okuyama, R.; Usui, R.; Yamada, Y.; Komaba, S. P_2-type $Na_{(x)}[Fe_{(1/2)}Mn_{(1/2)}]O_2$ made from earth-abundant elements for rechargeable Na batteries. *Nat. Mater.* **2012**, *11*, 512-517.

(21) Kim, S.-W.; Seo, D.-H.; Ma, X.; Ceder, G.; Kang, K. Electrode materials for rechargeable sodium-ion batteries: potential alternatives to current lithium-ion batteries. *Adv. Energy Mater.* **2012**, *2*, 710-721.

(22) DiVincenzo, D.; Mele, E. Cohesion and structure in stage-1 graphite intercalation compounds. *Phys. Rev. B* **1985**, *32*, 2538-2553.

(23) Moriwake, H.; Kuwabara, A.; Fisher, C. A. J.; Ikuhara, Y. Why is sodium-intercalated graphite unstable? *RSC Adv.* **2017**, *7*, 36550-36554.

(24) Kang, Y.-J.; Jung, S. C.; Choi, J. W.; Han, Y.-K. Important Role of Functional Groups for Sodium Ion Intercalation in Expanded Graphite. *Chem. Mater.* **2015**, *27*, 5402-5406.

(25) Abel, P. R.; Fields, M. G.; Heller, A.; Mullins, C. B. Tin–Germanium alloys as anode materials for sodium-ion batteries. *ACS appl. mater. interfaces* **2014**, *6*, 15860-15867.

(26) Wu, L.; Bresser, D.; Buchholz, D.; Giffin, G. A.; Castro, C. R.; Ochel, A.; Passerini, S. Unfolding the mechanism of sodium insertion in anatase TiO_2 nanoparticles. *Adv. Energy Mater.* **2015**, *5*, 1401142-1401152.

(27) Qian, J.; Xiong, Y.; Cao, Y.; Ai, X.; Yang, H. Synergistic Na-storage reactions in Sn_4P_3 as a high-capacity, cycle-stable anode of Na-ion batteries. *Nano Lett.* **2014**, *14*, 1865-1869.

(28) Lu, Y.; Wang, L.; Cheng, J.; Goodenough, J. B. Prussian blue: a new framework of electrode materials for sodium batteries. *Chem. commun.* **2012**, *48*, 6544-6546.

(29) Zhai, Y.; Dou, Y.; Zhao, D.; Fulvio, P. F.; Mayes, R. T.; Dai, S. Carbon materials for chemical capacitive energy storage. *Adv. Mater.* **2011**, *23*, 4828-4850.

(30) Song, H.; Li, N.; Cui, H.; Wang, C. Enhanced storage capability and kinetic processes by pores- and hetero-atoms- riched carbon nanobubbles for lithium-ion and sodium-ion batteries anodes. *Nano Energy* **2014**, *4*, 81-87.

(31) Li, Z.; Jian, Z.; Wang, X.; Rodríguez-Pérez, I. A.; Bommier, C.; Ji, X. Hard carbon anodes of sodium-ion batteries: undervalued rate capability. *Chem.Commun.* **2017**, *53*, 2610-2613.

(32) Liu, H.; Jia, M.; Yue, S.; Cao, B.; Zhu, Q.; Sun, N.; Xu, B. Creative utilization of natural nanocomposites: nitrogen-rich mesoporous carbon for a high-performance sodium ion battery. *J. Mater. Chem. A* **2017**, *5*, 9572-9579.

(33) Muñoz-Márquez, M. Á.; Saurel, D.; Gómez-Cámer, J. L.; Casas-Cabanas, M.; Castillo-Martínez, E.; Rojo, T. Na-Ion batteries for large scale applications: a review on anode materials and solid electrolyte interphase formation. *Adv. Energy Mater.* **2017**, *7*, 1700463-1700493.

(34) Rubanov, S.; Suvorova, A.; Popov, V. P.; Kalinin, A. A.; Pal'yanov, Y. N. Fabrication of graphitic layers in diamond using FIB implantation and high pressure high temperature annealing. *Diam. Relat. Mat.* **2016**, *63*, 143-147.

(35) Franklin, R. E. The structure of graphitic carbons. *Acta crystallogr.* **1951**, *4*, 253-261.

(36) Dahn, J. R.; Zheng, T.; Liu, Y.; Xue, J. Mechanisms for lithium insertion in carbonaceous materials. *Science* **1995**, *270*, 590-593.

(37) Jian, Z.; Bommier, C.; Luo, L.; Li, Z.; Wang, W.; Wang, C.; Greaney, P. A.; Ji, X. Insights on the mechanism of Na-ion storage in soft carbon anode. *Chem. Mater.* **2017**, *29*, 2314-2320.

(38) Franklin, R. E. Crystallite growth in graphitizing and non-graphitizing carbons. *Proc. R. Soc. of London Ser. A-Math. Phys. Eng. Sci.* **1951**, *209*, 196-218.

(39) Lee, K. T.; Lytle, J. C.; Ergang, N. S.; Oh, S. M.; Stein, A. Synthesis and rate performance of monolithic macroporous carbon electrodes for lithium‐ion secondary batteries. *Adv. Funct. Mater.* **2005**, *15*, 547-556.

(40) Al‐Muhtaseb, S. A.; Ritter, J. A. Preparation and properties of resorcinol–formaldehyde organic and carbon gels. *Adv. mater.* **2003**, *15*, 101-114.

(41) Hasegawa, G.; Deguchi, T.; Kanamori, K.; Kobayashi, Y.; Kageyama, H.; Abe, T.; Nakanishi, K. High-Level Doping of Nitrogen, Phosphorus, and Sulfur into Activated Carbon Monoliths and Their Electrochemical Capacitances. *Chem. Mater.* **2015**, *27*, 4703-4712.

(42) Hasegawa, G.; Kanamori, K.; Kannari, N.; Ozaki, J.-i.; Nakanishi, K.; Abe, T. Hard Carbon Anodes for Na-Ion Batteries: Toward a Practical Use. *ChemElectroChem* **2015**, *2*, 1917-1920.

(43) Dahbi, M.; Kiso, M.; Kubota, K.; Horiba, T.; Chafik, T.; Hida, K.; Matsuyama, T.; Komaba, S. Synthesis of hard carbon from argan shells for Na-ion batteries. *J. Mater. Chem. A* **2017**, *5*, 9917-9928.

(44) Zhang, F.; Yao, Y.; Wan, J.; Henderson, D.; Zhang, X.; Hu, L. High temperature carbonized grass as a high performance sodium ion battery anode. *ACS Appl. Mater. Interfaces* **2017**, *9*, 391-397.

(45) Li, H.; Shen, F.; Luo, W.; Dai, J.; Han, X.; Chen, Y.; Yao, Y.; Zhu, H.; Fu, K.; Hitz, E.; Hu, L. Carbonized-leaf membrane with anisotropic surfaces for sodium-ion battery. *ACS Appl. Mater. Interfaces* **2016**, *8*, 2204-2210.

(46) Wang, Q.; Zhu, X.; Liu, Y.; Fang, Y.; Zhou, X.; Bao, J. Rice husk-derived hard carbons as high-performance anode materials for sodium-ion batteries. *Carbon* **2018**, *127*, 658-666.

(47) Li, Y.; Xu, S.; Wu, X.; Yu, J.; Wang, Y.; Hu, Y.-S.; Li, H.; Chen, L.; Huang, X. Amorphous monodispersed hard carbon micro-spherules derived from biomass as a high performance negative electrode material for sodium-ion batteries. *J. Mater. Chem. A* **2015**, *3*, 71-77.

(48) Luo, W.; Shen, F.; Bommier, C.; Zhu, H.; Ji, X.; Hu, L. Na-Ion Battery Anodes: Materials and Electrochemistry. *Acc. Chem. Res.* **2016**, *49*, 231-240.

(49) Metrot, A.; Guerard, D.; Billaud, D.; Herold, A. New results about the sodium-graphite system. *Synth. Met.* **1980**, *1*, 363-369.

(50) Cao, Y.; Xiao, L.; Sushko, M. L.; Wang, W.; Schwenzer, B.; Xiao, J.; Nie, Z.; Saraf, L. V.; Yang, Z.; Liu, J. Sodium ion insertion in hollow carbon nanowires for battery applications. *Nano Lett.* **2012**, *12*, 3783-3787.

(51) Doeff, M. M.; Ma, Y.; Visco, S. J.; De Jonghe, L. C. Electrochemical insertion of sodium into carbon. *J. Electrochem. Soc.* **1993**, *140*, L169-L170.

(52) Stevens, D.; Dahn, J. High capacity anode materials for rechargeable sodium‐ion batteries. *J. Electrochem. Soc.* **2000**, *147*, 1271-1273.

(53) Anji Reddy, M.; Helen, M.; Groß, A.; Fichtner, M.; Euchner, H. Insight into sodium insertion and the storage mechanism in hard carbon. *ACS Energy Lett.* **2018**, *3*, 2851-2857.

(54) Irisarri, E.; Ponrouch, A.; Palacin, M. R. Review-hard carbon negative electrode materials for sodium-ion batteries. *J. Electrochem. Soc.* **2015**, *162*, A2476-A2482.

(55) Ding, J.; Wang, H.; Li, Z.; Kohandehghan, A.; Cui, K.; Xu, Z.; Zahiri, B.; Tan, X.; Lotfabad, E. M.; Olsen, B. C.; Mitlin, D. Carbon nanosheet frameworks derived from peat moss as high performance sodium ion battery anodes. *ACS Nano* **2013**, *7*, 11004-11015.

(56) Lotfabad, E. M.; Ding, J.; Cui, K.; Kohandehghan, A.; Kalisvaart, W. P.; Hazelton, M.; Mitlin, D. High-density sodium and lithium ion battery anodes from banana peels. *ACS Nano* **2014**, *8*, 7115-7129.

(57) Simone, V.; Boulineau, A.; de Geyer, A.; Rouchon, D.; Simonin, L.; Martinet, S. Hard carbon derived from cellulose as anode for sodium ion batteries: Dependence of electrochemical properties on structure. *J. Energy Chem.* **2016**, *25*, 761-768.

(58) Thomas, P.; Billaud, D. Electrochemical insertion of sodium into hard carbons. *Electrochim. Acta* **2002**, *47*, 3303-3307.

(59) Wenzel, S.; Hara, T.; Janek, J.; Adelhelm, P. Room-temperature sodium-ion batteries: improving the rate capability of carbon anode materials by templating strategies. *Energy Environ. Sci.* **2011**, *4*, 3342-3345.

(60) Tang, K.; Fu, L.; White, R. J.; Yu, L.; Titirici, M.-M.; Antonietti, M.; Maier, J. Hollow carbon nanospheres with superior rate capability for sodium-based batteries. *Adv. Energy Mater.* **2012**, *2*, 873-877.

(61) Yang, S.; Feng, X.; Zhi, L.; Cao, Q.; Maier, J.; Mullen, K. Nanographene-constructed hollow carbon spheres and their favorable electroactivity with respect to lithium storage. *Adv. Mater.* **2010**, *22*, 838-842.

(62) Hou, H.; Banks, C. E.; Jing, M.; Zhang, Y.; Ji, X. Carbon Quantum Dots and Their Derivative 3D Porous Carbon Frameworks for Sodium-Ion Batteries with Ultralong Cycle Life. *Adv. Mater.* **2015**, *27*, 7861-7866.

(63) Song, R.; Song, H.; Zhou, J.; Chen, X.; Wu, B.; Yang, H. Y. Hierarchical porous carbon nanosheets and their favorable high-rate performance in lithium ion batteries. *J. Mater. Chem.* **2012**, *22*, 12369-12374.

(64) Prabakar, S. J. R.; Jeong, J.; Pyo, M. Nanoporous hard carbon anodes for improved electrochemical performance in sodium ion batteries. *Electrochim. Acta* **2015**, *161*, 23-31.

(65) Peled, E. The electrochemical behavior of alkali and alkaline earth metals in nonaqueous battery systems—the solid electrolyte interphase model. *J. Electrochem. Soc.* **1979**, *126*, 2047-2051.

(66) Luo, W.; Bommier, C.; Jian, Z.; Li, X.; Carter, R.; Vail, S.; Lu, Y.; Lee, J. J.; Ji, X. Low-surface-area hard carbon anode for Na-ion batteries via graphene oxide as a dehydration agent. *ACS Appl. Mater. Interfaces* **2015**, *7*, 2626-2631.

(67) Shen, F.; Zhu, H.; Luo, W.; Wan, J.; Zhou, L.; Dai, J.; Zhao, B.; Han, X.; Fu, K.; Hu, L. Chemically crushed wood cellulose fiber towards high-performance sodium-ion batteries. *ACS Appl. Mater. Interfaces* **2015**, *7*, 23291-23296.

(68) Luo, W.; Schardt, J.; Bommier, C.; Wang, B.; Razink, J.; Simonsen, J.; Ji, X. Carbon nanofibers derived from cellulose nanofibers as a long-life anode material for rechargeable sodium-ion batteries. *J. Mater. Chem. A* **2013**, *1*, 10662-10666.

(69) Li, Y.; Hu, Y.-S.; Titirici, M.-M.; Chen, L.; Huang, X. Hard carbon microtubes made from renewable cotton as high-performance anode material for sodium-ion batteries. *Adv. Energy Mater.* **2016**, *6*, 1600659-1600667.

(70) Zhang, Y.; Chen, L.; Meng, Y.; Xie, J.; Guo, Y.; Xiao, D. Lithium and sodium storage in highly ordered mesoporous nitrogen-doped carbons derived from honey. *J. Power Sources* **2016**, *335*, 20-30.

(71) Qin, D.; Zhang, F.; Dong, S.; Zhao, Y.; Xu, G.; Zhang, X. Analogous graphite carbon sheets derived from corn stalks as high performance sodium-ion battery anodes. *RSC Adv.* **2016**, *6*, 106218-106224.

(72) Ren, X.; Xu, S.-D.; Liu, S.; Chen, L.; Zhang, D.; Qiu, L. Lath-shaped biomass derived hard carbon as anode materials with super rate capability for sodium-ion batteries. *J. Electroanal. Chem.* **2019**, *841*, 63-72.

(73) Wang, P.; Zhu, K.; Ye, K.; Gong, Z.; Liu, R.; Cheng, K.; Wang, G.; Yan, J.; Cao, D. Three-dimensional biomass derived hard carbon with reconstructed surface as a free-standing anode for sodium-ion batteries. *J. Colloid Interface Sci.* **2020**, *561*, 203-210.

(74) Wu, F.; Zhang, M.; Bai, Y.; Wang, X.; Dong, R.; Wu, C. Lotus seedpod-derived hard carbon with hierarchical porous structure as stable anode for sodium-ion batteries. *ACS Appl. Mater. Interfaces* **2019**, *11*, 12554-12561.

(75) Wang, K.; Jin, Y.; Sun, S.; Huang, Y.; Peng, J.; Luo, J.; Zhang, Q.; Qiu, Y.; Fang, C.; Han, J. Low-cost and high-performance hard carbon anode materials for sodium-ion batteries. *ACS Omega* **2017**, *2*, 1687-1695.

(76) Stevens, D. A.; Dahn, J. R. An in situ small-angle X-ray scattering study of sodium insertion into a nanoporous carbon anode material within an operating electrochemical cell. *J. Electrochem. Soc.* **2000**, *147*, 4428-4431.

(77) Stevens, D.; Dahn, J. The mechanisms of lithium and sodium insertion in carbon materials. *J. Electrochem. Soc.* **2001**, *148*, A803-A811.

(78) Komaba, S.; Murata, W.; Ishikawa, T.; Yabuuchi, N.; Ozeki, T.; Nakayama, T.; Ogata, A.; Gotoh, K.; Fujiwara, K. Electrochemical Na insertion and solid electrolyte interphase for hard-carbon electrodes and application to Na-ion batteries. *Adv. Funct. Mater.* **2011**, *21*, 3859-3867.

(79) Nagao, M.; Pitteloud, C.; Kamiyama, T.; Otomo, T.; Itoh, K.; Fukunaga, T.; Tatsumi, K.; Kanno, R. Structure characterization and lithiation mechanism of nongraphitized carbon for lithium secondary batteries. *J. Electrochem. Soc.* **2006**, *153*, A914-A919.

(80) Au, H.; Alptekin, H.; Jensen, A. C. S.; Olsson, E.; O'Keefe, C. A.; Smith, T.; Crespo-Ribadeneyra, M.; Headen, T. F.; Grey, C. P.; Cai, Q.; Drew, A. J.; Titirici, M.-M. A revised mechanistic model for sodium insertion in hard carbons. *Energy Environ. Sci.* **2020**, *13*, 3469-3479.

(81) Gotoh, K.; Ishikawa, T.; Shimadzu, S.; Yabuuchi, N.; Komaba, S.; Takeda, K.; Goto, A.; Deguchi, K.; Ohki, S.; Hashi, K.; Shimizu, T.; Ishida, H. NMR study for electrochemically inserted Na in hard carbon electrode of sodium ion battery. *J. Power Sources* **2013**, *225*, 137-140.

(82) Morita, R.; Gotoh, K.; Kubota, K.; Komaba, S.; Hashi, K.; Shimizu, T.; Ishida, H. Correlation of carbonization condition with metallic property of sodium clusters formed in hard carbon studied using 23Na nuclear magnetic resonance. *Carbon* **2019**, *145*, 712-715.

(83) Dahbi, M.; Yabuuchi, N.; Kubota, K.; Tokiwa, K.; Komaba, S. Negative electrodes for Na-ion batteries. *Phys. Chem. Chem. Phys.* **2014**, *16*, 15007-15028.

(84) Bommier, C.; Surta, T. W.; Dolgos, M.; Ji, X. New mechanistic insights on Na-ion storage in nongraphitizable carbon. *Nano letters* **2015**, *15*, 5888-5892.

(85) Oyama, S. T. Crystal structure and chemical reactivity of transition metal carbides and nitrides. *J. Solid State Chem.* **1992**, *96*, 442-445.

(86) Chemler, S. R.; Bovino, M. T. Catalytic aminohalogenation of alkenes and alkynes. *ACS Catal.* **2013**, *3*, 1076-1091.

(87) Toth, L.: *Transition metal carbides and nitrides*; Elsevier, 2014.

(88) Siegel, E. d-Bandwidth contraction upon metalloid formation: a resolution of the bonding controversy in transition metal carbides, nitrides and borides. *Semicond. Insul.* **1979**, *5*, 47-60.

(89) Chen, J. G. Carbide and Nitride Overlayers on Early Transition Metal Surfaces: Preparation, Characterization, and Reactivities. *Chem. Rev.* **1996**, *96*, 1477-1498.

(90) Cabana, J.; Monconduit, L.; Larcher, D.; Palacin, M. R. Beyond intercalation-based Li-ion batteries: the state of the art and challenges of electrode materials reacting through conversion reactions. *Adv. Mater.* **2010**, *22*, 170-192.

(91) Bates, J.; Dudney, N.; Neudecker, B.; Ueda, A.; Evans, C. Thin-film lithium and lithium-ion batteries. *Solid state ionics* **2000**, *135*, 33-45.

(92) Pereira, N.; Klein, L.; Amatucci, G. The Electrochemistry of Zn_3N_2 and LiZnN A lithium reaction mechanism for metal nitride electrodes. *J. Electrochem. Soc.* **2002**, *149*, A262-A271.

(93) Balogun, M.-S.; Yu, M.; Huang, Y.; Li, C.; Fang, P.; Liu, Y.; Lu, X.; Tong, Y. Binder-free Fe_2N nanoparticles on carbon textile with high power density as novel anode for high-performance flexible lithium ion batteries. *Nano Energy* **2015**, *11*, 348-355.

(94) Sun, Q.; Fu, Z.-W. Vanadium nitride as a novel thin film anode material for rechargeable lithium batteries. *Electrochim. Acta* **2008**, *54*, 403-409.

(95) Dong, Y.; Wang, B.; Zhao, K.; Yu, Y.; Wang, X.; Mai, L.; Jin, S. Air-stable porous Fe_2N encapsulated in carbon microboxes with high volumetric lithium storage capacity and a long cycle life. *Nano Lett.* **2017**, *17*, 5740-5746.

(96) Balogun, M.-S.; Zeng, Y.; Qiu, W.; Luo, Y.; Onasanya, A.; Olaniyi, T. K.; Tong, Y. Three-dimensional nickel nitride (Ni_3N) nanosheets: free standing and flexible electrodes for lithium ion batteries and supercapacitors. *J. Mater. Chem. A* **2016**, *4*, 9844-9849.

(97) Zhang, M.; Qiu, Y.; Han, Y.; Guo, Y.; Cheng, F. Three-dimensional tungsten nitride nanowires as high performance anode material for lithium ion batteries. *J. Power Sources* **2016**, *322*, 163-168.

(98) Deng, M.; Qi, J.; Li, X.; Xiao, Y.; Yang, L.; Yu, X.; Wang, H.; Yuan, B.; Gao, Q. MoC/C nanowires as high-rate and long cyclic life anode for lithium ion batteries. *Electrochim. Acta* **2018**, *277*, 205-210.

(99) Ghidiu, M.; Lukatskaya, M. R.; Zhao, M. Q.; Gogotsi, Y.; Barsoum, M. W. Conductive two-dimensional titanium carbide 'clay' with high volumetric capacitance. *Nature* **2014**, *516*, 78-81.

(100) Alhabeb, M.; Maleski, K.; Anasori, B.; Lelyukh, P.; Clark, L.; Sin, S.; Gogotsi, Y. Guidelines for synthesis and processing of two-dimensional titanium carbide ($Ti_3C_2T_x$ MXene). *Chem. Mater.* **2017**, *29*, 7633-7644.

(101) Naguib, M.; Kurtoglu, M.; Presser, V.; Lu, J.; Niu, J.; Heon, M.; Hultman, L.; Gogotsi, Y.; Barsoum, M. W. Two-dimensional nanocrystals produced by exfoliation of Ti_3AlC_2. *Adv. Mater.* **2011**, *23*, 4248-4253.

(102) Tang, Q.; Zhou, Z.; Shen, P. Are MXenes promising anode materials for Li ion batteries? computational studies on electronic properties and Li storage capability of Ti_3C_2 and $Ti_3C_2X_2$ (X = F, OH) monolayer. *J. Am. Chem. Soc.* **2012**, *134*, 16909-16916.

(103) Mashtalir, O.; Naguib, M.; Mochalin, V. N.; Dall'Agnese, Y.; Heon, M.; Barsoum, M. W.; Gogotsi, Y. Intercalation and delamination of layered carbides and carbonitrides. *Nat. Commun.* **2013**, *4*, 1716-1722.

(104) Zhang, S.; Li, X. Y.; Yang, W.; Tian, H.; Han, Z.; Ying, H.; Wang, G.; Han, W. Q. Novel synthesis of red phosphorus nanodot/$Ti_3C_2T_x$ MXenes from low-cost Ti_3SiC_2 MAX phases for superior lithium- and sodium-ion batteries. *ACS Appl. Mater. Interfaces* **2019**, *11*, 42086-42093.

(105) Li, X.; Hasan, M. M.; Hector, A. L.; Owen, J. R. Performance of nanocrystalline Ni_3N as a negative electrode for sodium-ion batteries. *J. Mater. Chem. A* **2013**, *1*, 6441-6445.

(106) Li, X.; Hector, A. L.; Owen, J. R. Evaluation of Cu_3N and CuO as negative electrode materials for sodium batteries. *J. Phys. Chem. C* **2014**, *118*, 29568-29573.

(107) Cui, Z.; Li, C.; Yu, P.; Yang, M.; Guo, X.; Yin, C. Reaction pathway and wiring network dependent Li/Na storage of micro-sized conversion anode with mesoporosity and metallic conductivity. *J. Mater. Chem. A* **2015**, *3*, 509-514.

(108) Zu, C.-X.; Li, H. Thermodynamic analysis on energy densities of batteries. *Energy Environ. Sci.* **2011**, *4*, 2614-2624.

(109) Liu, S.; Liu, J.; Wang, W.; Yang, L.; Zhu, K.; Wang, H. Synthesis of coral-like Fe_2N@C nanoparticles and application in sodium ion batteries as a novel anode electrode material. *RSC Adv.* **2016**, *6*, 86131-86136.

(110) Yuan, J.; Hu, X.; Chen, J.; Liu, Y.; Huang, T.; Wen, Z. In situ formation of vanadium nitride quantum dots on N-doped carbon hollow spheres for superior lithium and sodium storage. *J. Mater. Chem. A* **2019**, *7*, 9289-9296.

(111) Wang, L.; Sun, J.; Song, R.; Yang, S.; Song, H. Hybrid 2D-0D graphene-VN quantum dots for superior lithium and sodium storage. *Adv. Energy Mater.* **2016**, *6*, 1502067-1502073.

(112) Li, Z.; Fang, Y.; Zhang, J.; Lou, X. W. D. Necklace-Like structures composed of Fe_3N@C yolk-shell particles as an advanced anode for sodium-ion batteries. *Adv. Mater.* **2018**, *30*, 1800525-1800529.

(113) Fu, Z.-W.; Wang, Y.; Yue, X.-L.; Zhao, S.-L.; Qin, Q.-Z. Electrochemical Reactions of Lithium with Transition Metal Nitride Electrodes. *J. Phys. Chem. B* **2004**, *108*, 2236-2244.

(114) Yu, P.; Wang, L.; Sun, F.; Zhao, D.; Tian, C.; Zhao, L.; Liu, X.; Wang, J.; Fu, H. Three-dimensional Fe_2N@C microspheres grown on reduced graphite oxide for lithium-ion batteries and the Li storage mechanism. *Chem. -A Eur. J.* **2015**, *21*, 3249-3256.

(115) Vadahanambi, S.; Park, H. Carbon sheathed molybdenum nitride nanoparticles anchored on reduced graphene oxide as high-capacity sodium-ion battery anodes and supercapacitors. *New J. Chem.* **2018**, *42*, 5668-5673.

(116) Çakır, D.; Sevik, C.; Gülseren, O.; Peeters, F. M. Mo_2C as a high capacity anode material: a first-principles study. *J. Mater. Chem. A* **2016**, *4*, 6029-6035.

(117) Sun, Q.; Dai, Y.; Ma, Y.; Jing, T.; Wei, W.; Huang, B. Ab Initio prediction and characterization of Mo_2C monolayer as anodes for lithium-ion and sodium-ion batteries. *J. Phys. Chem. Lett.* **2016**, *7*, 937-943.

(118) Lv, X.; Song, J.; Lai, Y.; Fang, J.; Li, J.; Zhang, Z. Ultrafine nanoparticles assembled Mo_2C nanoplates as promising anode materials for sodium ion batteries with excellent performance. *J. Energy Storage* **2016**, *8*, 205-211.

(119) Liao, H.; Hou, H.; Zhang, Y.; Qiu, X.; Ji, X. Nano-confined Mo_2C particles embedded in a porous carbon matrix: a promising anode for ultra-stable Na storage. *ChemElectroChem* **2017**, *4*, 2669-2676.

(120) Li, L.; Chen, Z.; Zhang, M. Mo2C embedded in S-doped carbon nanofibers for high-rate performance and long-life time Na-ion batteries. *Solid State Ion.* **2018**, *323*, 151-156.

(121) Li, X.; Deng, M.; Zhang, W.; Gao, Q.; Wang, H.; Yuan, B.; Yang, L.; Zhu, M. Mo_2C/N-doped carbon nanowires as anode materials for sodium-ion batteries. *Mater. Lett.* **2017**, *194*, 30-33.

(122) Balogun, M.-S.; Yu, M.; Li, C.; Zhai, T.; Liu, Y.; Lu, X.; Tong, Y. Facile synthesis of titanium nitride nanowires on carbon fabric for flexible and high-rate lithium ion batteries. *J. Mater. Chem. A* **2014**, *2*, 10825-10829.

(123) Li, X.; Hector, A. L.; Owen, J. R.; Shah, S. I. U. Evaluation of nanocrystalline Sn_3N_4 derived from ammonolysis of $Sn(NEt_2)_4$ as a negative electrode material for Li-ion and Na-ion batteries. *J. Mater. Chem. A* **2016**, *4*, 5081-5087.

(124) Shah, S. I. U.; Hector, A. L.; Li, X.; Owen, J. R. Solvothermal synthesis and electrochemical charge storage assessment of Mn_3N_2. *J. Mater. Chem. A* **2015**, *3*, 3612-3619.

(125) Toby, B. H. EXPGUI, a graphical user interface for GSAS. *J. Appl. Crystallogr.* **2001**, *34*, 210-213.

(126) Sadezky, A.; Muckenhuber, H.; Grothe, H.; Niessner, R.; Poeschl, U. Raman microspectroscopy of soot and related carbonaceous materials. spectral analysis and structural information. *Carbon* **2005**, *43*, 1731-1742.

(127) Lesiak, B.; Kövér, L.; Tóth, J.; Zemek, J.; Jiricek, P.; Kromka, A.; Rangam, N. C sp2/sp3 hybridisations in carbon nanomaterials – XPS and (X)AES study. *Appl. Surf. Sci.* **2018**, *452*, 223-231.

(128) Shirley, D. A. High-resolution X-ray photoemission spectrum of the valence bands of gold. *Phys. Rev. B* **1972**, *5*, 4709-4714.

(129) Alothman, Z. A review: fundamental aspects of silicate mesoporous materials. *Materials* **2012**, *5*, 2874-2902.

(130) Xiao, B.; Rojo, T.; Li, X. Hard carbon as sodium-ion battery anodes: progress and challenges. *ChemSusChem* **2019**, *12*, 133-144.

(131) Hon, D. N. S.; Editor: *Chemical modification of lignocellulosic materials*; Dekker, 1996. pp. 2-3.

(132) Gupta, A.; Dhakate, S. R.; Pal, P.; Dey, A.; Iyer, P. K.; Singh, D. K. Effect of graphitization temperature on structure and electrical conductivity of poly-acrylonitrile based carbon fibers. *Diam. Relat. Mat.* **2017**, *78*, 31-38.

(133) Sing, K. S. W.; Everett, D. H.; Haul, R. A. W.; Moscou, L.; Pierotti, R. A.; Rouquerol, J.; Siemieniewska, T. Reporting physisorption data for gas/solid systems with special reference to the determination of srface area and porosity. *Pure Appl. Chem.* **1985**, *57*, 603-619.

(134) Puziy, A. M.; Poddubnaya, O. I.; Martinez-Alonso, A.; Suarez-Garcia, F.; Tascon, J. M. D. Synthetic carbons activated with phosphoric acid II. porous structure. *Carbon* **2002**, *40*, 1507-1519.

(135) Tseng, R.-L.; Tseng, S.-K. Pore structure and adsorption performance of the KOH-activated carbons prepared from corncob. *J. Colloid Interface Sci.* **2005**, *287*, 428-437.

(136) Park, S. S.; Chu, S.-W.; Xue, C.; Zhao, D.; Ha, C.-S. Facile synthesis of mesoporous carbon nitrides using the incipient wetness method and the application as hydrogen adsorbent. *J. Mater. Chem* **2011**, *21*, 10801-10807.

(137) Ponrouch, A.; Goñi, A. R.; Palacín, M. R. High capacity hard carbon anodes for sodium ion batteries in additive free electrolyte. *Electrochem. Commun.* **2013**, *27*, 85-88.

(138) Ponrouch, A.; Dedryvère, R.; Monti, D.; Demet, A. E.; Ateba Mba, J. M.; Croguennec, L.; Masquelier, C.; Johansson, P.; Palacín, M. R. Towards high energy density sodium ion batteries through electrolyte optimization. *Energy Environ. Sci.* **2013**, *6*, 2361.

(139) Monti, D.; Ponrouch, A.; Palacín, M. R.; Johansson, P. Towards safer sodium-ion batteries via organic solvent/ionic liquid based hybrid electrolytes. *J. Power Sources* **2016**, *324*, 712-721.

(140) Jiang, Q.; Li, G.; Gao, X. Highly ordered TiN nanotube arrays as counter electrodes for dye-sensitized solar cells. *Chem. commun.* **2009**, 6720-6722.

(141) Patsalas, P.; Kalfagiannis, N.; Kassavetis, S. Optical Properties and Plasmonic Performance of Titanium Nitride. *Materials* **2015**, *8*, 3128-3154.

(142) Yousef, A.; Brooks, R. M.; El-Newehy, M. H.; Al-Deyab, S. S.; Kim, H. Y. Electrospun Co-TiC Nanoparticles Embedded on Carbon Nanofibers: Active and Chemically Stable Counter Electrode for Methanol Fuel Cells and Dye-sensitized Solar Cells. *Int. J. Hydrogen Energy* **2017**, *42*, 10407-10415.

(143) Zhang, J.; Hector, A. L.; Soulé, S.; Zhang, Q.; Zhao, X. Effects of Ammonolysis and of Sol–gel Titanium Oxide Nitride Coating on Carbon Fibres for Use in Flexible Supercapacitors. *J. Mater. Chem. A* **2018**, *6*, 5208-5216.

(144) Yu, Z.-L.; Xin, S.; You, Y.; Yu, L.; Lin, Y.; Xu, D.-W.; Qiao, C.; Huang, Z.-H.; Yang, N.; Yu, S.-H.; Goodenough, J. B. Ion-catalyzed synthesis of microporous hard carbon embedded with expanded nanographite for enhanced lithium/sodium storage. *J. Am. Chem. Soc.* **2016**, *138*, 14915-14922.

(145) Wen, Y.; He, K.; Zhu, Y.; Han, F.; Xu, Y.; Matsuda, I.; Ishii, Y.; Cumings, J.; Wang, C. Expanded Graphite as Superior Anode for Sodium-ion Batteries. *Nat. Commun.* **2014**, *5*, 4033.

(146) Yu, W.; Yu, T.; Graham, N. Development of a Stable Cation Modified Graphene Oxide Membrane for Water Treatment. *2D Mater.* **2017**, *4*, 045006.

(147) Inorg. Cryst. Struct. Database (ICSD, Fiz Karlsruhe) Accessed via EPSRC-funded Natl. Chem. Database Serv. hosted by R. Soc. Chem.

(148) Elliott, R. O.; Kempter, C. P. Thermal Expansion of Some Transition Metal Carbides. *J. Phys. Chem.* **1958**, *62*, 630-631.

(149) Pessall, N.; Gold, R. E.; Johansen, H. A. Superconductivity in Interstitial Compounds. *J. Phys. Chem. Solids* **1968**, *29*, 19-38.

(150) Stuart, H.; Ridley, N. Thermal Expansion of Some Carbides and Tessellated Stresses in Steels. *J. Iron Steel Inst.* **1970**, *208*, 1087-1092.

(151) Kieffer, R.; Nowotny, H.; Ettmayer, P.; Dufek, G. Miscibility of Transition Metal Nitrides and Carbides. *Metall* **1972**, *26*, 701-708.

(152) Rogl, P.; Naik, S. K.; Rudy, E. A Constitutional Diagram of the System Titanium Carbide-hafnium Carbide-tungsten Carbide. *Monatsh. Chem.* **1977**, *108*, 1189-1211.

(153) Bannister, F. A. Osbornite, meteoritic titanium nitride. *Mineral. Mag. J. Mineral. Soc.* **1941**, *26*, 36-44.

(154) Duwez, P.; Odell, F. Phase Relationships in the Binary Systems of Nitrides and Carbides of Zirconium, Niobium, Titanium, and Vanadium. *J. Electrochem. Soc.* **1950**, *97*, 299-304.

(155) Nowotny, H.; Benesovsky, F.; Rudy, E. High-melting Systems of Hafnium Carbide and Hafnium Nitride. *Monatsh. Chem.* **1960**, *91*, 348-356.

(156) Gatterer, J.; Dufek, G.; Ettmayer, P.; Kieffer, R. Cubic Tantalum Mononitride (B1) and Its Miscibility with the Transition Metal Nitrides and Carbide isotypes. *Monatsh. Chem.* **1975**, *106*, 1137-1147.

(157) Hasegawa, M.; Yagi, T. Systematic Study of Formation and Crystal Structure of 3d-transition Metal Nitrides Synthesized in a Supercritical Nitrogen Fluid under 10 GPa and 1800 K Using Diamond Anvil Cell and YAG Laser Heating. *J. Alloys Compd.* **2005**, *403*, 131-142.

(158) Rostoker, W. Observations on the Lattice Parameters of the α and TiO Phases in the Titanium-oxygen System. *J. Met.* **1952**, *4*, 981-982.

(159) Straumanis, M. E. Absorption Correction in Precision Determination of Lattice Parameters. *J. Appl. Phys.* **1959**, *30*, 1965-1969.

(160) Hilti, E. New Phases in the Titanium-oxygen System. *Naturwissenschaften* **1968**, *55*, 130-131.

(161) Banus, M. D.; Reed, T. B.; Strauss, A. J. Electrical and Magnetic Properties of TiO and VO. *Phys. Rev. B* **1972**, *5*, 2775-2784.

(162) Taylor, D. Thermal Expansion Data: 1. Binary Oxides with the Sodium Chloride and Wurtzite Structures, MO. *Trans. J. Br. Ceram. Soc.* **1984**, *83*, 5.

(163) Fechler, N.; Fellinger, T.-P.; Antonietti, M. Template-free One-pot Synthesis of Porous Binary and Ternary Metal Nitride@N-doped Carbon Composites from Ionic Liquids. *Chem. Mater.* **2012**, *24*, 713-719.

(164) Matenoglou, G. M.; Zoubos, H.; Lotsari, A.; Lekka, C. E.; Komninou, P.; Dimitrakopulos, G. P.; Kosmidis, C.; Evangelakis, G. A.; Patsalas, P. Metal-containing Amorphous Carbon (a-C:Ag) and AlN (AlN:Ag) Metallo-dielectric Nanocomposites. *Thin Solid Films* **2009**, *518*, 1508-1511.

(165) Tembre, A.; Henocque, J.; Clin, M. Infrared and raman spectroscopic study of carbon-cobalt composites. *Int. J. Spectrosc.* **2011**, *2011*, 186471-186476.

(166) Leiro, J. A.; Heinonen, M. H.; Laiho, T.; Batirev, I. G. Core-level XPS Spectra of Fullerene, Highly Oriented Pyrolitic Graphite, and Glassy Carbon. *J. Electron Spectrosc.* **2003**, *128*, 205-213.

(167) Lee, D. W.; Seo, J. W. sp2/sp3 carbon ratio in graphite oxide with different preparation times. *J. Phys. Chem. C* **2011**, *115*, 2705-2708.

(168) Luthin, J.; Linsmeier, C. Characterization of Electron Beam Evaporated Carbon Films and Compound Formation on Titanium and Silicon. *Phys. Scr., T* **2001**, *T91*, 134-137.

(169) Didziulis, S. V.; Frantz, P.; Perry, S. S.; El-Bjeirami, O.; Imaduddin, S.; Merrill, P. B. Substrate-dependent Reactivity of Water on Metal Carbide Surfaces. *J. Phys. Chem. B* **1999**, *103*, 11129-11140.

(170) Esaka, F.; Furuya, K.; Shimada, H.; Imamura, M.; Matsubayashi, N.; Sato, H.; Nishijima, A.; Kawana, A.; Ichimura, H.; Kikuchi, T. Comparison of Surface Oxidation of Titanium Nitride and Chromium Nitride Films Studied by x-ray Absorption and Photoelectron Spectroscopy. *J. Vac. Sci. Tech.* **1997**, *15*, 2521-2528.

(171) Heide, N.; Siemensmeyer, B.; Schultze, J. W. Surface Characterization and Electrochemical Behavior of Nitrogen- and Carbon-implanted Titanium. *Surf. Interface Anal.* **1992**, *19*, 423-429.

(172) Milosev, I.; Strehblow, H. H.; Navinsek, B.; Metikos-Hukovic, M. Electrochemical and Thermal Oxidation of TiN Coatings Studied by XPS. *Surf. Interface Anal.* **1995**, *23*, 529-539.

(173) Gaddam, R. R.; Jiang, E.; Amiralian, N.; Annamalai, P. K.; Martin, D. J.; Kumar, N. A.; Zhao, X. S. Spinifex Nanocellulose Derived Hard Carbon Anodes for High-performance Sodium-ion Batteries. *Sustain. Energ. Fuels* **2017**, *1*, 1090-1097.

(174) Biesinger, M. C.; Lau, L. W. M.; Gerson, A. R.; Smart, R. S. C. Resolving Surface Chemical States in XPS Analysis of First Row Transition Metals, Oxides and Hydroxides: Sc, Ti, V, Cu and Zn. *Appl. Surf. Sci.* **2010**, *257*, 887-898.

(175) Gray, B. M.; Hector, A. L.; Jura, M.; Owen, J. R.; Whittam, J. Effect of Oxidative Surface Treatments on Charge Storage at Titanium Nitride Surfaces for Supercapacitor Applications. *J. Mater. Chem. A* **2017**, *5*, 4550-4559.

(176) Cheng, H.; Ye, J. W.; Sun, Y.; Yuan, W. J.; Tian, J. Y.; Bogale, R. F.; Tian, P.; Ning, G. L. Template-induced Synthesis and Superior Antibacterial Activity of Hierarchical Ag/TiO_2 Composites. *Rsc Adv.* **2015**, *5*, 80668-80676.

(177) Li, H.; Wang, Q.; Shi, L.; Chen, L.; Huang, X. Nanosized SnSb Alloy Pinning on Hard Non-graphitic Carbon Spherules as Anode Materials for a Li Ion Battery. *Chem. Mater.* **2002**, *14*, 103-108.

(178) Wang, Y.; Fu, Z.-W.; Yue, X.-L.; Qin, Q.-Z. Electrochemical Reactivity Mechanism of Ni_3N with Lithium. *J. Electrochem. Soc.* **2004**, *151*, E162.

(179) Ghimire, P. C.; Schweiss, R.; Scherer, G. G.; Wai, N.; Lim, T. M.; Bhattarai, A.; Nguyen, T. D.; Yan, Q. Titanium Carbide-decorated Graphite Felt as High Performance Negative Electrode in Vanadium Redox Flow Batteries. *J. Mater. Chem. A* **2018**, *6*, 6625-6632.

(180) Cao, S.; Xue, Z.; Yang, C.; Qin, J.; Zhang, L.; Yu, P.; Wang, S.; Zhao, Y.; Zhang, X.; Liu, R. Insights into the Li^+ Storage Mechanism of TiC@C-TiO_2 Core-shell Nanostructures as High Performance Anodes. *Nano Energy* **2018**, *50*, 25-34.

(181) Park, J.; Jun, Y.-S.; Lee, W.-r.; Gerbec, J. A.; See, K. A.; Stucky, G. D. Bimodal Mesoporous Titanium Nitride/Carbon Microfibers as Efficient and Stable Electrocatalysts for Li–O_2 Batteries. *Chem. Mater.* **2013**, *25*, 3779-3781.

(182) Liu, Y.; Liu, L.; Kong, L.; Kang, L.; Ran, F. Supercapacitor Electrode Based on Nano-vanadium Nitride Incorporated on Porous Carbon Nanospheres Derived from Ionic Amphiphilic Block Copolymers & Vanadium-contained Ion Assembly Systems. *Electrochim. Acta* **2016**, *211*, 469-477.

(183) Wei, S.; Wang, C.; Chen, S.; Zhang, P.; Zhu, K.; Wu, C.; Song, P.; Wen, W.; Song, L. Dial the mechanism switch of VN from conversion to intercalation toward long cycling sodium-ion battery. *Adv. Energy Mater.* **2020**, 1903712-1903719.

(184) Cheng, H.; Garcia-Araez, N.; Hector, A. L.; Soule, S. Synthesis of hard carbon-TiN/TiC composites by reacting cellulose with $TiCl_4$ followed by carbothermal nitridation/reduction. *Inorg. Chem.* **2019**, *58*, 5776-5786.

(185) Jawhari, T.; Roid, A.; Casado, J. Raman spectroscopic characterization of some commercially available carbon black materials. *Carbon* **1995**, *33*, 1561-1565.

(186) Choi, D.; Blomgren, G. E.; Kumta, P. N. Fast and reversible surface redox reaction in nanocrystalline vanadium nitride supercapacitors. *Adv. Mater.* **2006**, *18*, 1178-1182.

(187) Kafizas, A.; Hyett, G.; Parkin, I. P. Combinatorial atmospheric pressure chemical vapour deposition (cAPCVD) of a mixed vanadium oxide and vanadium oxynitride thin film. *J. Mater. Chem.* **2009**, *19*, 1399-1408.

(188) Zielke, U.; Huettinger, K. J.; Hoffman, W. P. Surface-oxidized carbon fibers: I. surface structure and chemistry. *Carbon* **1996**, *34*, 983-998.

(189) Lakshminarayanan, P. V.; Toghiani, H.; Pittman, C. U. Nitric acid oxidation of vapor grown carbon nanofibers. *Carbon* **2004**, *42*, 2433-2442.

(190) Zhao, Z.; Liu, Y.; Cao, H.; Ye, J.; Gao, S.; Tu, M. Synthesis of VN nanopowders by thermal nitridation of the precursor and their characterization. *J. Alloy. Compd.* **2008**, *464*, 75-80.

(191) Indlekofer, G.; Mariot, J. M.; Lengauer, W.; Beauprez, E.; Oelhafen, P.; Hague, C. F. Electronic structure of stoichiometric and substoichiometric vanadium nitride from photoelectron spectroscopy. *Solid State Commun.* **1989**, *72*, 419-423.

(192) Glaser, A.; Surnev, S.; Netzer, F. P.; Fateh, N.; Fontalvo, G. A.; Mitterer, C. Oxidation of vanadium nitride and titanium nitride coatings. *Surf. Sci.* **2007**, *601*, 1153-1159.

(193) Ghimbeu, C. M.; Raymundo-Piñero, E.; Fioux, P.; Béguin, F.; Vix-Guterl, C. Vanadium nitride/carbon nanotube nanocomposites as electrodes for supercapacitors. *J. Mater. Chem.* **2011**, *21*, 13268-13275.

(194) Vannerberg, N. G. The ESCA-spectra of sodium and potassium cyanide and of the sodium and potassium salts of the hexacyanometallates of the first transition metal series. *Chem. Scr.* **1976**, *9*, 122-126.

(195) Memarzadeh Lotfabad, E.; Kalisvaart, P.; Kohandehghan, A.; Karpuzov, D.; Mitlin, D. Origin of non-SEI related coulombic efficiency loss in carbons tested against Na and Li. *J. Mater. Chem. A* **2014**, *2*, 19685-19695.

(196) Bommier, C.; Leonard, D.; Jian, Z.; Stickle, W. F.; Greaney, P. A.; Ji, X. New paradigms on the nature of solid electrolyte interphase formation and capacity fading of hard carbon anodes in Na-ion batteries. *Adv. Mater. Interfaces* **2016**, *3*, 1600449-1600458.

(197) Rostoker, W.; Yamamoto, A. A survey of vanadium binary systems. *Trans. Am. Soc. Met.* **1954**, *46*, 1136-1167.

(198) Xie, F.; Xu, Z.; Jensen, A. C. S.; Au, H.; Lu, Y.; Araullo-Peters, V.; Drew, A. J.; Hu, Y. S.; Titirici, M. M. Hard–soft carbon composite anodes with synergistic sodium storage performance. *Adv. Funct. Mater.* **2019**, *29*, 1901072-1901080.

(199) Zhang, X.; Pan, G.; Li, G.; Qu, J.; Gao, X. Si–Si_3N_4 composites as anode materials for lithium ion batteries. *Solid State Ion.* **2007**, *178*, 1107-1112.

(200) Suzuki, N.; Cervera, R. B.; Ohnishi, T.; Takada, K. Silicon nitride thin film electrode for lithium-ion batteries. *J. Power Sources* **2013**, *231*, 186-189.

(201) Yang, J.; de Guzman, R. C.; Salley, S. O.; Ng, K. Y. S.; Chen, B.-H.; Cheng, M. M.-C. Plasma enhanced chemical vapor deposition silicon nitride for a high-performance lithium ion battery anode. *J. Power Sources* **2014**, *269*, 520-525.

(202) Weinberger, M.; Pfeifer, C.; Schindler, S.; Diemant, T.; Behm, R. J.; Wohlfahrt-Mehrens, M. Submicron-sized silicon oxycarbide spheres as anodes for alkali ion batteries. *J. Mater. Chem. A* **2015**, *3*, 23707-23715.

(203) Chandra, C.; Kim, J. Silicon oxycarbide produced from silicone oil for high-performance anode material in sodium ion batteries. *Chem. Engineer. J.* **2018**, *338*, 126-136.

(204) Dou, X.; Buchholz, D.; Weinberger, M.; Diemant, T.; Kaus, M.; Indris, S.; Behm, R. J.; Wohlfahrt-Mehrens, M.; Passerini, S. Study of the Na storage mechanism in silicon oxycarbide—evidence for reversible silicon redox activity. *Small Methods* **2018**, *3*, 1800177-1800185.

(205) Chandra, C.; Cahyadi, H. S.; Alvin, S.; Devina, W.; Park, J.-H.; Chang, W.; Chung, K. Y.; Kwak, S. K.; Kim, J. Revealing the sodium storage mechanism in high-temperature-synthesized silicon oxycarbides. *Chem. Mater.* **2019**, 410-423.

(206) Hector, A. L. Synthesis and processing of silicon nitride and related materials using preceramic polymer and non-oxide sol-gel approaches. *Coord. Chem. Rev.* **2016**, *323*, 120-137.

(207) Seher, M.; Bill, J.; Aldinger, F.; Riedel, R. Crystallization kinetics of polysilazane-derived amorphous silicon nitride. *J. Cryst. Growth* **1994**, *137*, 452-456.

(208) Castanho, S. M.; Moreno, R.; Fierro, J. L. G. Influence of process conditions on the surface oxidation of silicon nitride green compacts. *J. Mater. Sci.* **1997**, *32*, 157-162.

(209) Foti, G. Silicon carbide: from amorphous to crystalline material. *Appl. Surf. Sci.* **2001**, *184*, 20-26.

(210) Sun, X.; Liu, H. T.; Cheng, H. F. Oxidation behavior of silicon nitride fibers obtained from polycarbosilane fibers via electron beam irradiation curing. *RSC Adv.* **2017**, *7*, 47833-47839.

(211) Ma, D. H.; Wang, H. J.; Niu, M.; Wen, J. B.; Wei, H.; Zhou, J.; Fan, J. P.; Zhang, D. H. Oxidation behavior of amorphous silicon nitride nanoparticles. *Ceram. Int.* **2018**, *44*, 1443-1447.

(212) Volodin, V. A.; Efremov, M. D.; Gritsenko, V. A.; Kochubei, S. A. Raman study of silicon nanocrystals formed in SiNx films by excimer laser or thermal annealing. *Appl. Phys. Lett.* **1998**, *73*, 1212-1214.

(213) Wieligor, M.; Wang, Y.; Zerda, T. W. Raman spectra of silicon carbide small particles and nanowires. *J. Phys.-Condens. Matter* **2005**, *17*, 2387-2395.

(214) Pauling, L. C.: *The nature of the chemical bond and the structure of molecules and crystals. an introduction to modern structural chemistry*; 2 ed. ed.; Cornell University Press, 1960.

(215) Sardar, K.; Bounds, R.; Carravetta, M.; Cutts, G.; Hargreaves, J. S.; Hector, A. L.; Hriljac, J. A.; Levason, W.; Wilson, F. Sol-gel preparation of low oxygen content, high surface area silicon nitride and imidonitride materials. *Dalton Trans.* **2016**, *45*, 5765-5774.

(216) Bland, H. A.; Thomas, E. L. H.; Klemencic, G. M.; Mandal, S.; Morgan, D. J.; Papageorgiou, A.; Jones, T. G.; Williams, O. A. Superconducting diamond on silicon nitride for device applications. *Sci. Rep.* **2019**, *9*, 2911-2919.

(217) Brow, R. K.; Patano, C. G. Compositionally dependent silicon 2p binding energy shifts in silicon oxynitride thin films. *J. Am. Ceram. Soc.* **1986**, *69*, 314-316.

(218) Wu, C.-Y.; Chang, C.-C.; Duh, J.-G. Silicon nitride coated silicon thin film on three dimensions current collector for lithium ion battery anode. *J. Power Sources* **2016**, *325*, 64-70.

(219) Huang, X. D.; Zhang, F.; Gan, X. F.; Huang, Q. A.; Yang, J. Z.; Lai, P. T.; Tang, W. M. Electrochemical characteristics of amorphous silicon carbide film as a lithium-ion battery anode. *RSC Adv.* **2018**, *8*, 5189-5196.

(220) Choi, W. K.; Ong, T. Y.; Tan, L. S.; Loh, F. C.; Tan, K. L. Infrared and x-ray photoelectron spectroscopy studies of as-prepared and furnace-annealed radio-frequency sputtered amorphous silicon carbide films. *J. Appl. Phys.* **1998**, *83*, 4968-4973.

(221) Contarini, S.; Howlett, S. P.; Rizzo, C.; De Angelis, B. A. XPS study on the dispersion of carbon additives in silicon carbide powders. *Appl. Surf. Sci.* **1991**, *51*, 177-183.

(222) Chen, L. C.; Chen, C. K.; Wei, S. L.; Bhusari, D. M.; Chen, K. H.; Chen, Y. F.; Jong, Y. C.; Huang, Y. S. Crystalline silicon carbon nitride: A wide band gap semiconductor. *Appl. Phys. Lett.* **1998**, *72*, 2463-2465.

(223) Gao, Y.; Wei, J.; Zhang, D. H.; Mo, Z. Q.; Hing, P.; Shi, X. Effects of nitrogen fraction on the structure of amorphous silicon–carbon–nitrogen alloys. *Thin Solid Films* **2000**, *377-378*, 562-566.

(224) Gomez, F. J.; Prieto, P.; Elizalde, E.; Piqueras, J. SiCN alloys deposited by electron cyclotron resonance plasma chemical vapor deposition. *Appl. Phys. Lett.* **1996**, *69*, 773-775.

(225) Liu, A. Y.; Cohen, M. L. Structural properties and electronic structure of low-compressibility materials: β-silicon nitride and hypothetical carbon nitride (β-C3N4). *Phys. Rev. B: Condens. Matter* **1990**, *41*, 10727-10734.

(226) Li, K.; Zhang, J.; Lin, D.; Wang, D. W.; Li, B.; Lv, W.; Sun, S.; He, Y. B.; Kang, F.; Yang, Q. H.; Zhou, L.; Zhang, T. Y. Evolution of the electrochemical interface in sodium ion batteries with ether electrolytes. *Nat Commun.* **2019**, *10*, 725-734.

(227) Lu, P.; Li, C.; Schneider, E. W.; Harris, S. J. Chemistry, impedance, and morphology evolution in solid electrolyte interphase films during formation in lithium ion batteries. *J. Phys. Chem. C* **2014**, *118*, 896-903.

(228) Eshetu, G. G.; Diemant, T.; Hekmatfar, M.; Grugeon, S.; Behm, R. J.; Laruelle, S.; Armand, M.; Passerini, S. Impact of the electrolyte salt anion on the solid electrolyte interphase formation in sodium ion batteries. *Nano Energy* **2019**, *55*, 327-340.

(229) Wang, C.; Wang, L.; Li, F.; Cheng, F.; Chen, J. Bulk bismuth as a high-capacity and ultralong cycle-Life anode for sodium-ion batteries by coupling with glyme-based electrolytes. *Adv. Mater.* **2017**, *29*, 1702212-1702218.

(230) Web of Science Database Search, Thompson-Reuters. **2020**.

(231) Zhu, Z.; Cheng, F.; Hu, Z.; Niu, Z.; Chen, J. Highly stable and ultrafast electrode reaction of graphite for sodium ion batteries. *J. Power Sources* **2015**, *293*, 626-634.

(232) Matei Ghimbeu, C.; Górka, J.; Simone, V.; Simonin, L.; Martinet, S.; Vix-Guterl, C. Insights on the Na + ion storage mechanism in hard carbon: Discrimination between the porosity, surface functional groups and defects. *Nano Energy* **2018**, *44*, 327-335.

(233) Zhang, M.; Garcia-Araez, N.; Hector, A. L.; Owen, J. R. A sol–gel route to titanium nitride conductive coatings on battery materials and performance of TiN-coated LiFePO4. *J. Mater. Chem. A* **2017**, *5*, 2251-2260.

(234) Kaspar, J.; Storch, M.; Schitco, C.; Riedel, R.; Graczyk-Zajac, M. SiOC (N)/hard carbon composite anodes for Na-ion batteries: influence of morphology on the electrochemical properties. *J. Electrochem. Soc.* **2016**, *163*, A156-A162.